



Fakultät für Physik

Joule-Class Ultrafast Thin Disk Laser System with Kilohertz Repetition Rate for Atmospheric Applications

Clemens Herkommer

Vollständiger Abdruck der von der Fakultät für Physik der Technischen Universität München
zur Erlangung des akademischen Grades eines

Doktors der Naturwissenschaften (Dr. rer. nat.)

genehmigten Dissertation.

Vorsitzender:

Prof. Dr. Johannes Knolle

Prüfer der Dissertation:

1. Prof. Dr. Reinhard Kienberger

2. Prof. Dr. Franz Pfeiffer

Die Dissertation wurde am 22.10.2021 bei der Technischen Universität München eingereicht
und durch die Fakultät für Physik am 27.01.2022 angenommen.



To Anna



Kurzzusammenfassung

Die Kontrolle über destruktive atmosphärische Phänomene wie Blitze ist seit langem ein Traum der Menschheit. Im Rahmen des Laser Lightning Rod Projektes wird das aktive Triggern von aufwärts gerichteten Blitzentladungen mittels der Filamentation von ultrakurzen Laserpulsen erforscht. Mit Hilfe der Laserfilamente kann eine elektrische Leitfähigkeit der Luft verursacht werden, wodurch ein für die Blitzentladungen bevorzugter Pfad generiert werden kann. Um diesen leitfähigen Kanal permanent aufrecht zu erhalten wird eine Ultrakurzpuls-Laserquelle mit einer Wiederholrate im Kilohertzbereich, Pulsenergien auf dem Joule-Level und Pulsspitzenleistungen im Terawattbereich benötigt.

In der vorliegenden Thesis wird die Entwicklung einer für die Anwendung als Laser Lightning Rod in der Atmosphärenforschung spezialisierte Ultrakurzpuls-Laserquelle präsentiert. Das Lasersystem basiert auf industrieller Scheibenlasertechnologie unter Verwendung Ytterbium-dotierter Laserkristalle und emittiert bei einer Wellenlänge von 1030 nm. Für die CPA Konfiguration wird ein gechirptes Faser Bragg-Gitter in Kombination mit einem Gitterkompressor verwendet. Die gestreckten Seed-Pulse werden von einem modifizierten kommerziellen Mikromaterialbearbeitungslaser bereitgestellt. Diese werden zuerst in einem regenerativen Verstärker auf 240 mJ und danach in einem Multipassverstärker auf 800 mJ verstärkt. Nach der Kompression wird eine Energie von 720 mJ bei einer Pulsdauer von 920 fs erreicht. Die Strahlqualität bei voller Leistung weist eine Beugungsmaßzahl von $M^2=1.9$ auf.

Um eine geeignete Laserscheibengeometrie für den Multipassverstärker auszuwählen wurde eine Studie hinsichtlich der Verstärkungseigenschaften und deren Limitierung durch verstärkten Spontanemission unter Variation der Pumpparameter durchgeführt. Ausgehend von diesen Resultaten wurde eine geeignete Laserscheibengeometrie für den Multipassverstärker für die Zielwiederholrate von 1 kHz ausgewählt.

Mit der komprimierten regenerativen Verstärkerstufe wurden Vorexperimente zum Auslösen und Führen von elektrischen Hochspannungsentladungen im Labor durchgeführt. Durch Konversion von Teilen der Pulsenergie zur zweiten und dritten Harmonischen mittels nichtlinearer Kristalle konnte die Durchbruchspannung und die minimale Pulsenergie für Funkenüberschläge im Vergleich zur fundamentalen Wellenlänge trotz des Leistungsverlustes durch die begrenzte Konversionseffizienz deutlich reduziert werden.

Das entwickelte Lasersystem wurde in einer experimentellen Kampagne eingesetzt, mit dem Ziel, die Filamentation horizontal über eine Länge von 140 m zu charakterisieren. Die Filamentationszone erstreckte sich über mehr als 70 m und ihr Beginn konnte über eine

Distanz von 120 m hinausgezögert werden. Dies sind wichtige Eigenschaften für den Erfolg einer experimentelle Feldkampagne auf dem Säntis im Sommer 2021.

Abstract

Controlling destructive atmospheric phenomena such as lightning has been a long dream of mankind. In the context of the Laser Lightning Rod project, active triggering of upward atmospheric lightning discharges using ultrafast laser filamentation is addressed. Enabled by the electrical conductivity associated with the laser filaments or the density depression in the laser wake, a preferential path for the lightning discharges can be generated. To maintain a permanent conductive channel from the thundercloud to the ground, an ultrafast laser source providing kilohertz repetition rate and Joule-class pulse energy is required.

In this thesis, the development of an ultrafast laser system specialized for the application as a laser lightning rod in atmospheric research is presented. The laser system is based on industrial thin-disk technology using Ytterbium-doped laser crystals emitting at a wavelength of 1030 nm. The CPA configuration comprises a chirped fiber Bragg grating in combination with a grating compressor. The stretched seed pulses are generated by a modified industrial micromachining laser. They are amplified first with a regenerative amplifier to 240 mJ, and subsequently with a multipass amplifier to 800 mJ. After compression, 920 fs pulses with 720 mJ were obtained. A beam quality with an M^2 of 1.9 is measured at the full output power.

To select a suitable thin-disk geometry for the multipass amplifier, a study on amplified spontaneous emission and on the energy storage in the disks was performed. The limitation of the population inversion due to amplified spontaneous emission was tested by varying the pump duration and the pump power. The inversion in the disks was probed across one pump cycle, revealing plateaus for high pump energies as predicted by simulations of ASE in thin-disk lasers in the literature. Based on the results, the optimal thin-disk geometry for a repetition rate of 1 kHz was selected.

Laboratory experiments on triggering and guiding of electrical discharges were performed with the first amplifier stage of the laser system. With parts of the laser energy converted to the second and third harmonic using nonlinear crystals, it was demonstrated that the breakdown voltage could be significantly reduced as compared to using only the fundamental wavelength.

The completed laser system was used in an experimental campaign to characterize the laser filamentation region horizontally over a length of 140 m. The longest filamentation zone extended over more than 70 m, and the onset of filamentation could be retarded beyond a propagation distance of 120 m. These are important characteristics for the experimental outdoor campaign during the lightning season in summer 2021 at Mt. Säntis, Switzerland.

Table of Contents

I	List of Publications	i
II	List of Acronyms	iii
III	List of Figures	v
IV	List of Tables	viii
1	Introduction	1
2	Theory and Basic Aspects	6
2.1	Ultrafast Laser Physics.....	6
2.1.1	Fundamental Physical Properties of Yb:LuAG	6
2.1.2	Dispersion and Ultrafast Optical Pulses	14
2.1.2.1	Material dispersion.....	14
2.1.2.2	Group velocity dispersion.....	15
2.1.2.3	Higher-order dispersion	19
2.1.2.4	Dispersive optical elements	20
2.1.2.5	Ultrashort pulses.....	22
2.1.3	Optical Resonators	24
2.1.4	Beam Quality	25
2.2	Basics of Nonlinear Optics.....	26
2.3	Filamentation and Breakdown of Optical Pulses.....	32
3	Front-End	35
3.1	Seed Laser.....	35
3.2	Regenerative Amplifier	36
4	Study of energy storage and ASE in different thin-disk geometries	45
4.1	Measurement setup and approach	45
4.2	Results for 3 thin-disk geometries and discussion	48
5	Thin-disk Multipass Amplifier	55
5.1	Design Considerations	55
5.2	Preparatory Experiments.....	59
5.2.1	Characterization of the pump power	59
5.2.2	Thermal load reduction by pulsed pumping.....	60
5.2.3	Influence of the pump spot on the propagation	61
5.3	Studies on high-energy pulse amplification.....	66
5.3.1	Concept A: Amplifier including 1 thin disk	66
5.3.2	Concept B: Amplifier including 2 thin disks.....	74

5.3.3	Concept C: Amplifier including 3 and 4 thin disks.....	79
5.4	Final Multipass Amplifier Layout	82
5.5	Completed LLR Laser System.....	90
6	Dispersion Management and Pulse Compression.....	92
6.1	CPA Design and Pulse Stretching	92
6.2	Layout of the Grating Compressor.....	95
6.3	Compression of high-energy output pulses.....	102
7	Experiments	106
7.1	HV Discharge Triggering	106
7.2	Short Range Filament Generation	107
7.3	Long-Range Filament Generation.....	109
8	Summary and Outlook.....	113
9	Bibliography.....	117
10	Appendix	129

I List of Publications

Journal articles

T. Produit, P. Walch, C. Herkommer, A. Mostajabi, M. Moret, U. Andral, A. Sunjerga, M. Azadifar, Y.-B. André, B. Mahieu, W. Haas, B. Esmler, G. Fournier, P. Krötz, T. Metzger, K. Michel, A. Mysyrowicz, M. Rubinstein, F. Rachidi, J. Kasparian, J.-P. Wolf, and A. Houard, "The laser lightning rod project," *Eur. Phys. J. Appl. Phys.* **93**, 10504 (2021).

C. Herkommer, P. Krötz, R. Jung, S. Klingebiel, C. Wandt, R. Bessing, P. Walch, T. Produit, K. Michel, D. Bauer, R. Kienberger, and T. Metzger, "Ultrafast thin-disk multipass amplifier with 720 mJ operating at kilohertz repetition rate for applications in atmospheric research," *Opt. Exp.* **28**, 30164–30173 (2020).

T. Produit, P. Walch, G. Schimmel, B. Mahieu, C. Herkommer, R. Jung, T. Metzger, K. Michel, Y.-B. André, A. Mysyrowicz, A. Houard, J. Kasparian, and J.-P. Wolf, "HV discharges triggered by dual- and triple-frequency laser filaments," *Opt. Exp.* **27**, 11339-11347 (2019)

Conference Contributions

C. Herkommer, P. Krötz, S. Klingebiel, R. Kienberger, and T. Metzger, "Joule-Class Ultrafast Thin-Disk Laser Amplifiers for Applications in Atmospheric Research," in *Imaging and Applied Optics Congress 2021*, in OSA Imaging and Applied Optics Congress 2021, OSA Technical Digest (Optica Publishing Group, 2021), paper PTh2E.2.

C. Wandt, C. Herkommer, R. Jung, S. Klingebiel, P. Krötz, M. Rampp, C. Y. Teisset, K. Michel, and T. Metzger, "Ultrafast Thin-Disk based CPA System with >1kW Output Power and <500 fs Pulse Duration," in *Ultrafast Phenomena 2020*, OSA Technical Digest (Optical Society of America, 2020), paper W2A.2.

C. Wandt, C. Herkommer, R. Jung, S. Klingebiel, P. Krötz, S. Prinz, M. Rampp, C. Y. Teisset, K. Michel, and T. Metzger, "Ultrafast Thin-Disk based CPA System with >1kW Output Power and <500 fs Pulse Duration," in *High-Brightness Sources and Light-driven Interactions*, OSA Technical Digest (online) (Optical Society of America, 2020), paper HM2B.4.

- C. Herkommer, P. Krötz, S. Klingebiel, C. Wandt, D. Bauer, K. Michel, R. Kienberger, and T. Metzger, "Towards a Joule-Class Ultrafast Thin-Disk Based Amplifier at Kilohertz Repetition Rate," in Conference on Lasers and Electro-Optics (Optical Society of America, 2019), paper SM4E.3.
- C. Herkommer, P. Krötz, S. Klingebiel, C. Wandt, D. Bauer, K. Michel, R. Kienberger, and T. Metzger, "Towards a Joule-Class Ultrafast Thin-Disk Based Amplifier at Kilohertz Repetition Rate", DPG Frühjahrstagung, paper K3.3, München (2019).
- T. Metzger, C. Grebing, C. Herkommer, S. Klingebiel, P. Krötz, S. Prinz, S. Stark, C. Y. Teisset, C. Wandt, K. Michel, "High-power ultrafast industrial thin-disk lasers," Proc. SPIE 11034, Short-pulse High-energy Lasers and Ultrafast Optical Technologies, 110340N (2019).
- P. Krötz, C. Grebing, C. Herkommer, R. Jung, S. Klingebiel, S. Prinz, C. Teisset, C. Wandt, K. Michel, and T. Metzger, "High-Power Ultrafast Industrial Thin-Disk Lasers," in Laser Congress 2019 (ASSL, LAC, LS&C), OSA Technical Digest (Optical Society of America, 2019), paper CTu1C.4.
- P. Krötz, C. Wandt, C. Grebing, C. Herkommer, R. Jung, S. Klingebiel, S. Prinz, C. Teisset, K. Michel, and T. Metzger, "Towards 2 kW, 20 kHz ultrafast thin-disk based regenerative amplifiers," in Laser Congress 2019 (ASSL, LAC, LS&C), OSA Technical Digest (Optical Society of America, 2019), paper ATh1A.8.
- C. Herkommer, P. Krötz, S. Klingebiel, C. Wandt, S. Stark, K. Michel, R. Kienberger, and T. Metzger, "Towards High-Power Picosecond Thin-Disk Laser Amplifiers with 1 Joule Pulse Energy for Filamentation Applications", COFIL Geneva (2018).

II List of Acronyms

Yb	Ytterbium
YAG	Yttrium-Aluminum Garnet
LuAG	Lutetium-Aluminum Garnet
Yb:YAG	Ytterbium-doped YAG
Yb:LuAG	Ytterbium-doped LuAG
InGaAs	Indium-Gallium-Arsenide
Ti:Sa	Titanium-doped Sapphire
MOPA	Master Oscillator Power Amplifier
HV	High Voltage
LLR	Laser Lightning Rod
ESA	Excited-State Absorption
ETU	Electron-Transfer Up-Conversion
ASE	Amplified Spontaneous Emission
CW	Continuous-Wave
AR	Anti-Reflection
HR	High-Reflection
TIR	Total Internal Reflection
GD	Group Delay
GVD	Group Velocity Dispersion
GDD	Group-Delay Dispersion
TOD	Third-Order Dispersion
FOD	Fourth-Order Dispersion
SPM	Self-Phase Modulation
SHG	Second-Harmonic Generation
DFG	Difference-Frequency Generation

List of Acronyms

FWM	Four-Wave Mixing
SF	Self-Focusing
TPA	Three-Photon Absorption
CFBG	Chirped Fiber-Bragg Grating
FWHM	Full Width at Half-Maximum
AOM	Acousto-Optic Modulator
ROC	Radius of Curvature
SLM	Spatial Light Modulator
CCD	Charge-Coupled Device
MP	Multipass
DPSSL	Diode-Pumped Solid-State Laser
LIDT	Laser-Induced Damage Threshold
FTL	Fourier Transform-Limit
CAD	Computer-Aided Design
AOI	Angle of Incidence
IPR	In-Plane Rotation
LBO	Lithium Triborate

III List of Figures

Figure 1.1: Schematic application scenario of a laser lightning rod.....	5
Figure 2.1: Energy levels of typically used rare-earth dopant ions.	7
Figure 2.2: Energy level diagram of Yb:LuAG at 10 at%.....	8
Figure 2.3: Emission and absorption cross sections of Yb:LuAG with 10 at% at 293 K.....	8
Figure 2.4: Schematic diagram of the inversion ranges for Yb:LuAG.....	9
Figure 2.5: Diagram of the inverted fraction β	11
Figure 2.6: Threshold intensity required to achieve transparency	12
Figure 2.7: Sketch of ASE propagation in a discoidal shaped laser medium.....	13
Figure 2.8: Refractive index of silica	15
Figure 2.9: Sketch of an optical resonator consisting of two spherical mirrors.	25
Figure 2.10: Illustration of self-phase modulation.....	30
Figure 2.11: Illustration of the effect of self-focusing in a transparent nonlinear material.	32
Figure 2.12: Balance between Kerr self-focusing and plasma defocusing in filaments.	34
Figure 3.1: Characteristics of the seed laser.....	35
Figure 3.2: Layout of the regenerative amplifier.....	36
Figure 3.3: Design of the resonator of the regenerative amplifier.....	37
Figure 3.4: Visualization of pulsed pumping vs. cw pumping.	38
Figure 3.5: Amplification with different numbers of roundtrips.....	39
Figure 3.6: Amplification characteristics of the regenerative amplifier.....	40
Figure 3.7: Spectral pre-shaping of the seed pulses to compensate for the gain narrowing.	41
Figure 3.8: M^2 measurement of the uncompressed output of the regenerative amplifier.	41
Figure 3.9: Long-term measurement of the regenerative amplifier.....	42
Figure 3.10: Operation of the regenerative amplifier with different repetition rates.....	43
Figure 3.11 Compression of the regenerative amplifier output.....	44
Figure 4.1: Schematic sketch of the experimental setup for the study on energy storage.	47

Figure 4.2: Measured single pass gain	49
Figure 4.3: Maximum single-pass gain and inversion ((a) and (b)).....	50
Figure 4.4: Photodiode (PD) signals and spectra measured during the experiments.	51
Figure 4.5: Instantaneous gain probed over the duration of the pump pulse at 100 Hz.....	52
Figure 4.6: Simulation of the gain build-up as a function of time	53
Figure 5.1: Schematic visualization of different concepts to achieve stable propagation.....	57
Figure 5.2: Characterization of the pump unit comprising 6 pump laser diode modules.....	59
Figure 5.3: Experiment to determine the dioptric power of the thin-disk.....	60
Figure 5.4: Collimation and beam transport of the pump light.	63
Figure 5.5: Pump spots for different focal lengths of the pump collimation lens.	63
Figure 5.6: Beam profile evolution over 8 disk passes.....	64
Figure 5.7: Beam profile evolution over six passes for different pump spot diameters.	65
Figure 5.8 Experimental setup of the first multipass amplifier prototype.	66
Figure 5.9: Amplification with the first multipass amplifier prototype	67
Figure 5.10: Pulse amplification with different pump energies E_p and duty cycles (DC).	68
Figure 5.11: Pulse amplification with the alignment optimized for the beam quality.	69
Figure 5.12: Pulse amplification using 12 disk passes and a de-focused pump spot.	70
Figure 5.13: M^2 measurement setup.....	72
Figure 5.14 M^2 measurements from the 1-head multipass amplifier	73
Figure 5.15: Experimental setup of the second multipass amplifier prototype.....	75
Figure 5.16: Experimental results from pulse amplification with 2 laser heads.....	76
Figure 5.17: Reduction of the tangential gain as a function of the seed pulse energy.....	77
Figure 5.18: Comparison of experimental results using 1 laser head and 2 laser heads.....	78
Figure 5.19: Experimental setup of concept C with 4 thin disk lasers heads integrated.	80
Figure 5.20: Experimental results from the setup including up to 4 thin disk laser heads.....	81
Figure 5.21: Schematic top view of the final multipass amplifier.	82
Figure 5.22: Beam propagation inside the final multipass amplifier setup.	84
Figure 5.23: Performance of the multipass amplifier.....	85

Figure 5.24: M^2 measurements at of the two multipass stages.	86
Figure 5.25: Spectrum and autocorrelation trace of the compressed output at 720 mJ.....	87
Figure 5.26: Collimated output beam profiles.	88
Figure 5.27 Stability of the multipass amplifier.....	89
Figure 5.28: Schematic sketch of the final setup of the developed laser system.....	90
Figure 5.29: Photograph of the completed laser system used for experiments.	91
Figure 6.1: Transmission and dispersion of the two chirped fiber Bragg gratings	92
Figure 6.2: Pulse duration as a function of the GDD, controlled by the waveshaper.	93
Figure 6.3: Schematic sketch for the layout of the grating compressor	96
Figure 6.4: Fourier transform limited pulse duration before and after a bandpass.....	97
Figure 6.5: Layout of the grating compressor.	99
Figure 6.6: Results from the compressor ray-tracing.	100
Figure 6.7: Coordinate system and convention of the rotation direction denomination.....	102
Figure 6.8: Spectral characteristics of the amplification chain.....	104
Figure 6.9: Compression of the pulses from the regen.	104
Figure 7.1: HV discharge triggering in the laboratory.	106
Figure 7.2: Schematic sketch of short-range filamentation experiments in the laboratory. ...	108
Figure 7.3 Filament generation at different output pulse energies.	108
Figure 7.4: Theoretical and experimental filamentation length.....	109
Figure 7.5: Long-range filament generation with the developed laser system.....	110
Figure 7.6: Filament detection with photographic paper.....	111
Figure 7.7: Beam expanding telescope for remote filament generation.	112

IV List of Tables

Table 2.1: Sellmeier coefficients for silica glass.....	14
Table 4.1: Material properties of a standard Yb doped thin disk.	46
Table 4.2: Studied disk geometries.....	48
Table 5.1: Cumulated fluence in the two multipass amplifier stages.	83
Table 5.2: Summary of the output parameters of the final multipass amplifier.	84
Table 10.1: Pump energy as a function of pump pulse duration and the peak pump power.	130

1 Introduction

Since the first demonstration of the ruby laser by Theodore Maiman in 1960 [1], it has transitioned from “a solution looking for a problem” to one of the most versatile tools in research and industry [2,3]. Today, driven by numerous applications, a broad parameter range is covered with respect to the wavelength, average power, pulse energy, and the pulse duration [4,5]. A steady increase of the energy and peak power of ultrafast pulses in the picosecond and femtosecond regimes could be achieved with the MOPA scheme, continuously expanding the spectrum of applications. Since the invention of the chirped-pulse amplification (CPA) technique [6], the available pulse energy has taken another leap, initiating a new era in the field of high-power lasers [7]. Associated with the previously unattained pulse energies and peak powers, new fields of research have emerged, as new physical phenomena became observable. Righteously, the 2018 Nobel prize in physics was therefore awarded partially to Donna Strickland and Gérard Mourou for the development of CPA [8,9].

Enabled by CPA-based Ti:Sa lasers with multi-milli-Joule pulse energy and peak powers beyond the terawatt level, a self-channeling process of ultrafast pulses was first observed in 1995 [10] and was later named laser filamentation, which led to a research field on its own [11,12]. While plasma generation in air can already be achieved by focusing highly energetic nanosecond laser pulses, the generated high electron densities above the critical plasma density render the air opaque for the trailing part of the pulses, preventing further propagation. As a consequence, localized plasma balls are formed. In turn, picosecond and shorter pulses can undergo extended filamentation, due to the absence of avalanche ionization within the duration of the pulse, allowing for further pulse propagation. The ability to remotely deliver high intensities with the laser beam, and the possibility to remotely create and control extended plasma channels with precise temporal control, unlocked numerous applications in atmospheric research [13,14]. These include laser-based telecommunication through fog [15–17], cloud seeding to stimulate rain or snowfall [18–20], remote sensing of atmospheric compounds [21–23] and the laser lightning rod [24]. The latter is based on the electrical conductivity of the lineic plasma channel left in the wake of an ultrashort pulse undergoing filamentation, and also the subsequent air density depression, following Paschen’s law [25]. In laboratory environments, HV discharge triggering and guiding has early been demonstrated and investigated in detail [26–28]. Moreover, in outdoor experiments, filamentation could be observed over a distance of several hundreds of meters [29], while the beam collapse point can be controlled and retarded via the temporal duration of the laser pulses and geometrical focusing of the laser beam.

Only two attempts to trigger atmospheric lightning with pulsed lasers have been launched in the past. The first was in 1999 with a combination of nanosecond CO₂, Nd:Glass, and Nd:YAG lasers [30], and the second in 2008 using a femtosecond Ti:Sa laser [31]. From these experiments, the evidence on artificially triggered lightning is statistically questionable. However, electrical discharge events in the thunderclouds synchronized with the laser could be identified as described in [31], verifying the concept of laser-initiated lightning rod.

The success of a laser-assisted lightning rod relies on the extended increased electrical conductivity invoked by the laser filaments. In addition to the electrical conductivity associated with the free carriers in the ionized channel, it was found that a cumulative effect at high laser repetition rates can further reduce the breakdown voltage between two HV electrodes [32–34]. After recombination of the free carriers with the nuclei in the plasma within tens of nanoseconds, a channel of heated and under-dense air remains in the wake of the pulse on a time scale of milliseconds (pulse propagation in air), providing a much longer-lived channel with an increased electrical conductivity as compared to regions apart from the laser beam. When the repetition rate of the laser approaches the inverse lifetime of the heated and under-dense air channel, i.e. an order of 1 kHz, it is maintained permanently. Such a channel provides a preferential path for electric discharges following Paschen's law [35] and allows for atmospheric leaders and corona fronts to propagate over long distance, facilitating the application as a laser lightning rod [14].

From the perspective of laser engineering, the kilohertz repetition rate translates to average powers in a regime of hundreds of Watts, since high pulse energies and peak powers approaching the terawatt level are required to initiate the filamentation process and to provide an energy reservoir for long-distance and extended filament generation. Lasers based on the Ti:Sa technology have been the workhorse for research on laser filamentation for decades, due to the large available amplification bandwidth and the resulting femtosecond pulse durations, leading to terawatt peak powers at milli-Joule level pulse energies. However, high average powers are limited by the large quantum defect and the poor heat extraction in the bulk crystal geometry [36], preventing the combination of high pulse energies with high repetition rates.

On the other hand, Ytterbium-based lasers are very successful in delivering kilowatt average powers [37–41]. Their exceptionally low quantum defect of only 9%, the absence of excited-state absorption, and the availability of powerful InGaAs pump laser diodes in the 940-nm absorption band enable high efficiency and performance [42]. Pulse durations well below the picosecond level are supported by the amplification bandwidth. While the efficient heat removal in the fiber, slab and thin disk architectures have enabled kilowatt average-powered ultrafast

lasers [40,43–45], the thin-disk is particularly suited for high pulse energies due to its large aperture [46].

Invented in 1992 by Adolf Giesen [42], the thin disk laser technology was matured and industrialized by TRUMPF Laser GmbH. In CW operation, the output power from a single disk can reach up to 12 kW in multimode operation [47] and up to 4 kW in single mode operation [48]. Recently, ultrafast pulsed thin-disk laser systems have also traversed the multi-kilowatt power threshold [49]. The maximum pulse energy can be scaled with the disk diameter, since the stored energy is increased and at the same time laser-induced damage is avoided as the peak fluence is decreased for larger beam diameters. Consequently, thin-disk based regenerative amplifiers have been leading the field of high-repetition rate and high-energy ultrafast lasers in the last decade. Up to 260 mJ have been achieved recently at 1 kHz with near-diffraction limited beam quality [50]. Average powers above the kilowatt level are provided by integration of a second laser head in the resonator of the amplifier [51,52]. For even higher pulse energies, eventually, a limitation is given by the aperture and optical quality of the Pockels cells typically used as electro-optic switch inside the resonator.

Thin-disk based multipass amplifiers offer a simple and flexible platform for further scaling of the pulse energy and average power, profiting from the benefits of the thin-disk geometry. The linear propagation of the signal through the amplifier does not rely on a closed optical resonator, eliminating the limitation for the pulse energy otherwise set by the optical switch. Furthermore, arbitrary signals (eg. pulse bursts, long pulses) can be amplified, and nonlinearities are minimized when employing reflective optics. Finally, several laser heads or several multipass amplifier stages can be serially combined to scale pulse energy and average power.

In the last decade, substantial progress has been achieved in the development of ultrafast thin-disk based multipass amplifiers. Without CPA, single pulse energies up to 140 mJ have been achieved in 2013 with an amplifier operating in burst mode with 80 pulses per burst, leading to a total burst energy of 11.2 J [53]. This result was achieved at 10 Hz burst repetition rate, leading to an average power of 112 W. In the following years until 2016, researchers at the Institut für Strahlwerkzeuge (IFSW) in Stuttgart, Germany, continuously developed a CPA-free thin-disk based multipass amplifier yielding an average power as high as 2 kW with a pulse duration below 10 ps [45]. With a repetition rate of 300 kHz and a pulse energy of 6.7 mJ, the system was designed for novel applications in material processing such as the cutting of carbon fiber reinforced polymers. With a similar, industrialized multipass amplifier based on a monolithic glass mirror array, similar output power and pulse energy with a pulse duration of 1.3 ps were demonstrated in 2020 [44], featuring an optimized thermal stability and robustness, and employed for glass cleaving applications.

The development of high-power thin-disk multipass amplifiers with high pulse energy has been less advanced so far by research and industry. While in laser facilities, large Yb-based nanosecond laser amplifiers have reached pulse energies in the range from several Joules [54–56] up to 100 J [57], they are operated at repetition rates of only less than 10 Hz, mostly rely on cryogenically cooled laser crystals, and require footprints too large to be transported to experimental sites. In 2015, a compact thin-disk based multipass amplifier including two thin-disk laser heads operating at room temperature has attained a pulse energy of 1.07 J before the compression at a repetition rate of 100 Hz, with the potential for sub-picosecond pulse durations [58]. At repetition rates approaching 1 kHz, pulse energies above 1 Joule have to date been achieved only with cryogenically cooled multipass amplifiers, based on “thick-disk” type active mirror configurations [59,60]. However, the minimum pulse duration from such systems is limited to a few picoseconds due to the narrowed amplification bandwidth of the gain medium at cryogenic temperatures [61], which reduces the pulse peak power. For the application as a lightning rod, however, sub-picosecond pulse durations are desired as to enable extended filamentation with the absence of avalanche ionization.

In the framework of this thesis, a sub-picosecond thin-disk amplifier with Joule-class pulse energy operating at 1 kHz was developed [62]. The CPA system was conceived and tailored as the drive laser source for the FET-open research project “Laser Lightning Rod” [63], addressing a disruptive lightning protection technique based on a powerful ultrafast laser [64]. The complete amplifier chain consists of a commercial fiber laser used as the seed laser, a regenerative thin-disk pre-amplifier, and a main thin-disk multipass amplifier. Before pulse compression, a pulse energy of 800 mJ is achieved. After compression, sub-picosecond pulses with an energy of 720 mJ remain. The CPA design includes a chirped fiber Bragg grating to stretch the pulses, a waveshaper for small dispersion corrections, and a grating compressor to recompress them. For transportability, the whole laser system is divided in five modules which are mounted on mobile support structures to allow deployment to the experimental sites.

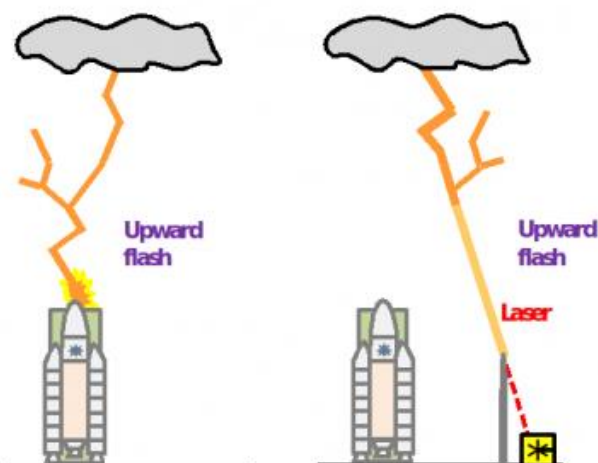


Figure 1.1: Schematic application scenario of a laser lightning rod protecting a rocket on a launching pad from lightning strikes. Figure taken from [65].

First horizontal experiments have been performed at LAL, Orsay, studying the filamentation characteristics over >140 m. A final experimental campaign is planned in summer 2021 at the summit of Mount Säntis, Switzerland, which is one of the locations with the highest lightning occurrence in Europe [66,67]. By remotely generating extended laser filaments starting at the tip of the station's 120 m tall antenna, upward lightning strikes are aimed to be initiated and guided from the tower. The results may have a major impact on future lightning protection approaches for sensitive sites such as airports, rocket launching pads, and power or industrial plants [64]. A schematic application scenario is shown in Figure 1.1.

2 Theory and Basic Aspects

In this chapter some basic theoretic fundamentals are discussed. The goal of this chapter is to provide a fundamental understanding in the context of the experimental work carried out in the framework of this dissertation. In addition, some useful formulae are derived which are used during the evaluation of the experimental results. More details and completeness of ultrafast laser physics can be found in standard text books [4,68–72].

2.1 Ultrafast Laser Physics

2.1.1 Fundamental Physical Properties of Yb:LuAG

Yb:LuAG as an alternative to Yb:YAG has become an important laser material for high-power applications. Since diode-pumping was enabled by the development of InGaAs laser diodes, the high intensities and brilliance at its broad absorption feature around 940 nm became available and enabled to surpass the relatively high power threshold for lasing. In such diode-pumped configurations, Yb:LuAG has several very useful advantages, which are detailed in the following.

Energy levels, absorption and emission cross sections

The energy level structure of the Yb³⁺ ion is relatively simple, when compared to those of other commonly used rare-earth dopants, as shown in Figure 2.1. In particular, no higher-energy levels exist above the two manifolds $^4F_{7/2}$ and $^4F_{5/2}$.

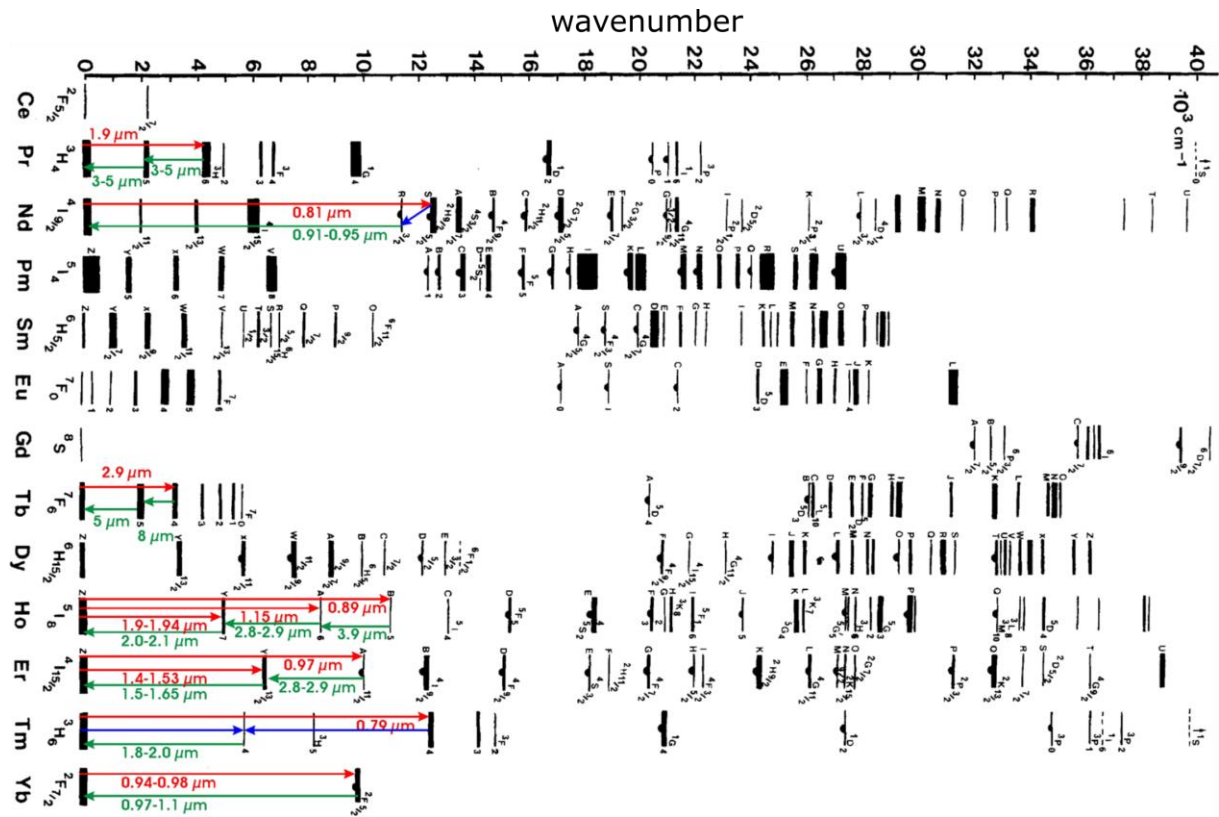


Figure 2.1: Energy levels of typically used rare-earth dopant ions. Technologically used optical transitions are indicated in red and green. Figure taken from [73].

This makes the Yb^{3+} ion suitable to be used in high doping concentrations, because parasitic processes such as excited-state absorption (ESA) of pump radiation as well as energy-transfer up-conversion (ETU) are absent, which would otherwise scale with the doping concentration. When used as a dopant in a host material such as LuAG, the $^4F_{7/2}$ and $^4F_{5/2}$ manifolds of Yb^{3+} are split further by the electric field of the crystal due to the Stark-effect, resulting in the laser-active energy levels as shown in the diagram in Figure 2.2. The transition used for the laser signal has a wavelength of 1030 nm, and the transitions commonly used for pumping are located at 939 nm and 969 nm. The complete absorption and emission spectra of 10 at% Yb:LuAG are shown in Figure 2.3.

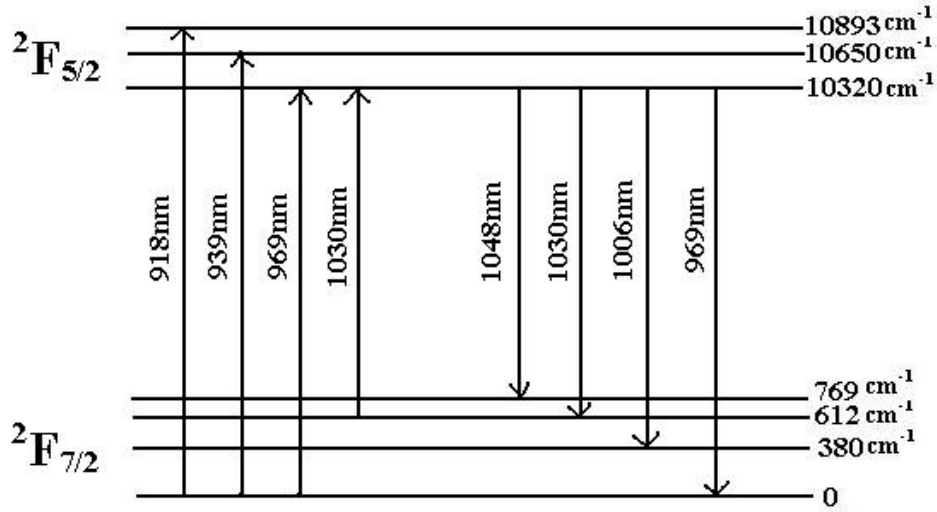


Figure 2.2: Energy level diagram of Yb:LuAG at 10 at%. Figure taken from [74].

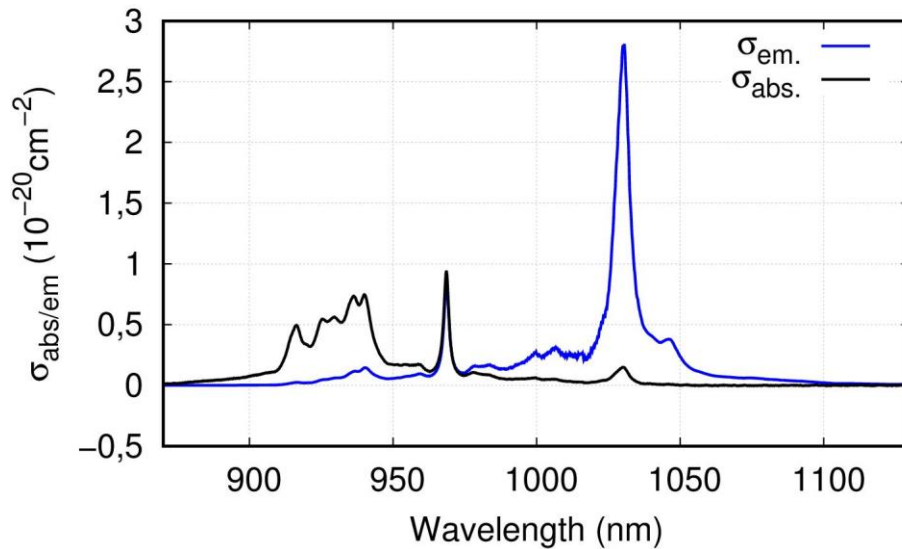


Figure 2.3: Emission and absorption cross sections of Yb:LuAG with 10 at% at 293 K. Curves are reproduced from [75].

Pumping and three level behavior

For the pumping process, the absorption bands around 940 nm and 969 nm are typically used. Around 940 nm, a quite broad absorption feature allows for straightforward diode pumping with a large wavelength tolerance. The Stokes quantum defect at this wavelength is $q_{940\text{ nm}} = \frac{(h\nu_{\text{pump}} - h\nu_{\text{Laser}})}{h\nu_{\text{pump}}} = 8.74\%$. The 969 nm absorption line is called the zero phonon line, as the ions are excited directly to the upper laser level and no non-radiative relaxation via lattice phonons takes place. This reduces the thermal load of the crystal further, with a resultant quantum defect $q_{969\text{ nm}} = 5.92\%$.

Due to the small quantum defect of Yb:LuAG, very low heat is generated in the laser material, however, coming along with a pronounced quasi-three level behavior. At room temperature, the energy difference from ground state to the lower laser level $\Delta E/h \sim 600 \text{ cm}^{-1}$. The thermal energy at $T = 293 \text{ K}$ is $E_T/h = k_B T/h = 203.6 \text{ cm}^{-1}$. Therefore the thermal population of the lower laser level is significant and leads to the typical behavior of quasi-three level laser media.

- The laser medium is absorbing at the signal laser wavelength. To reach transparency for the laser wavelength, a certain pump intensity is required. The threshold intensity as a function of the pump wavelength for Yb:LuAG is calculated in equation 2.5 and plotted in Figure 2.1.
- The corresponding inverted fraction beta cannot contribute to the gain and the energy stored in these ions cannot be accessed by the laser signal. For $\lambda_{\text{Laser}} = 1030 \text{ nm}$ this fraction is $\beta_{\text{max}}^{(1030 \text{ nm})} = 6.21 \%$. For the typical pump wavelengths, the fraction is $\beta_{\text{max}}^{(940 \text{ nm})} = 83.8 \%$ and $\beta_{\text{max}}^{(969 \text{ nm})} = 51.2 \%$.
- Therefore, during laser action, the lower limit for the inversion is given by $\beta_{\text{max}}^{(1030 \text{ nm})}$ and the upper limit for the inversion is given by $\beta_{\text{max}}^{(940 \text{ nm})}$. This is visualized in Figure 2.4, additionally taking into account potentially occurring amplified spontaneous emission before reaching the transparency for the pump wavelength. The amount of energy storable in the laser medium is thereby reduced as corresponding to the accessible inversion range.

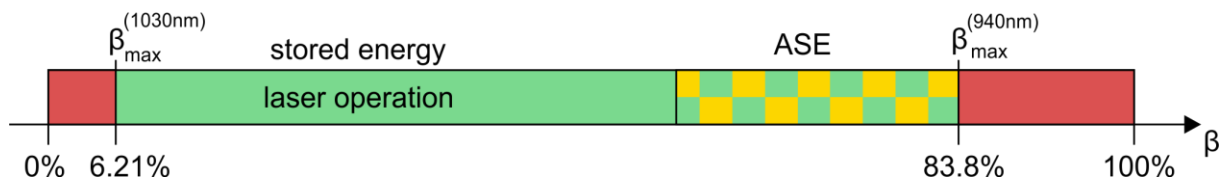


Figure 2.4: Schematic diagram of the inversion ranges for Yb:LuAG. At $\beta_{\text{max}}^{(1030 \text{ nm})} = 6.21 \%$, transparency for the laser wavelength is reached. Before reaching transparency for the pump wavelength at $\beta_{\text{max}}^{(940 \text{ nm})} = 83.8 \%$, ASE may further limit the inversion, depending on the geometry of the laser medium. The useable inversion range is therefore limited to the indicated range.

Inversion

Using the emission and absorption cross sections shown in Figure 2.3, one can calculate the steady-state inverted fraction β when the laser medium is optically pumped. The base equation for the derivation is the rate equation for the laser material:

$$\frac{dn_2}{dt} = \frac{I \cdot \lambda}{h \cdot c} \underbrace{\left(-\sigma_{em}^{(\lambda)} \cdot n_2 + \sigma_{abs}^{(\lambda)} \cdot n_1 \right)}_{\text{stim. em. / abs.}} - \underbrace{\frac{n_2}{\tau_{n_2}}}_{\text{spont. em.}}, \quad 2.1$$

where I is the intensity of the pump light, τ is the excited-state life time of the upper laser level, n_2 and n_1 are the populations of the upper and lower level for the pump transition, and $\sigma_{em}^{(\lambda)}$ and $\sigma_{abs}^{(\lambda)}$ are the emission and absorption cross sections at the respective wavelength λ .

To obtain the population of the laser levels in the steady-state, the time derivative of n_2 must vanish, i.e. $\frac{dn_2}{dt} = 0$, which gives:

$$\begin{aligned} 0 &= \frac{I \cdot \lambda}{h \cdot c} \left(-\sigma_{em}^{(\lambda)} \cdot n_2 + \sigma_{abs}^{(\lambda)} \cdot n_1 \right) - \frac{n_2}{\tau} \\ \Leftrightarrow \frac{n_1}{n_2} &= \frac{h \cdot c}{I \cdot \lambda \cdot \tau \cdot \sigma_{abs}^{(\lambda)}} + \frac{\sigma_{em}^{(\lambda)}}{\sigma_{abs}^{(\lambda)}} \end{aligned} \quad 2.2$$

With the definition of the inverted fraction $\beta = \frac{n_2}{n_1+n_2}$ one obtains the steady-state inverted fraction at a specific pump wavelength:

$$\beta^\lambda(I) = \frac{1}{\frac{h \cdot c}{I \cdot \lambda \cdot \tau \cdot \sigma_{abs}^{(\lambda)}} + \frac{\sigma_{em}^{(\lambda)}}{\sigma_{abs}^{(\lambda)}} + 1}. \quad 2.3$$

For high pump light intensities, i.e. $I \rightarrow \infty$, the inversion goes a maximum value β_λ^{max} :

$$\beta_{max}^{(\lambda)} = \frac{\sigma_{abs}^{(\lambda)}}{\sigma_{em}^{(\lambda)} + \sigma_{abs}^{(\lambda)}} \quad 2.4$$

This means that the maximum achievable steady-state inversion $\beta_{max}^{(\lambda)}$ is given by the emission and absorption cross sections of the gain material at the pump wavelength.

The maximum steady state inversion $\beta_{max}^{(\lambda)}$ is plotted as a function of the wavelength in Figure 2.5 (a) using the emission and absorption cross sections for Yb:LuAG given in [75]. The values at the two most common pump wavelengths 940 nm and 969 nm are indicated, showing significantly different maximum achievable inversions. As a consequence, when designing a laser or laser amplifier, the achievable inversion has to be traded off with the thermal load at a specific pump wavelength.

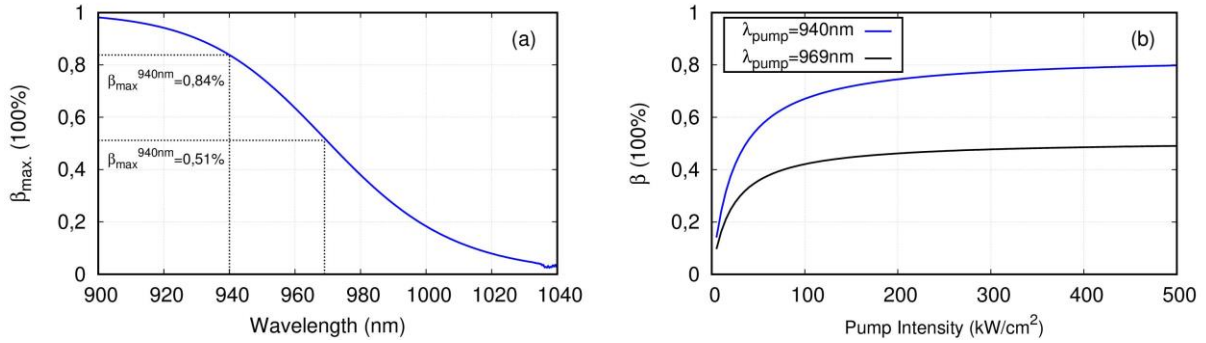


Figure 2.5: Diagram of the inverted fraction β . (a) Maximum achievable inverted fraction β as a function of the pumping wavelength, assuming high pump intensities. (b) Maximum achievable inverted fraction β for the pumping wavelengths 940 nm and 969 nm as a function of the total pump intensity.

Moreover, in real setups, the pump power and therefore the pump intensity is finite, which caps the actual inversion at a value lower than the theoretical limit. The inverted fraction is plotted as a function of the pump intensity in Figure 2.5 (b) for the pump wavelengths 940 nm and 969 nm. It can be seen that at approximately 100 kW/cm², the inversion is approaching close to the theoretical maximum, providing an estimation for the order of magnitude of the required pump intensity.

In thin-disk lasers, typically multipass arrangements are used to multiplex the pump light over the active medium. This enables pump intensities surpassing by far the single-pass intensity of the pump beam, leading to almost complete absorption of the pump power.

Transparency pump intensity in quasi-three level lasers

For classical four-level laser systems, inversion is achieved already at very low pump powers. This is due to the lower laser level being thermally unpopulated. In the case of quasi three-level laser systems, the lower laser level is energetically close to the ground state and its thermal population is therefore significant. When unpumped, laser signal radiation is therefore absorbed by the active medium. As a consequence, there is a certain pump intensity required to achieve transparency for the laser signal radiation. Furthermore, the threshold inversion corresponds to a certain amount of excited dopant ions, which therefore does not contribute to available energy stored in the inversion.

The transparency pump intensity can be calculated from the absorption and emission cross sections of the laser medium at the pump and the laser wavelength. First, the inversion β_{tr} required for transparency at the laser wavelength λ_{Laser} is given by equation 2.4 with $\lambda = \lambda_{\text{Laser}}$. This can be understood by considering that an infinite intensity eventually results in a dynamic balance between simulated emission and absorption at the signal wavelength, where

$n_1 = n_2$. By inserting β_{tr} into equation 2.3 and solving for the intensity, the threshold pump intensity $I_{th}^{(\lambda_p)}$ required to achieve transparency at the laser wavelength is given:

$$I_{th}^{(\lambda_p)} = \frac{h \cdot c}{\lambda_p} \cdot \frac{1}{\left(\sigma_{abs}^{(\lambda_p)} \left(\frac{\sigma_{em}^{(\lambda_{Laser})} + \sigma_{abs}^{(\lambda_{Laser})}}{\sigma_{abs}^{(\lambda_{Laser})}} - 1 \right) - \sigma_{em}^{(\lambda_p)} \right) \cdot \tau} \quad 2.5$$

In Figure 2.6 the transparency intensity is plotted as a function of the pump wavelength for the case of Yb:LuAG. At the most common pump wavelengths 940 nm and 969 nm, the transparency pump intensities are $I_{th}^{(940\text{ nm})} = 1.62\text{ kW/cm}^2$ and $I_{th}^{(969\text{ nm})} = 1.48\text{ kW/cm}^2$. Consequently, it is obvious that powerful and brilliant pump sources are required for the efficient laser operation. Therefore, Yb:LuAG lasers are conventionally pumped by InGaAs laser diodes.

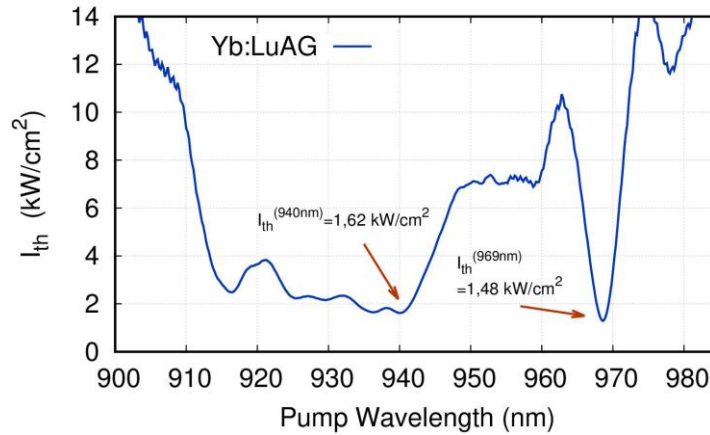


Figure 2.6: Threshold intensity required to achieve transparency at 1030 nm for Yb:LuAG as a function of the pump wavelength.

Amplified spontaneous emission

Photons which are spontaneously emitted in the bulk of the laser material are amplified via stimulated emission during the propagation in the pumped volume. For high gain cross sections $\sigma_g = \beta \cdot (\sigma_{em} - \sigma_{abs}) - \sigma_{abs}$, long geometrical extension L of the laser medium, and high doping density N , this can lead to a high gain G_{ASE} , and therefore an exponentially growing ASE signal power P_{ASE} :

$$G_{ASE} = e^{\sigma_g \cdot N \cdot L} \quad 2.6$$

$$P_{ASE} = P_{0,ASE} \cdot G_{ASE}$$

As a consequence, the upper laser level can be significantly depleted, limiting the stored energy and therefore the gain for the laser signal. In fiber amplifiers, L (the fiber length) is typically large, which causes a substantial (CW) ASE background emission [75].

On the other hand, in the thin-disk geometry, L is typically on the order of only $\sim 100 \mu\text{m}$, leading to a negligible G_{ASE} at in the z -direction. However, the lateral extension is on the order of $\sim 10 \text{ mm}$, enabling substantial ASE build-up. Additionally, the propagation along a zig-zag path due to total internal reflection at the AR-coated side of the disk can take place at an angle β that is greater than the critical angle for total internal reflection β_{TIR} . This effectively increases the maximum propagation length even beyond the disk diameter. In Figure 2.7 (a) such a zig-zag path is illustrated, starting at a spontaneous emission source in the bulk of the laser disk. At the edge of the disk, the ASE may be partially scattered, leading to a virtual source of radiation that can further propagate. If resonant, this process can even lead to transverse laser action [76]. It has been shown that, in thin-disk lasers, ASE can be responsible for considerable reduction of the maximum amount of stored energy and therefore also the gain for the laser signal [77–80].

A way to reduce the loss due to ASE is to add an undoped, refractive index-matched material to the top of the laser-active medium, see Figure 2.7 (b). Here, zig-zag propagation can still occur, but the propagation through the laser medium is partially replaced by propagation through the undoped medium. Therefore, the total gain length of ASE is reduced [80].

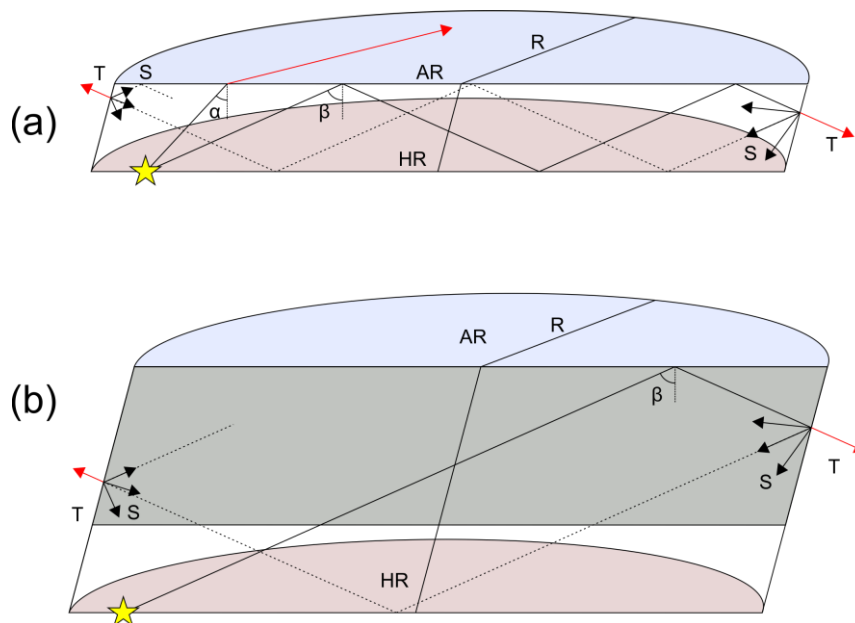


Figure 2.7: Sketch of ASE propagation in a discoidal shaped laser medium without (a) and with (b) anti-ASE cap. The yellow star marks the location of a spontaneously emitted photon propagating along the zig-zag path for $\beta > \beta_{TIR}$. If the angle of incidence at the AR face $\alpha < \beta_{TIR}$, the emission is fully transmitted.

2.1.2 Dispersion and Ultrafast Optical Pulses

The variation of the velocity of light with respect to its optical carrier frequency is called dispersion. It gives rise to a variety of rich physical phenomena, particularly in the field of ultrafast laser pulses. The different dispersion mechanisms are elaborated in this section.

2.1.2.1 Material dispersion

The wavelength dependence of the refractive index of optical materials can be derived from the Lorentz oscillator model [70]. It gives rise to a wavelength-dependence of the phase velocity of light propagating through the medium. Optical pulses consisting of a multitude of optical frequency components therefore acquire a spectral phase upon propagation through a dispersive medium. When neglecting nonlinear effects, the spectral phase grows linearly with the propagation distance.

To describe the dispersion of an optical medium, the Sellmeier coefficients can be used [81]. For a given set of Sellmeier coefficients A_1, A_2, A_3 and material resonance wavelengths $\lambda_1, \lambda_2, \lambda_3$, the wavelength dependent refractive index can be well described by:

$$n(\lambda) = \sqrt{1 + \sum_{i=1}^3 \frac{A_i \cdot \lambda^2}{\lambda^2 - \lambda_i^2}} \quad 2.7$$

Via the dispersion relation $k(\omega) = \frac{\omega}{c_0/n} = \frac{\omega}{c_0} \cdot n(\lambda)$ the dispersion coefficients D_m are then given, as detailed in section 2.1.2.2.

As an example, the curve is shown for the case of silica glass in Figure 2.8. For the calculation, the Sellmeier coefficients listed in Table 2.1 were used.

Table 2.1: Sellmeier coefficients for silica glass. Data taken from [82].

A_1	A_2	A_3	λ_1 (μm^2)	λ_2 (μm^2)	λ_3 (μm^2)
0.6961663	0.4079426	0.8974794	0.004679148	0.013512063	97.9340025

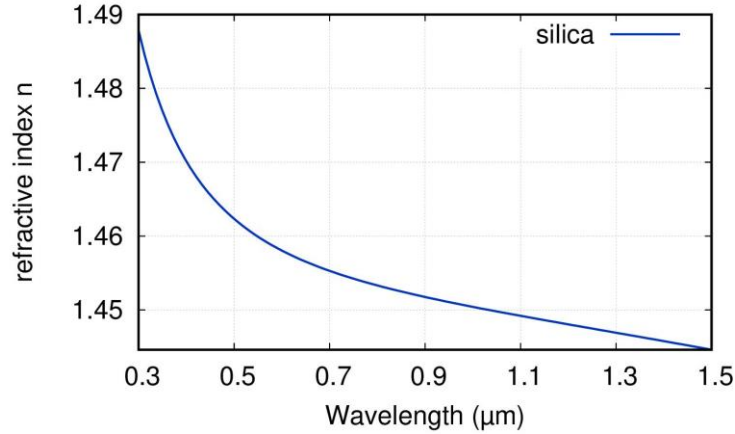


Figure 2.8: Refractive index of silica calculated with the Sellmeier coefficients from Table 2.1.

2.1.2.2 Group velocity dispersion

In the following, the velocity of optical pulses and its spectral dispersion are considered and derived. The formulae are well known and can be found in standard text books [4,69,71] [Koechner, Milonny, Boyd].

From Maxwell's equations, the well-known wave equation can be derived:

$$\left(-(\nabla)^2 + \frac{n^2}{c^2} \frac{\partial^2}{\partial t^2} \right) \vec{E}(\vec{x}, t) = \mu_0 \frac{\partial^2}{\partial t^2} \vec{P}(\vec{x}, t) \quad 2.8$$

In the one-dimensional case (propagation only in x-direction) it simplifies to:

$$\left(-\frac{\partial^2}{\partial x^2} + \frac{n^2}{c^2} \frac{\partial^2}{\partial t^2} \right) E(x, t) = \mu_0 \frac{\partial^2}{\partial t^2} P(x, t) \quad 2.9$$

Solutions to this one-dimensional wave equation are plane waves, which can be described by a superposition of sine and cosine functions, or simply a complex exponential:

$$E(x, t) = E_0(x, t) \cdot e^{i(\overbrace{kx - \omega t}^{\varphi(x,t)})} \quad 2.10$$

Here, $k = \frac{2\pi}{\lambda}$ is the wavenumber (also called propagation constant) of the wave, ω is the frequency of the wave, and E_0 is the amplitude of the electric field. Importantly, the phase $\varphi(x, t) = kx - \omega t$ of the exponential is a function of the time and space coordinate. This gives rise to the phase velocity of the wave, which is defined as the speed with which fixed phase values of the wave propagate, i.e. the distance λ traveled within one optical cycle T :

$$\frac{\lambda}{T} = \frac{2\pi/k}{2\pi/\omega} = \frac{\omega}{k} \quad 2.11$$

The phase velocity represents the propagation speed of the phase fronts of the monochromatic plane wave.

Most light sources, however, are not monochromatic and have a finite bandwidth. Moreover, for the case of ultrafast pulsed lasers, wave packets are formed through the phase-locked superposition of many longitudinal laser modes. The actual propagation of the wave packets occurs at the group velocity, which is generally different from the phase velocity for the case of dispersive media. Therefore the group velocity is the more relevant quantity for most applications.

An intuitive derivation of the group velocity is to consider a superposition of two plane waves E_1 and E_2 with slightly different frequencies, i.e. ω_1 and ω_2 , and therefore also slightly different wave numbers k_1 and k_2 :

$$E_1(x, t) = E_0 \cdot \exp(i(k_1x - \omega_1t)) \quad 2.12$$

$$E_2(x, t) = E_0 \cdot \exp(i(k_2x - \omega_2t))$$

It is useful to define the average k-vector and frequency, and the difference in k-vector and frequency:

$$\begin{aligned} k_{\text{ave}} &= \frac{(k_2 + k_1)}{2}, \\ \omega_{\text{ave}} &= \frac{(\omega_2 + \omega_1)}{2}, \\ \Delta k &= \frac{(k_2 - k_1)}{2}, \\ \Delta \omega &= \frac{(\omega_2 - \omega_1)}{2}. \end{aligned} \quad 2.13$$

Then, the superposition of E_1 and E_2 can be written as:

$$\begin{aligned} E(x, t) &= E_1(x, t) + E_2(x, t) \\ &= E_0 \cdot [\exp(i(k_1x - \omega_1t)) + \exp(i(k_2x - \omega_2t))] \\ &= E_0 \cdot \exp(i(k_{\text{ave}}x - \omega_{\text{ave}}t)) \cdot [\exp(i(\Delta kx - \Delta \omega t)) + \exp(-i(\Delta kx - \Delta \omega t))] \\ &= 2 \cdot E_0 \cdot \underbrace{\exp(i(k_{\text{ave}}x - \omega_{\text{ave}}t))}_{\text{phase oscillations}} \cdot \underbrace{\cos(\Delta kx - \Delta \omega t)}_{\text{pulse train envelope}} \end{aligned} \quad 2.14$$

As a result, the coherent superposition of the two waves E_1 and E_2 leads to a rapidly oscillating part of the E-field with the average frequency of the original waves. In addition, an envelope is

present for the E-field, whose frequency is given by the frequency difference of the original waves. Moreover, the “phase velocity of the envelope” can be calculated using the same consideration as used for equation 2.11, yielding the group velocity v_G :

$$v_G = \frac{\Delta k}{\Delta \omega} \xrightarrow{k_2 \rightarrow k_1} \frac{dk}{d\omega} = \frac{1}{dk/d\omega} \quad 2.15$$

Here, the continuous limit was considered when k_2 approaches k_1 , leading to the differential of ω with respect to k , or more commonly the inverse of the differential of k with respect to ω . In conclusion, the phase-locked superposition of plane waves leads to a signal that consists of a rapid carrier oscillation and a slowly oscillating beat envelope. The time period of the envelope corresponds to the inverse frequency distance between the individual waves of the superposition. The minimum temporal width of the wave packets corresponds to the inverse of the frequency interval covered by the individual waves. The group velocity as the propagation velocity of the wave packets is therefore relevant for the maximum speed of the transmission of energy and hence for the transmission of information. In the following, the wave packets are called pulses.

If a pulse propagates a distance L through a dispersive medium or a dispersive optical element with $k = k(\omega)$, it acquires a phase which is given by

$$\varphi(\omega) = k(\omega) \cdot L. \quad 2.16$$

The spectral phase $\varphi(\omega)$ is therefore directly related to the dispersion relation $k(\omega)$. To separate the different orders of polynomial contributions, the spectral phase can be written as a Taylor expansion around a central frequency ω_0 :

$$\begin{aligned}
 \varphi(\omega) &= \sum_{n=0}^{\infty} \frac{1}{n!} \left(\frac{d^n \varphi}{d\omega^n} \right)_{|\omega_0} \cdot (\omega - \omega_0)^n & 2.17 \\
 &= \varphi(\omega_0) \\
 &+ \underbrace{\left(\frac{d\varphi}{d\omega} \right)_{|\omega_0}}_{GD} \cdot (\omega - \omega_0) \\
 &+ \frac{1}{2} \underbrace{\left(\frac{d^2 \varphi}{d\omega^2} \right)_{|\omega_0}}_{GDD} \cdot (\omega - \omega_0)^2 \\
 &+ \frac{1}{6} \underbrace{\left(\frac{d^3 \varphi}{d\omega^3} \right)_{|\omega_0}}_{TOD} \cdot (\omega - \omega_0)^3 \\
 &+ \frac{1}{24} \underbrace{\left(\frac{d^4 \varphi}{d\omega^4} \right)_{|\omega_0}}_{FOD} \cdot (\omega - \omega_0)^4 \dots
 \end{aligned}$$

The linear term denoted as GD is called the group delay. It gives the temporal delay of the pulse due to the reduced group velocity in the dispersive medium.

The quadratic term denoted as GDD is called the group delay dispersion. It gives the variation of the group delay across the spectral components of the carrier waves.

The cubic and quartic terms called denoted as TOD and FOD are called the third- and fourth-order dispersion, and represent the higher-order variations of the group delay with respect to the optical frequency.

From a practical perspective, the n^{th} derivative of the spectral phase gives the n^{th} -order variation of the spectral phase with respect to frequency. Therefore, after traveling through a dispersive medium or dispersive optical element, the spectral phase contains the encoded information on the dispersion of the medium.

For the dispersion management of a picosecond (i.e. medium-broad band) optical system, typically the first two dispersion orders (GD, GDD) are considered :

$$\begin{aligned}
 GD &= \frac{d\varphi}{d\omega} & 2.18 \\
 &= \varphi(\omega_0) + \left(\frac{d\varphi}{d\omega} \right)_{|\omega_0} \cdot (\omega - \omega_0) + \frac{1}{2} \left(\frac{d^2 \varphi}{d\omega^2} \right)_{|\omega_0} \cdot (\omega - \omega_0)^2 \\
 &+ \frac{1}{6} \left(\frac{d^3 \varphi}{d\omega^3} \right)_{|\omega_0} \cdot (\omega - \omega_0)^3 + \frac{1}{24} \left(\frac{d^4 \varphi}{d\omega^4} \right)_{|\omega_0} \cdot (\omega - \omega_0)^4 + \dots
 \end{aligned}$$

$$\begin{aligned}
 GDD &= \frac{d^2 \varphi}{d\omega^2} & 2.19 \\
 &= \left(\frac{d\varphi}{d\omega} \right)_{|\omega_0} + \left(\frac{d^2 \varphi}{d\omega^2} \right)_{|\omega_0} \cdot (\omega - \omega_0) + \frac{1}{2} \left(\frac{d^3 \varphi}{d\omega^3} \right)_{|\omega_0} \cdot (\omega - \omega_0)^2 \\
 &\quad + \frac{1}{6} \left(\frac{d^4 \varphi}{d\omega^4} \right)_{|\omega_0} \cdot (\omega - \omega_0)^3 + \dots
 \end{aligned}$$

Often, the dispersion parameter D_λ or D_2 is used, which can be calculated from the GDD:

$$D_2 = D_\lambda = -\frac{2\pi c}{\lambda^2} \frac{d^2 \varphi}{d\omega^2} = -\frac{2\pi c}{\lambda^2} \text{GDD} \quad 2.20$$

Here, for D_λ the units of $\frac{ps}{nm}$ are used, while units of ps^2 are used for the GDD.

The group velocity dispersion (GVD) of a dispersive optical medium or element is the GDD of a pulse after propagation through it divided by the propagation length.

The knowledge of the dispersion curve of an optical system allows to design and match the overall dispersion such that the residual dispersion of the pulse after traveling through the system is eliminated. In the case of chirped-pulse amplifier systems, the pulse stretcher and compressor are chosen such as to compensate each other's dispersion and at the same time to account for any dispersion contributed by optical elements of the amplifier.

2.1.2.3 Higher-order dispersion

For optical systems that are sensitive on dispersion, higher orders of the variation of the spectral phase must be taken into account in order to achieve the desired pulse shape (i.e. in many cases the Fourier-transform limited pulse duration). This is especially applicable to very broadband spectra, where only a low GDD is required to obtain a high stretching factor, or to pulses stretched by optical elements with higher-order contributions.

The third-order dispersion is given by the third-order variation of the spectral phase across frequency. It is given by the Taylor expansion (equation 2.17):

$$\begin{aligned}
 TOD &= \frac{d^3 \varphi}{d\omega^3} & 2.21 \\
 &= \left(\frac{d^2 \varphi}{d\omega^2} \right)_{|\omega_0} + \left(\frac{d^3 \varphi}{d\omega^3} \right)_{|\omega_0} \cdot (\omega - \omega_0) + \frac{1}{2} \left(\frac{d^4 \varphi}{d\omega^4} \right)_{|\omega_0} \cdot (\omega - \omega_0)^2 + \dots
 \end{aligned}$$

Accordingly, the fourth-order dispersion can be written as:

$$\begin{aligned}
 FOD &= \frac{d^4 \varphi}{d\omega^4} & 2.22 \\
 &= \left(\frac{d^3 \varphi}{d\omega^3} \right)_{|\omega_0} + \left(\frac{d^4 \varphi}{d\omega^4} \right)_{|\omega_0} \cdot (\omega - \omega_0) + \dots
 \end{aligned}$$

Often the conversion from the dispersion orders in the frequency domain (GDD, TOD, FOD,...) to units of wavelength (D_2 , D_3 , D_4) is useful:

$$D_3 = -\frac{1}{2} \left(\frac{4 \cdot \pi \cdot c}{\lambda^3} \cdot GDD + \left(\frac{2 \cdot \pi \cdot c}{\lambda^2} \right)^2 \cdot TOD \right) \quad 2.23$$

$$D_4 = -\frac{1}{6} \left(\frac{12 \cdot \pi \cdot c}{\lambda^4} \cdot GDD + \frac{24 \cdot (\pi \cdot c)^2}{\lambda^3} \cdot TOD + \left(\frac{2 \cdot \pi \cdot c}{\lambda^2} \right)^3 \cdot FOD \right) \quad 2.24$$

2.1.2.4 Dispersive optical elements

Chirped Fiber Bragg grating

Compact dispersive optical elements can be manufactured by the UV-laser inscription of periodic refractive index structures into optical fibers, resulting in Bragg-type fiber reflectors. By varying the refractive index periodicity, chirped fiber Bragg reflectors can be realized with a designed dispersion. Typically, a maximum group delay of several nanoseconds and a power loss of ~10 % are available [83]. Such dispersive, chirped fiber Bragg gratings (CFBGs) are routinely used for dispersion compensation in fiber optics, eg in telecommunication. Furthermore, CFBGs provide a compact alternative to the grating based Martinez-type pulse

stretchers [84] commonly used in CPA laser systems. Due to their small form factor, they can be easily integrated into the seed laser via fiber splicing.

Grating compressor

Negative (anomalous) GDD can be achieved by a Treacy-type grating compressor [85]. Numerous studies have been performed on such grating compressors concerning their layout, stability, or alignment sensitivity. Details can be found in references [86–91]. In the following a review of the properties of Treacy-type grating compressors is outlined.

The grating equation relates the diffraction angle β' of a light beam at a wavelength λ from the grating in the m^{th} diffraction order to the angle of incidence α on the grating with a grating period N :

$$\sin(\beta') = \sin(\alpha) + m \frac{\lambda}{N} \quad 2.25$$

In most cases of grating compressors, to achieve a high diffraction efficiency, near-Littrow configurations are chosen, and the optimized line grating period allows only for the negative first diffraction order to exist, i.e. $m = -1$.

The spectral phase of a Treacy-type compressor can be written as:

$$\varphi(\omega) = 2 \frac{\omega}{c} D \cos(\beta_0 - \beta(\omega)) \quad 2.26$$

With the grating separation D along the propagation path of the central wavelength, the diffraction angle $\beta_0 = \beta(\omega_0)$ of the central wavelength, and the diffraction angles $\beta(\omega)$ of other wavelengths.

From equations 2.25 and 2.26, the different polynomial contributions for the spectral phase response of such a grating compressor can be calculated by the n^{th} differentiation of $\varphi(\omega)$, according to 2.17 (note a factor 2 due to the double-pass in the compressor):

$$\text{GDD} = \varphi^{(2)}(\omega_0) = - \frac{2D\lambda^3}{2 \pi c^2 N^2 \cos^2(\beta_0)} \quad 2.27$$

$$\text{TOD} = \varphi^{(3)}(\omega_0) = \frac{6D\lambda^4}{4\pi c^3 N^2 \cos^2(\beta_0)} \left(1 + \frac{\lambda \sin(\beta_0)}{N \cos^2(\beta_0)} \right) \quad 2.28$$

$$\text{FOD} = \varphi^{(4)}(\omega_0) = -\frac{6D\lambda^5}{8\pi c^4 N^2 \cos^2(\beta_0)} \left[4 \left(1 + \frac{\lambda \sin(\beta_0)}{N \cos^2(\beta_0)} \right)^2 + \left(\frac{\lambda}{N \cos^2(\beta_0)} \right)^2 \right] \quad 2.29$$

If the normal separation of the gratings $s = D \cdot \cos(\beta_0)$ is used instead of the distance along the propagation path of the central wavelength, the GDD is given by [86,90]:

$$\text{GDD} = -\frac{s\lambda^3}{\pi c^2 N^2} \frac{1}{\cos^3(\beta_{(\lambda_c)})} \quad 2.30$$

In turn, to choose the correct grating distance for a pulse with a given GDD, equation 2.27 can be solved for D :

$$D = -\frac{\pi c^2 N^2}{\lambda^3} \cos^2(\beta'_{(\lambda_c)}) \cdot \text{GDD} \quad 2.31$$

2.1.2.5 Ultrashort pulses

The generation, amplification, propagation, and application of ultrashort optical pulses provides rich physics and all aspects are active fields of research. To achieve highest peak powers, careful design of the physical aspects of ultrashort laser pulses is necessary. Here, some useful aspects are discussed.

In many cases, the temporal shape of the intensity of an optical pulse can be approximated by a Gaussian curve [68]:

$$I_{pulse}(t) = I_{peak} \cdot e^{-2\left(\frac{t}{\tau_0}\right)^2} \quad 2.32$$

Here, τ_0 is the $1/e^2$ -half-width of the temporal pulse envelope. The temporal FWHM of the pulse can be calculated from τ_0 via:

$$\Delta\tau_{FWHM} = 2 \cdot t_{FWHM} = \sqrt{2 \ln(2)} \tau_0 \approx 1.177 \tau_0 . \quad 2.33$$

As the pulse travels through a dispersive medium with a group velocity dispersion $\beta_2(\omega)$, the pulse temporally broadens. After propagation of a distance z through the medium, the temporal pulse duration can be calculated via

$$\tau(z, \beta_2) = \tau_0 \cdot \sqrt{1 + \left(\frac{z \cdot |\beta_2|}{\tau_0^2}\right)^2} . \quad 2.34$$

The energy of the pulse can be calculated by integrating over the both the temporal and spatial intensity distribution of the pulse. If assuming a Gaussian spatial mode with an $1/e^2$ -beam diameter w_0 , the pulse energy can be calculated by:

$$\begin{aligned} E_{pulse} &= \int dt \int r dr d\varphi I(r, t) & 2.35 \\ &= \int dt I_{pulse}(t) \cdot \int d\varphi \int dr r \cdot e^{-2\left(\frac{r}{w_0}\right)^2} \\ &= \sqrt{2\pi} \frac{\tau_0}{2} I_{peak} \cdot 2\pi \int dr r \cdot e^{-2\left(\frac{r}{w_0}\right)^2} \\ &= \sqrt{2\pi} \frac{\tau_0}{2} I_{peak} \cdot 2\pi \frac{\omega_0^2}{4} \\ &= \sqrt{2\pi} \cdot \frac{1}{2} \frac{t_{FWHM}}{2\sqrt{1/2 \ln(2)}} \cdot \underbrace{P_{peak}}_{P_{peak}} \\ &= \sqrt{\frac{\pi}{4 \ln(2)}} t_{FWHM} \cdot P_{peak} \end{aligned}$$

Hence, for a known pulse energy and pulse duration, the peak power can be calculated by solving equation 2.35 for P_{peak} :

$$P_{peak} = \sqrt{\frac{4 \ln(2)}{\pi}} \cdot \frac{E_{pulse}}{t_{FWHM}} \approx 0.94 \cdot \frac{E_{pulse}}{t_{FWHM}} \quad 2.36$$

Fourier Transform

The pulse described in equation 2.32 can be transformed to the frequency domain via the Fourier transformation using $E(t) = \sqrt{I(t)} = \sqrt{I_{peak}} \cdot e^{-\left(\frac{t}{\tau_0}\right)^2}$:

$$\begin{aligned}
 E(\omega) &= FT(E(t)) = \frac{1}{\sqrt{2\pi}} \int_{-\infty}^{\infty} E(t) \cdot e^{i\omega t} \propto e^{-\left(\frac{\omega}{\tau_0}\right)^2} \\
 \Rightarrow I(\omega) &= |E(\omega)|^2 \propto e^{-2\left(\frac{\omega}{\tau_0}\right)^2}
 \end{aligned}
 \tag{2.37}$$

The following conclusions can be drawn:

- (i) The spectral intensity of a Gaussian pulse has a Gaussian shape
- (ii) The spectral FWHM $\Delta\nu_{FWHM}$ can be calculated from the FWHM pulse duration:

$$2\pi \cdot \Delta\nu_{FWHM} = \sqrt{2 \ln(2)} \cdot \tau_0 = \sqrt{2 \ln(2)} \cdot \frac{2}{\tau_0} = \sqrt{2 \ln(2)} \cdot \frac{2 \cdot \sqrt{2 \ln(2)}}{\Delta\tau_{FWHM}} = \frac{4 \ln(2)}{\Delta\tau_{FWHM}}
 \tag{2.38}$$

Hence, the spectral intensity width of the Gaussian pulse is inversely proportional to the temporal pulse duration τ_0 .

- (iii) The (FWHM-) time-bandwidth product of the a Gaussian pulse is given by:

$$\Delta\nu_{FWHM} \cdot \Delta\tau_{FWHM} = \frac{4 \ln(2)}{2\pi} \approx 0.441.
 \tag{2.39}$$

2.1.3 Optical Resonators

A simple model for an optical resonator is given by two spherical mirrors M_1 and M_2 with radii of curvature R_1 and R_2 , that are placed at a distance L from each other (see Figure 2.9). For a Gaussian beam to be stable inside the resonator, the wavefront curvatures of the beam at the mirror positions must match R_1 and R_2 . Depending on R_1 , R_2 , and L , the beam waist radius ω_0 , the beam radii ω_1 and ω_2 at the resonator mirrors, and the position of the waist between the mirrors t_1 and t_2 can be derived [72,92]:

$$\omega_1^4 = \left(\frac{\lambda R_1}{\pi}\right)^2 \cdot \frac{R_2 - L}{R_1 - L} \cdot \frac{L}{R_1 + R_2 - L}
 \tag{2.40}$$

$$\omega_2^4 = \left(\frac{\lambda R_2}{\pi}\right)^2 \cdot \frac{R_1 - L}{R_2 - L} \cdot \frac{L}{R_1 + R_2 - L} \quad 2.41$$

$$\omega_0^4 = \left(\frac{\lambda}{\pi}\right)^2 \cdot \frac{L \cdot (R_1 - L)(R_2 - L)(R_1 + R_2 - L)}{(R_1 + R_2 - 2L)^2} \quad 2.42$$

$$t_1 = \frac{L \cdot (R_2 - L)}{R_1 + R_2 - 2L} \quad 2.43$$

$$t_2 = \frac{L \cdot (R_1 - L)}{R_1 + R_2 - 2L} \quad 2.44$$

Commonly, the stability of such a resonator can be assessed by the stability criterion:

$$0 \leq g_1 g_2 \leq 1 \quad 2.45$$

with

$$g_{1,2} = 1 - \frac{L}{R_{1,2}}.$$

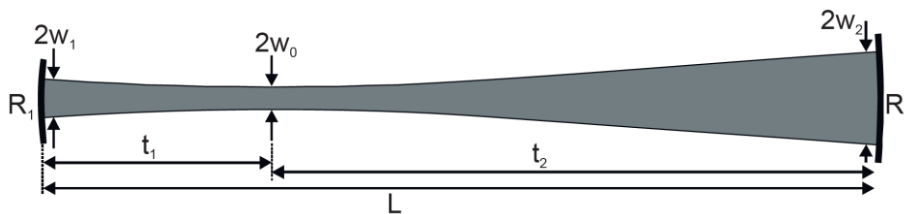


Figure 2.9: Sketch of an optical resonator consisting of two spherical mirrors. Figure taken from [91].

2.1.4 Beam Quality

Many optical resonators are optimized for the fundamental transverse laser mode. The divergence of this mode is minimal, enabling small focal beam diameters and therefore high power densities and high brightness. This is useful for many applications.

For the fundamental mode (TEM₀₀) of a Gaussian beam, the beam radius at a position z from the waist is given by [71]:

$$\omega(z) = \omega_0 \sqrt{1 + \left(\frac{z}{z_0}\right)^2} . \quad 2.46$$

Here, z_0 is the Rayleigh length, which is given by

$$z_0 = \frac{\pi \omega_0^2}{\lambda} . \quad 2.47$$

The divergence angle θ can then be calculated as

$$\theta = \frac{\lambda}{\pi \omega_0} . \quad 2.48$$

For most real resonators, often higher-order modes are oscillating above the laser threshold, too, altering the divergence angle for a given focal waist ω_0 . For a given transverse Hermite-Gaussian mode with the orders m and n , TEM_{mn}, the divergence angle increases by a factor $M_{x(y)}^2 = \sqrt{1 + 2m(n)}$, respectively in the x and y directions. The parameter M^2 is called the beam quality parameter. To determine the beam quality parameter of an experimental laser beam, a method described in the ISO standard 11146 can be used. Here, the beam waist diameters $\omega(z)$ are measured at several distances z from the focus position. The beam quality parameter M^2 is then obtained by fitting equation 2.49 to the data via M^2 , where z_0 is replaced with $z_{0,M^2} = z_0/M^2$:

$$\omega(z) = \omega_0 \sqrt{1 + \left(\frac{z}{z_{0,M^2}}\right)^2} . \quad 2.49$$

2.2 Basics of Nonlinear Optics

Nonlinear polarization

The polarization invoked by light traveling through a medium gives rise to the phenomena of nonlinear optics. Depending on the symmetry of the material, different types of nonlinear

processes can take place. In this section the basics for important nonlinear effects are detailed, as described in many text books [68,69,71].

The left-hand side of the wave equation 2.9 describes the electric field of the initial electromagnetic wave traveling through the medium. The right-hand side describes the polarization of the medium invoked by the electromagnetic wave. Depending on the material, the polarization can contain nonlinear components, which is due to its characteristic nonlinear susceptibility χ . In general, the susceptibility is a three-dimensional tensor, which accounts for the three-dimensionality of the optical material. Here the one-dimensional case is described, which is valid for one certain alignment between the incident wave and the nonlinear material. A Taylor expansion for the susceptibility can be used to describe the response of the polarization of the material to the electric field. The resulting nonlinear susceptibility coefficients $\chi^{(n)}$ with $n \geq 2$ can then be used to calculate the nonlinear material polarization:

$$P_{NL}(x, t) = \sum_n P_{NL}^{(n)} = \sum_n \epsilon_0 \chi^{(n)} E^n(x, t) \quad 2.50$$

Depending on the symmetry of the material, the even or odd elements of $\chi^{(n)}$ vanish due to symmetry conditions. For non-centro-symmetric materials, all odd contributions vanish, so the lowest nonlinear contribution is of second order. In turn, for centro-symmetric materials, all even contributions vanish, leaving the third order as the lowest nonlinear contribution n .

Second order nonlinear effects

The second order nonlinear polarization for an incident field $E(x, t) = E_0 e^{i\omega t}$ is given by

$$\begin{aligned} P_{NL}^{(2)}(x, t) &= \epsilon_0 \chi^{(2)} E^2(x, t) \\ &= \epsilon_0 \chi^{(2)} E_0^2 e^{i2\omega t} \end{aligned} \quad 2.51$$

This means, that a light wave with frequency 2ω is generated due to the quadratic dependence of the material polarization on the electric field of the driving wave. This phenomenon is called second harmonic generation (SHG).

Other second-order nonlinear effects occur, if multiple (≥ 2) light waves are applied together to the nonlinear material, eg. $E_1(x, t) = E_1 e^{i\omega_1 t} + cc.$ and $E_2(x, t) = E_2 e^{i\omega_2 t} + cc.$ Then $P_{NL}^{(2)}$ is given by:

$$\begin{aligned}
 P_{NL}^{(2)}(x, t) &= \epsilon_0 \chi^{(2)} \left(E_1(x, t) + E_2(x, t) \right)^2 & 2.52 \\
 &= \epsilon_0 \chi^{(2)} \left(\underbrace{E_1^2 e^{i2\omega_1 t}}_{SHG} + \underbrace{E_2^2 e^{i2\omega_2 t}}_{SHG} + \underbrace{2E_1 E_2 e^{i(\omega_1 + \omega_2)t}}_{SFG} + \underbrace{2E_1 E_2^* e^{i(\omega_1 - \omega_2)t}}_{DFG} \right. \\
 &\quad \left. + \underbrace{(E_1 E_1^* + E_2 E_2^*)}_{OR} \right)
 \end{aligned}$$

Hence, in addition to the SHG of the two input frequencies, the sum frequency (SFG) and difference frequency (DFG) are generated due to the material response. A static component with frequency $\omega = 0$ is also created, called optical rectification (OR).

Third-order nonlinear effects

The third-order nonlinear polarization for an incident field consisting of three waves $E_j(x, t) = E_j e^{i\omega_j t}$, with $l = 1, 2, 3$, gives rise to the third-order nonlinear processes. When sorting the contributions for their frequencies ω_j , the nonlinear polarization is given by:

$$\begin{aligned}
 P_{NL}^{(3)}(x, t) &= \epsilon_0 \chi^{(3)} \left(E_1(x, t) + E_2(x, t) + E_3(x, t) \right)^3 & 2.53 \\
 &= \epsilon_0 \chi^{(3)} \left(\underbrace{\sum_j |E_j|^2 E_j e^{i\omega_j t}}_{SPM (TPA)} + \underbrace{\sum_j E_j^3 e^{i3\omega_j t}}_{THG} + \underbrace{\sum_{j,k,l} (|E_j|^2 + |E_k|^2) E_l e^{i\omega_l t}}_{XPM} \right. \\
 &\quad \left. + \underbrace{\sum_{\substack{j,k,l \\ w/o \ j=k=l}} E_j E_k E_l e^{i(\omega_j + \omega_k + \omega_l)t}}_{FWM} \right)
 \end{aligned}$$

Note that the complex conjugates of the electric fields are not written out for simplicity, but must be considered for the complete evaluation of $P_{NL}^{(3)}(x, t)$.

The most important effects in the context of high-power and high-intensity lasers stem from the first term of equation 2.53. They are discussed in the following.

Optical Kerr Effect

The contributions of $P_{NL}^{(3)}(x, t)$ with one of the input frequencies $\omega_1, \omega_2, \omega_3$ lead to an effective modulation of the susceptibility and hence a modulation of the refractive index of the material. This effect is often referred to as the optical Kerr effect [93]. It can be derived by calculating the total polarization P^{TOT} for a centrosymmetric medium, as induced by a monochromatic wave with frequency ω :

$$\begin{aligned} P^{TOT}(\omega) &= P^{LIN} + P^{NL} = \epsilon_0 \chi^{(1)} E(\omega) + 3\epsilon_0 \chi^{(3)} |E(\omega)|^2 E(\omega) \\ &= \epsilon_0 \underbrace{(\chi^{(1)} + 3\chi^{(3)} |E(\omega)|^2)}_{\chi^{(eff)}} E(\omega) \end{aligned} \quad 2.54$$

Using the definition of the refractive index $n_{eff}^2 = 1 + \chi^{(eff)}$, the refractive index can be written as a function of the time-averaged intensity of the optical field $I(x, t) = 2n_0 \epsilon_0 c |E(\omega)|^2$:

$$n_{eff} = n_0 + n_2 \cdot I(x, t), \quad 2.55$$

with the nonlinear refractive index

$$n_2 = \frac{3}{4n_0^2 \epsilon_0 c} \text{Re}(\chi^{(3)}). \quad 2.56$$

The optical Kerr effect gives rise to important phenomena of nonlinear optics, including self-phase modulation (SPM) and self-focusing (SF) of laser beams. SF will be discussed in more detail in section 2.3. SPM is an instantaneous modulation of the temporal phase due to the varying intensity of a pulsed laser signal, that can cause significant spectral broadening of the input spectrum of the pulse. As an example, consider an unchirped, Gaussian pulse, according to equation 2.32, $I(t) = I_{peak} \cdot e^{-2\left(\frac{t}{\tau_0}\right)^2}$. Then the real part of the refractive index is given according to equation 2.55 and leads to a modulated propagation constant k :

$$\begin{aligned}
 k(\omega_0) &= \frac{\omega_0}{c} \cdot n_{eff} & 2.57 \\
 &= \frac{\omega_0}{c} n_0 + \frac{\omega_0}{c} n_2 \cdot I(x, t) \\
 &= k_0 + \frac{\Phi_{NL}}{z}
 \end{aligned}$$

with $\Phi_{NL} = z \cdot \frac{\omega_0}{c} n_2 \cdot I(x, t)$.

The resulting temporal phase $\varphi(t) = \omega_0 t - k(\omega_0)z$ is thus modulated by the instantaneous optical field intensity $I(x, t)$. For the case of the Gaussian pulse shape, this leads to a modulated instantaneous frequency $\omega(t)$:

$$\begin{aligned}
 \omega &= -\frac{\partial \varphi}{\partial t} & 2.58 \\
 &= \omega_0 - \frac{\partial}{\partial t} \Phi_{NL} \\
 &= \omega_0 - \frac{\omega_0 n_2}{c} \frac{dI(x, t)}{dt} \\
 &= \omega_0 + \frac{\omega_0 n_2}{c} \cdot 4 I_{peak} \frac{t}{\tau_0^2} e^{-2\left(\frac{t}{\tau_0}\right)^2}
 \end{aligned}$$

The effect of SPM on a Gaussian pulse is qualitatively plotted in Figure 2.10. In panel (a), the instantaneous frequency shift is overlaid with the Gaussian intensity shape. In panel (b) the electric field oscillations of the phase-modulated pulse are shown.

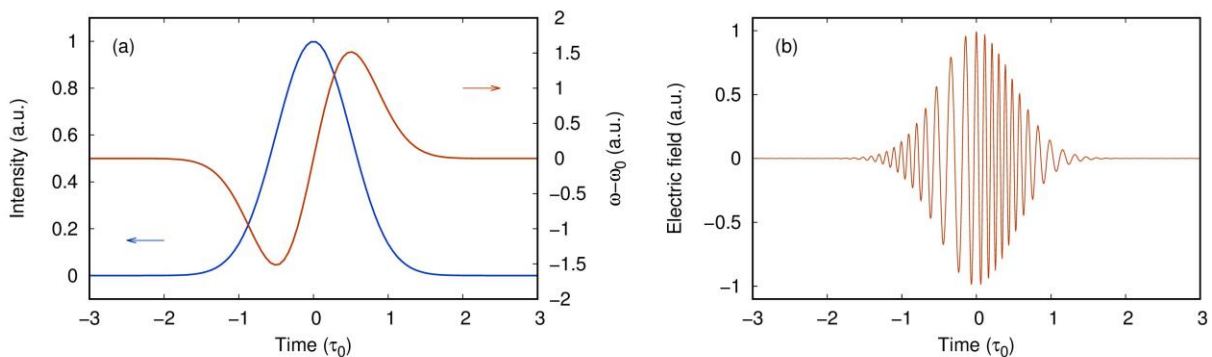


Figure 2.10: Illustration of self-phase modulation. (a) The initial pulse with a Gaussian shape leads to a frequency modulation dependent on the slope of the pulse edges. (b) The frequency modulation leads to red-shifted frequencies generated at the leading edge of the pulse, and blue-shifted frequencies generated at the trailing edge of the pulse.

Two-photon absorption (TPA)

Any imaginary contributions of $\chi^{(3)}$ in the first term of equation 2.53 have an influence on the imaginary part of the refractive index and therefore give rise to TPA instead of SPM. As a consequence, the absorption coefficient α depends on the intensity of the optical field:

$$\alpha_{eff} = \alpha_0 + \alpha_2 \cdot I, \quad 2.59$$

where the nonlinear absorption coefficient α_2 is given by the imaginary part of $\chi^{(3)}$:

$$\alpha_2 = \frac{-3\omega}{2n_0^2\epsilon_0c^2} \text{Im}(\chi^{(3)}). \quad 2.60$$

2.3 Filamentation and Breakdown of Optical Pulses

Self-focusing

Next to the above described mechanism of self-phase modulation, the optical Kerr effect also gives rise to the phenomenon of self-focusing of a laser beam. For a spatially inhomogeneous beam profile, the nonlinear refractive index is modified according to equation 2.55 across the beam profile. If $n_2 > 0$, then the lateral refractive index profile corresponds to a positive lens, that is self-enhanced as the beam narrows. As a result, the beam is focused upon propagation through the transparent nonlinear material, as shown in Figure 2.11.

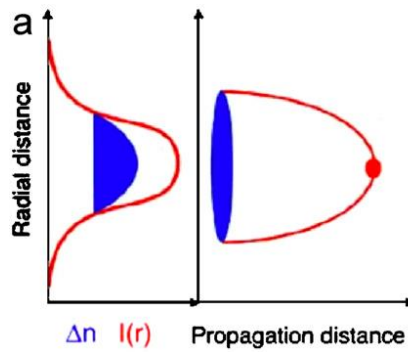


Figure 2.11: Illustration of the effect of self-focusing in a transparent nonlinear material. The radial intensity distribution $I(r)$ leads to a positive lens if $n_2 > 0$. Figure taken from [11].

To overcome diffraction, the peak power of the laser pulse must exceed a critical power. For the case of a Gaussian beam profile the critical power for self-focusing is given by [11]:

$$P_{\text{crit}} = \frac{3.77 \cdot \lambda_0^2}{8\pi \cdot n_0 n_2} \quad 2.61$$

For the case of propagation in air under normal atmospheric conditions, $n_0 = 1$ and $n_2 \approx 3 \cdot 10^{-23} \frac{\text{m}^2}{\text{W}}$, [11,14] which leads to a critical power of $\approx 5 \text{ GW}$ at a wavelength of $\lambda_0 = 1030 \text{ nm}$ [94]. Importantly, it is the peak power of the laser pulse (instead of the peak intensity) that eventually leads to the collapse of an initially collimated beam at a distance L_c , which is dependent on the Rayleigh length L_{DF} of the beam [95]:

$$L_c = \frac{0.367 \cdot L_{DF}}{\sqrt{\left[\left(\frac{P_{in}}{P_{crit}} \right)^{\frac{1}{2}} - 0.852 \right]^2 - 0.0219}} \quad 2.62$$

For non-collimated beams, the distance until beam collapse is altered. If the beam is passing through an additional lens with a focal length f , then the collapse distance is given by:

$$\frac{1}{L_{c,f}} = \frac{1}{L_c} + \frac{1}{f}. \quad 2.63$$

Filamentation

The self-focusing effect of laser beams leads to increased optical intensities as the beam diameter decreases. Eventually, this leads to ionization of the transparent medium, first via multi-photon ionization and at higher via intensities tunnel ionization. Due to the radial gradient of the density of the generated plasma $\rho(r, t)$, the effective refractive index is modulated and reduced at the center of the laser beam [96]:

$$n \approx n_0 - \frac{\rho(r, t)}{2\rho_{crit}}. \quad 2.64$$

Here, the critical plasma density ρ_{crit} gives the threshold above which the plasma becomes opaque for the laser light, and is given by:

$$\rho_{crit} = \epsilon_0 m_e \omega_0 / e^2 \quad 2.65$$

where ϵ_0 is the vacuum permittivity, m_e is the electron mass, ω_0 is the frequency of the electromagnetic wave, and e is the electron charge.

As a consequence, thin plasma channels can be formed in transparent media, enabled by the balance between the Kerr self-focusing effect and the defocusing effect due to the generated plasma. An illustration is shown in Figure 2.12. Interestingly, the intensity reached within the core of a filament is clamped due to locally saturated self-focusing at the center of the filament, which causes local defocusing and thereby limits the reached intensity [97]:

$$I \approx \frac{0.76 n_2 \rho_c}{\sigma_K t_p \rho_{at}}. \quad 2.66$$

The diameter of the filament is then given by [10,98]:

$$\omega_0 \approx \left(\frac{2P_{crit}^{Gauss}}{\pi \cdot I} \right)^{\frac{1}{2}}, \quad 2.67$$

which give a value of $\omega_0 \approx 100 \mu m$ for a laser pulse at a wavelength of 1030 nm filamenting in air. The clamped intensity I has been shown to lead to an amount of power contained in a filament close to the P_{crit} .

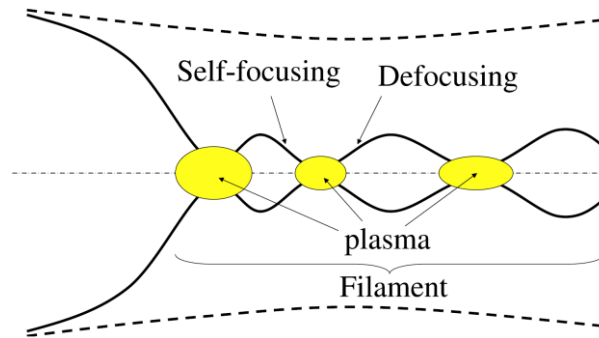


Figure 2.12: Balance between Kerr self-focusing and plasma defocusing in filaments. Figure taken from [11].

The nature and theoretical description of laser filaments has been studied and summarized in several books and review papers since their first demonstration in 1995 [10] [11,12,14,99,100]. While the first demonstration of filamentation of ultrashort laser pulses occurred in a laboratory environment, filaments extending over hundreds of meters have been demonstrated in open-air experiments [29,101].

Multifilamentation

For laser pulses exceeding by far the critical power P_{crit} given in equation 2.61, the spatial frequencies (noise) present in the transverse laser beam profile lead to the formation of multiple filaments within the beam profile due to a spatial modulational instability (MI) effect [11]. For pulsed laser beams with a Gaussian profile, the threshold peak power P_{MI} for the MI effect starting from spatial intensity noise was reported to be approximately $P_{MI} \approx 100 \cdot P_{crit}$ [102]. The total number of filaments N_{fil} can then be estimated from the ratio of the total peak power P_{Laser} and the critical power P_{crit} [103]:

$$N_{fil} \approx \frac{P_{Laser}}{5 \cdot P_{crit}}. \quad 2.68$$

3 Front-End

The front-end of the developed laser system acts as a stable source of medium-energy laser pulses for further amplification in the main amplifier. It consists of the seed oscillator and the first high-power regenerative amplification stage. For the complete multi-stage CPA system, the front end represents a key component to achieve the Joule-level, kilowatt-class ultrafast laser output. It will be presented in this chapter.

3.1 Seed Laser

As an industrial-grade ultrafast laser, the Trumpf TruMicro2000 series was chosen as the seed laser for the amplifier chain [104]. It is a fiber-based ultrafast laser typically used for micromachining. The advantages of the seed source are its compactness and the industry-proven reliability with turn-key operation and an internal monitoring system. Several thousand operating hours can be achieved without significant maintenance. A photograph of an industrial TruMicro2000 is shown in Figure 3.1 (b).

To adapt the industrialized TruMicro2000 as a seed laser suitable for the following CPA amplifier chain, it was equipped with a chirped fiber Bragg grating that temporally chirps the ultrafast pulses from the mode-locked oscillator. The output spectrum after passing the CFBG is shown in Figure 3.1 (a). At the output, the seed pulses can reach an energy of up to 100 μJ , and the repetition rate is reduced to 1 kHz via an external AOM. To facilitate the alignment of the laser system, the repetition rate of the TruMicro2000 can be increased up to 100 kHz, resulting in an average power up to 10 W.

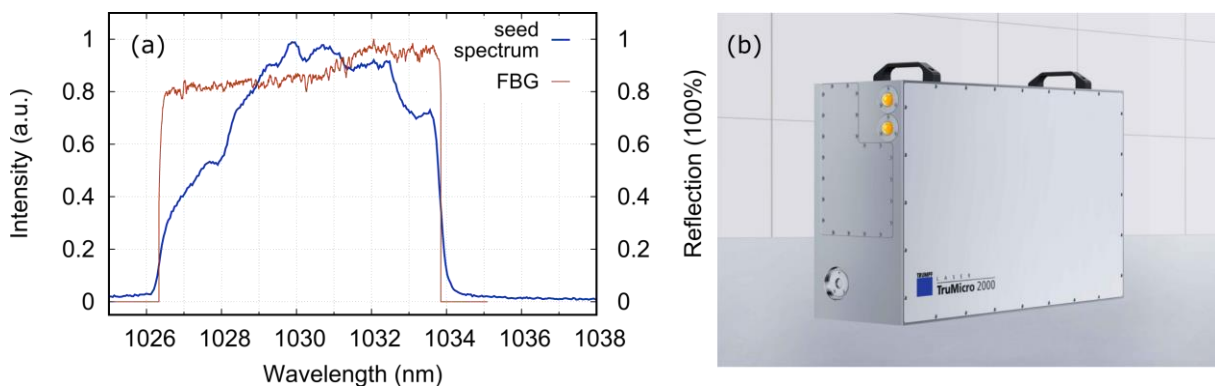


Figure 3.1: Characteristics of the seed laser. (a) Spectrum of the seed laser pulses after passing the chirped fiber Bragg grating. (b) Photograph of a TruMicro2000 micromachining laser [104] (Courtesy of TRUMPF Laser GmbH).

3.2 Regenerative Amplifier

The regenerative amplifier is used to pre-amplify the laser pulses to an energy of up to 240mJ. The main design aspects were first conceived by TRUMPF Scientific Lasers GmbH & Co. KG in 2015 [105] and similar systems are commercially available with the Dira series. Within the scope of this thesis, a regenerative amplifier based on the Dira series was built up with some modifications to adapt and optimize the system to function as a front end for the multipass amplifier. The core design aspects are summarized in this chapter.

Overview of the regenerative amplifier

The schematic layout of the regenerative amplifier is shown in Figure 3.2. The main components of the system are the seed oscillator, the thin-disk laser head, the Pockels cell, the amplifier cavity, and the timing unit. Within each roundtrip inside the cavity, the pulses are amplified by passing through the active laser disk. The breadboard-type laser board therefore enables flexible alignment and implementation of different folded cavity designs.

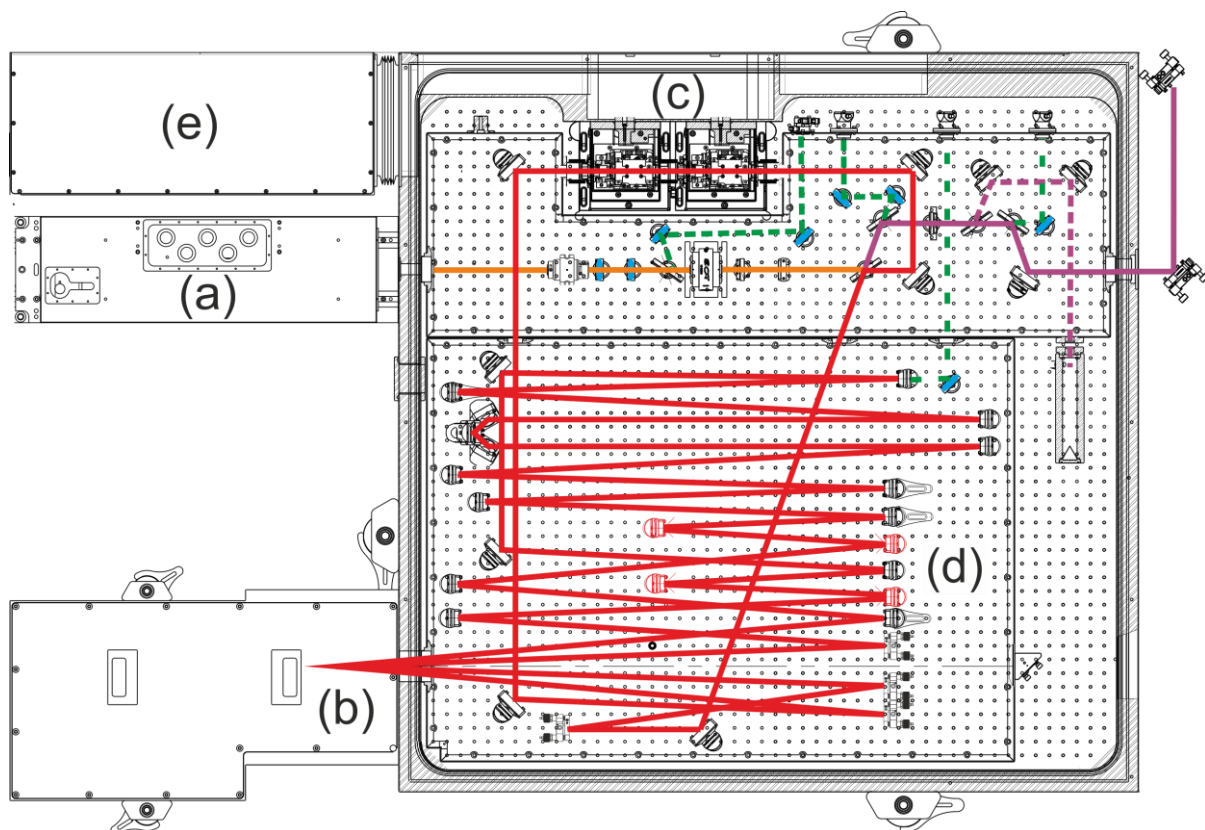


Figure 3.2: Layout of the regenerative amplifier. The beam path the seed in-coupling is marked in yellow. The pulses are then amplified in the cavity marked in red. After polarization switching by the Pockels cell, the pulses follow the output beam path marked in purple. (a) Seed oscillator. (b) Thin-disk laser head. (c) Pockels cell. (d) Amplifier cavity. (e) Timing unit.

Cavity design

The cavity of the regenerative amplifier has to fulfil the following requirements:

- The resonator must be designed to be stable for the chosen minimum beam size.
- The thermal lens of the thin-disk induced by the pump must be supported within the stability range of the resonator.
- The beam diameter inside the resonator must be sufficiently large not to exceed the laser-induced damage threshold of the involved optics (thin-disk, Pockels cell, thin-film polarizer, mirrors).

To meet these conditions, the main degrees of freedom when designing the cavity are

- the focal lengths of intracavity telescope mirrors,
- the mounting radius of curvature (ROC) of the thin-disk
- the distances between the curved optics.

A design was found to be both theoretically and experimentally stable using telescope mirror focal lengths of $f_{\text{cav}} = -10.0$ m and $f_{\text{vex}} = 10.0$, a disk mounting radius of $\text{ROC}_{\text{disk}} = 20$ m a cavity length of approximately 22 meters results, while the beam diameter is maintained above 3.5 mm within the cavity. The cavity design is shown in Figure 3.3.

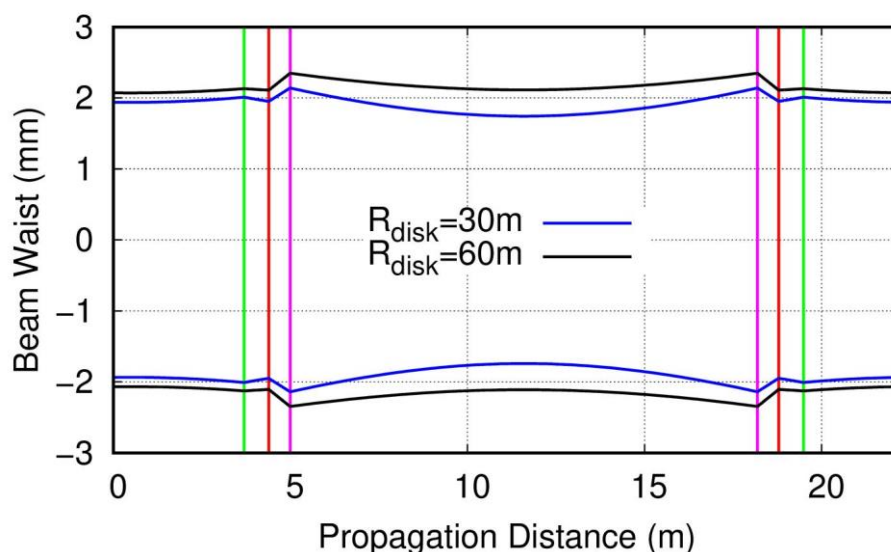


Figure 3.3: Design of the resonator of the regenerative amplifier. The beam diameter is plotted as a function of the propagation distance inside the cavity for a thin-disk ROC of 30 m (low pump power) and 60 m (high pump power). The positions of the disk reflection are marked in green, the positions of the Telescope mirrors are marked in red (convex) and purple (concave).

Pump source

The power required to pump the regenerative amplifier is delivered by two high-power InGaAs laser diode stack modules provided by TRUMPF Laser GmbH. Each pump module can deliver up to 2 kW of optical power, resulting in a maximum total pump power of $P_{Peak} = 4$ kW. The pump energy provided within a duration of t_{pump} is therefore $E_{Pump} = t_{pump} \cdot P_{Peak}$, scaling linearly with the pump duration and the peak pump power. Since the available pump power is sufficiently large to provide a multiple of the required pump energy within less than the inverse of the repetition frequency of 1 kHz, the pump diodes are driven in pulsed mode. In this way, the time interval where the upper energy level is occupied is minimized, which reduces the average rate of nonradiative decay processes and therefore the heat generated in the laser crystal. The difference between cw-pumping and pulsed pumping are schematically visualized in Figure 3.4. As a rule of thumb, the pump pulse duration must be significantly shorter than the relaxation time of the employed laser medium in order to reduce the amount of generated heat.

Performance optimization

The dynamics of regenerative amplifiers have been subject to several studies in the last years [106–108]. The initially exponential growth of the pulse energy inside the regenerative amplifier as a function of the number of intracavity roundtrips is flattened when approaching the saturation fluence of the laser gain material at the current pump power. To meet the optimum point of operation, the number of roundtrips has to be traded off with the pump power, in order to achieve

- (i) a high pulse energy as desired for experimental applications, with
- (ii) as few roundtrips as possible to minimize the cumulated B-integral, while
- (iii) maximum pulse-to-pulse energy stability is achieved, and
- (iv) the thermal influence is minimized by minimizing the pump power.

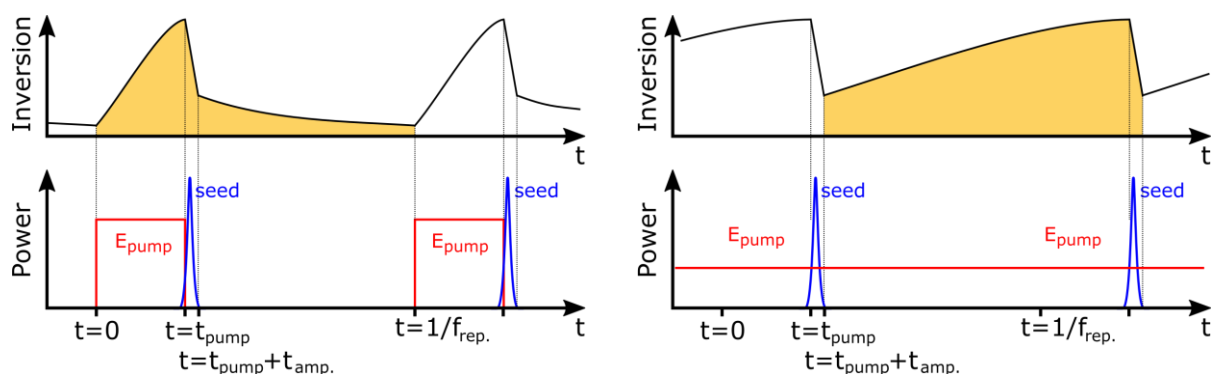


Figure 3.4: Visualization of pulsed pumping vs. cw pumping.

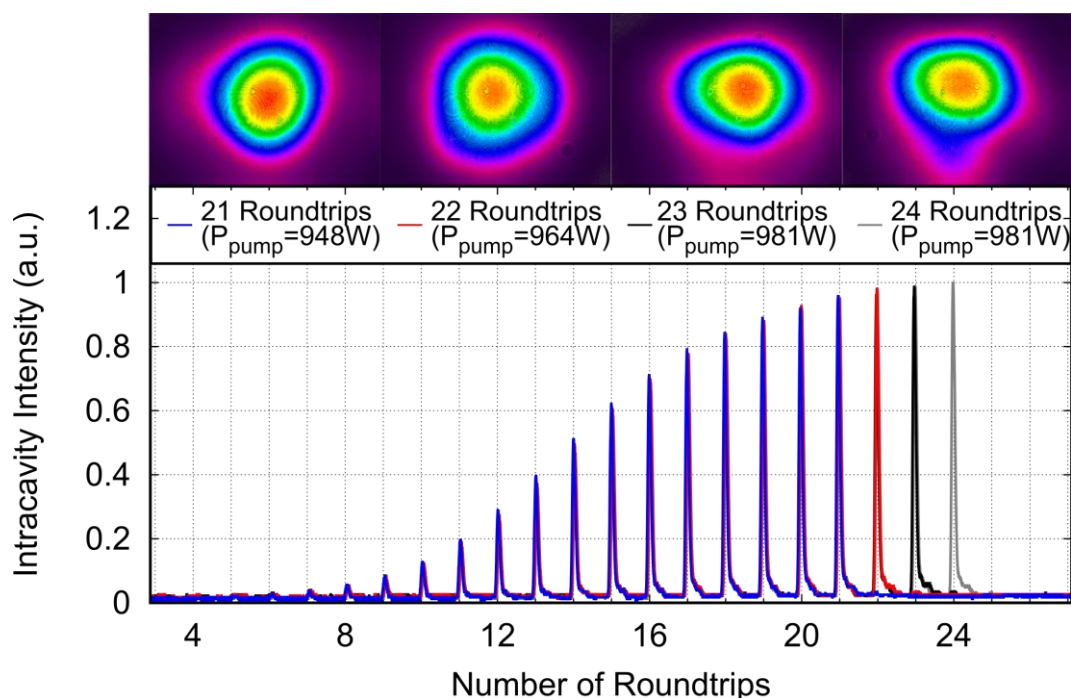


Figure 3.5: Amplification with different numbers of roundtrips. On the top the corresponding collimated output beam profiles are shown.

In practice, the pulses should perform as few roundtrips as possible while already being at high energy, in order to minimize the cumulated B-integral. On the other hand, by reducing the number of roundtrips, the pump power has to be increased and thermal wavefront distortions are provoked by the thermal load of the thin-disk. To find an optimum operation point, the number of roundtrips was swept from 21 to 24. At the same time, the pump power was adapted in order to maintain 240 mJ of final pulse energy. In Figure 3.5 the intracavity pulse build-up signal measured with a photodiode is shown as a function of the number of roundtrips. For each number of roundtrips, the pump power was adapted in order to achieve 240 mJ of pulse energy. The traces are re-scaled and overlaid for clarity. From the photodiode traces it can be seen that during the last two to three roundtrips, the pulses are circulating inside the cavity with only marginal energy gain. As a result, the corresponding near-field beam profiles are deformed with respect to a fundamental Gaussian mode due to phase distortions, accumulated from the thin-disk and the Pockels-cell crystals. The settings with 21 roundtrips were therefore chosen for the final point of operation.

Performance characteristics

The characteristics of the regenerative amplifier at the chosen operation point are detailed in the following. In Figure 3.6 (a) the output pulse energy is plotted as a function of the pump

energy, measured using a calibrated photodiode. The optical efficiency is calculated by the

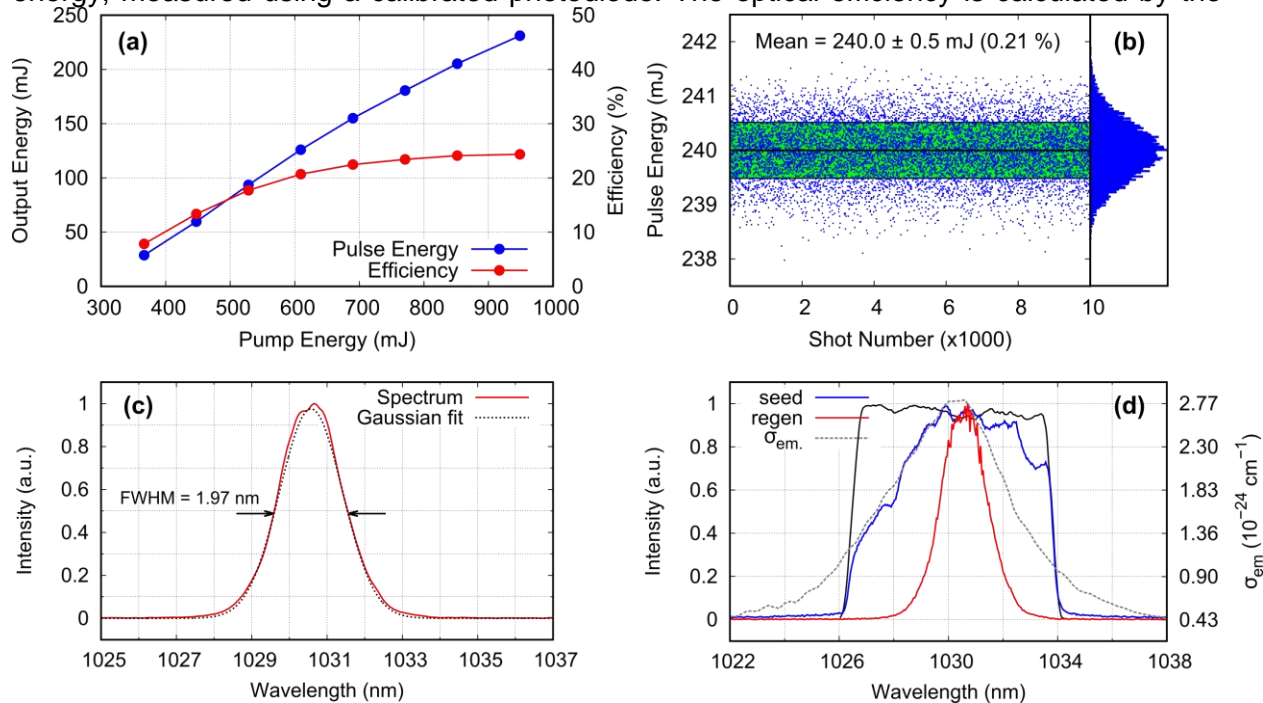


Figure 3.6: Amplification characteristics of the regenerative amplifier. (a) Amplification slope and optical efficiency, measured by a calibrated photodiode. (b) Pulse-to-pulse energy stability of 10,000 consecutive shots, measured with a calibrated photodiode. (c) Spectrum of the output pulses measured with a grating spectrometer. (d) Evolution of the spectrum before (seed) and after (regen) amplification. The transmission of the FBG is included to illustrate the cut-off on the long-wavelength side. The spectral emission cross section of Yb:LuAG is overlaid and refers to the right-hand ordinate.

ratio between average output power and average pump power. 240 mJ are achieved at a pump energy of 950 mJ, translating to an optical efficiency slightly above 25 %. The fast-time pulse energy stability from 10,000 consecutive pulses was also measured using a calibrated photodiode. The result is shown in Figure 3.6 (b). The green area marks the standard deviation of the distribution (0.21 %), which follows a Gaussian, as shown on the right hand side of the figure. After amplification to 240 mJ, the spectrum of the output pulses was measured using a grating spectrometer, as shown in Figure 3.6 (c). By fitting a Gaussian curve to the measured data, a spectral bandwidth of 1.97 nm (FWHM) is obtained for the output pulses of the regenerative amplifier. For comparison, the spectrum of the seed pulses and the spectral transmission of the (FBG) are included in Figure 3.6 (d). It can be seen that the center of the output spectrum is shifted towards the peak of the gain spectrum of the employed Yb:LuAG gain material at room temperature. In addition, the spectrum is narrowed significantly due to the gain peak.

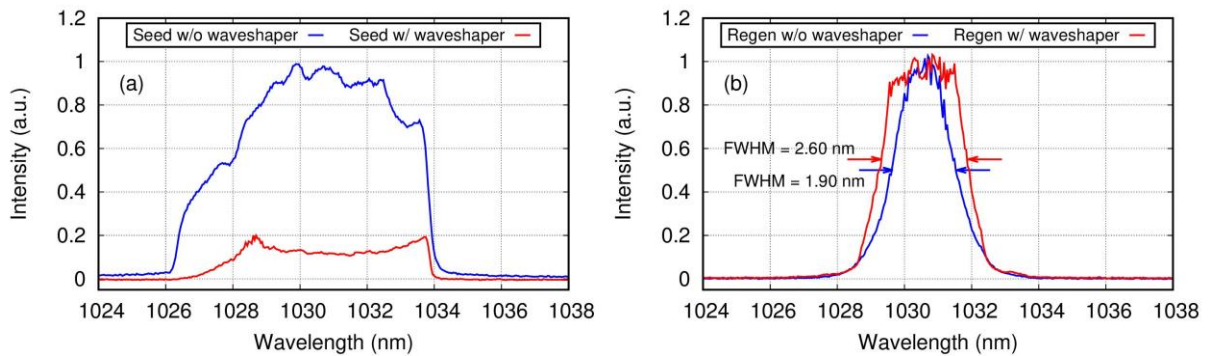


Figure 3.7: Spectral pre-shaping of the seed pulses to compensate for the gain narrowing. (a) Spectra of the seed pulse with and without shaping. (b) Spectra of the amplified output pulses with and without spectral pre-shaping. A bandwidth increase of 37 % is achieved.

Spectral pre-shaping

An attempt to counteract the observed gain narrowing was performed using a spectral light modulator (SLM). The spectral intensity of the seed pulses was pre-shaped with the SLM so as to pre-compensate for spectral evolution during pulse amplification [109]. In Figure 3.7 the spectra of the seed pulses and the spectra of the amplified pulses at 208 mJ are shown both with and without spectral pre-shaping. By attenuating the seed pulses in the spectral region around the peak of the spectral gain, a broader spectral intensity distribution is obtained after pulse amplification. The spectral bandwidth of the output pulses from the regenerative amplifier could be increased by 37 % from 1.90 nm to 2.6 nm using this technique.

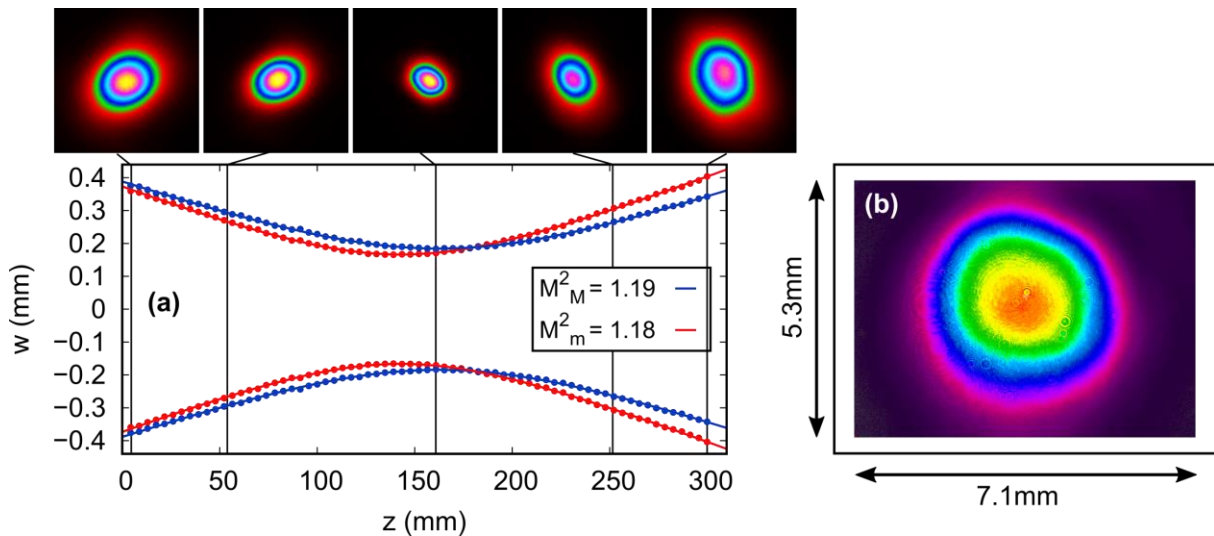


Figure 3.8: M^2 measurement of the uncompressed output of the regenerative amplifier. (a) The measured beam diameter in the major and minor axis show an M^2 parameter of 1.19 and 1.18, respectively. On the top, the beam profiles at the indicated z -positions are shown. (b) Near-field beam profile at the output of the regenerative amplifier.

Beam quality of the regenerative amplifier

Enabled by the one-dimensional heat flow in the back-side cooled laser disk, the beam quality of thin-disk based regenerative amplifiers can typically approach close to the diffraction-limit of fundamental mode Gaussian beams. To quantify the beam quality, M^2 measurements according to the ISO 11146 standard [110] were performed using a home-built setup including a motorized linear stage and a high dynamic-range CCD camera. Evaluation of the beam diameters was performed using the second moment method [111] and using the beam diameters along the determined major and the minor axes (not X and Y directions). A typical M^2 measurement is shown in Figure 3.8. By fitting the model to the data with the M^2 , w_0 and z_0 as free parameters, a beam quality of $M^2_{\text{Maj.}} = 1.19$ and $M^2_{\text{Min.}} = 1.18$ is obtained.

Long-term stability of the regenerative amplifier

Stable operation over several hours is an important condition for the regenerative amplifier, as its purpose is to serve as a front end for the high-energy multipass amplifier. The high average pump power close to 1 kW and the high circulating power in the cavity are causing thermal drifts of the optics and therefore of the beam pointing. This will translate to a pointing instability of the output beam and as a consequence a change of the pulse energy. To compensate for the thermally induced drift, an active beam stabilization based on position-sensitive detectors and piezo-controlled mirrors is included, and the pump power is actively controlled as fed-back from a photodiode continuously measuring the pulse energy. As a result, the regenerative amplifier can be operated over tens of hours at the full output energy, with no manual corrections necessary. In Figure 3.9 a long-term measurement over >13 hours is shown. The regenerative amplifier was operated at 240 mJ and is stabilized by both the piezo-controlled mirrors and the pump power modulation, resulting in a very reliable front laser source.

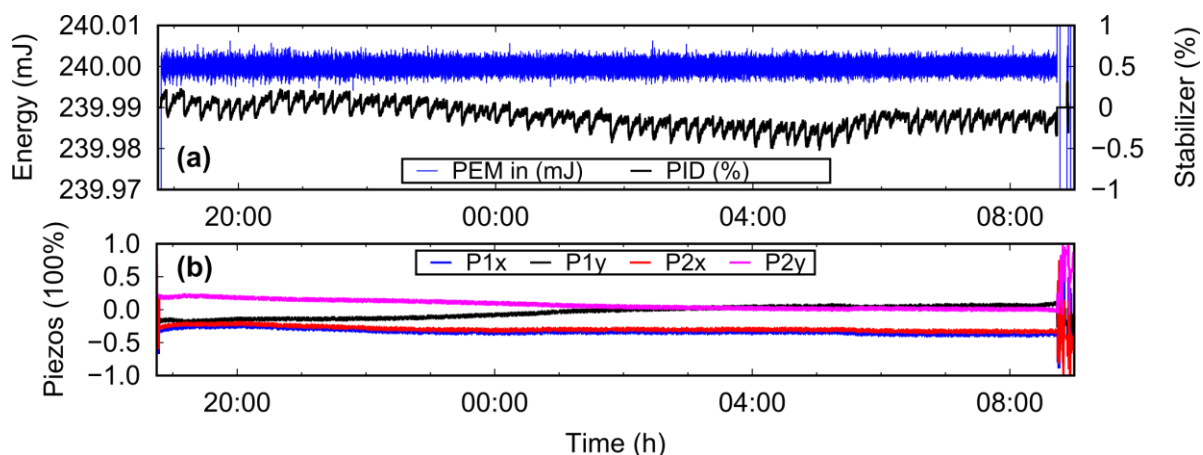


Figure 3.9: Long-term measurement of the regenerative amplifier. (a) Pulse energy (PEM) and pump modulation of the energy stabilizer (PID) in percent of the nominal peak pump power. (b) Actuation of the piezo mirrors of the active beam stabilization stages.

Operation at different Repetition Rates

It is interesting to investigate the energy storage in the active laser medium of the regenerative amplifier at different repetition rates. While the pump energy per seed pulse is maintained constant, the average pump power scales linearly with the repetition rate. Therefore, thermal effects are revealed as well as the influence of the decay time of the upper laser level. For higher repetition rates, the thermal load of the disk increases with the average pump power, translating to a lower optical-to-optical efficiency. To obtain the same output pulse energy, the pump power would have to be increased at a higher repetition rate. On the other hand, the lifetime of the upper laser level of approximately $985 \mu\text{s}$ of Yb:LuAG [112] is on the order of the relevant repetition rates around 1 kHz, so the pump energy for a previous pulse can still contribute to the energy content in the disk during amplification of the next pulse. In Figure 3.10 (a) the measured amplification slopes are shown for repetition rates of 250 Hz, 500 Hz, and 1 kHz. It can be seen that, in the chosen parameter regime (pump energy, duty cycle, efficiency, cavity design, disk geometry), the efficiency of the pulse amplification increases with the repetition rate. The cumulative effect of consecutive pump pulses at higher repetition rate at the same time scale as the excited-state lifetime of the laser-active ions contributes significantly to the overall energy stored in the thin disk.

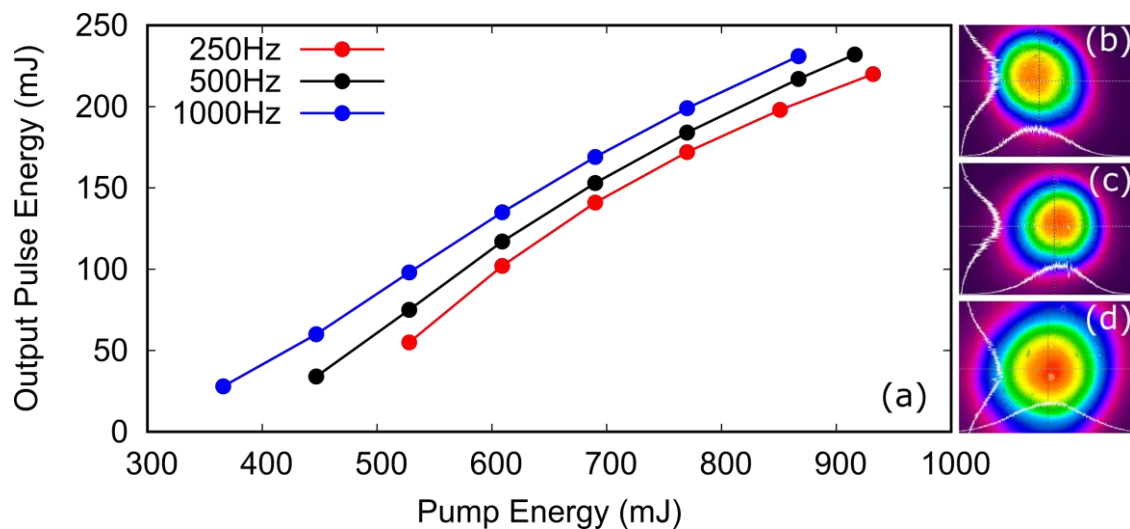


Figure 3.10: Operation of the regenerative amplifier with different repetition rates. (a) Amplification slopes at different repetition rates. (b)-(d) Near-field output beam profiles for the repetition rates 1 kHz (b), 500 Hz (c), 250 Hz (d).

The thermal effect acting detrimental on the efficiency with respect to the repetition rate is still weak at the chosen repetition rates. From the comparison of the amplification slopes it can be seen that at low pump energies the output pulse energies are even further apart compared to high pump energies. This indicates that thermal effects favoring operation at lower repetition rate are becoming relevant in this pump power regime.

Compression of the Regenerative Amplifier Output

The compressor as designed for compression of the Joule-class output pulses was used to compress the output pulses from the regenerative amplifier. In principle the compressor configuration does not differ for the compression of different pulse energies. However, nonlinear effects occurring in the gain medium and other transmissive optics can slightly alter the spectrum and the spectral phase. This will be discussed in more detail in section 6. The measurements of the pulse compression are shown in Figure 3.11.

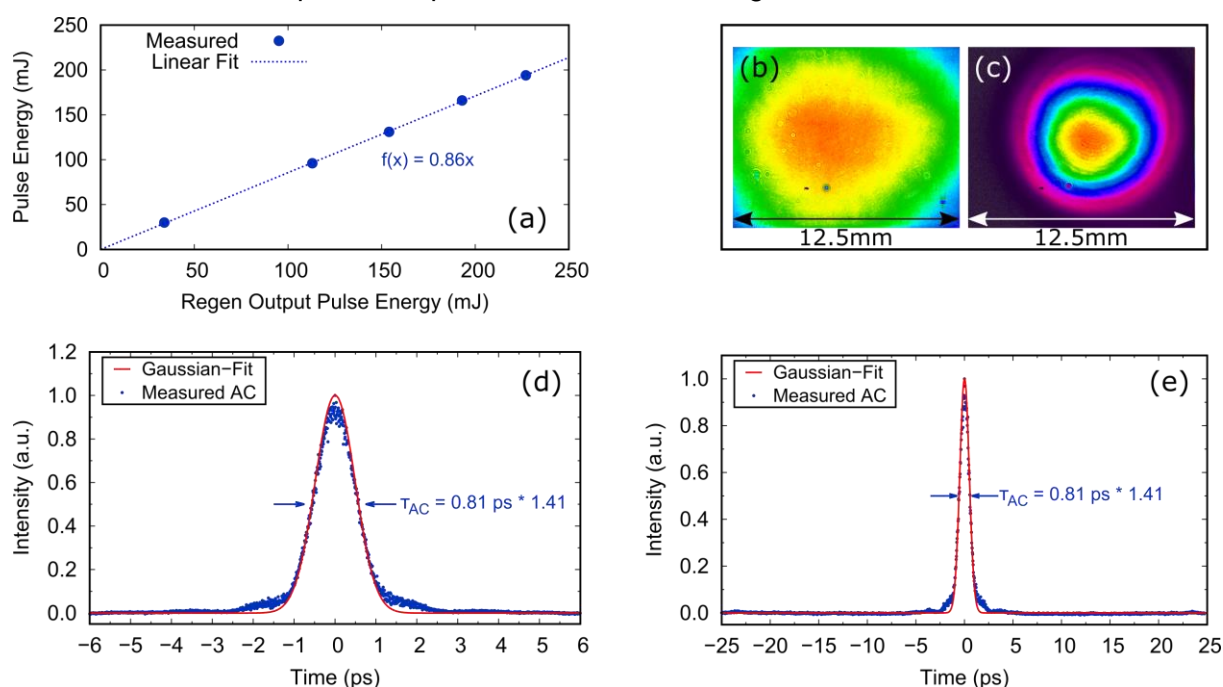


Figure 3.11 Compression of the regenerative amplifier output. (a) Measured compressed output power as a function of uncompressed output power. The slope of the linear fit yields a compressor efficiency of 86 %. (b-c) Beam profile of the raw compressed output, original sized (b) and de-magnified (c) using a Galilean telescope for visualization with the CCD camera (chip size 12.5 mm x 10 mm). (d) Autocorrelation trace of the compressed pulses with narrow scanning window. (e) Autocorrelation trace of the compressed pulses with large scanning window. Both traces are fitted with a Gaussian curve to extract the pulse duration of 810 fs.

The compressor efficiency at this configuration was determined to be around 86 %. The beam profile after compression showed some faint horizontal striations, which is caused by the compressor gratings. The overall shape of the spatial profile, however, is not notably altered. A pulse duration of 810 fs could be achieved with at 195 mJ compressed pulse energy. The side-wings visible in the autocorrelation occur from the alignment of the compressor optimized for the high-energy output pulses from the multipass amplifier instead of the regenerative amplifier. The large-scan-range autocorrelation does not indicate any pre- or post-pulses.

4 Study of energy storage and ASE in different thin-disk geometries

The amplifier system presented in this thesis is aimed at providing highest pulse energies. This is achieved with an high-energy main amplifier realized as a thin-disk multipass amplifier. One of its crucial main component is the thin-disk used as the gain medium in the laser heads. Its properties such as the geometry, shape, and doping concentration can have a major influence on the amount of energy that can be stored in the disk, and hence the single-pass gain for the laser signal. In this chapter, three different thin-disks are characterized with regard to their applicability for the multipass amplifier. The results provide an understanding for the further layout of the amplifier at the targeted repetition rate.

4.1 Measurement setup and approach

In this section the experimental setup and the methods of the study on amplification are described. The experimental results ultimately provide information on the gain and energy storage of different thin-disk geometries, and allow for selecting the appropriate disk for certain laser operation parameters.

When propagating through the active medium, an optical signal is amplified by a certain total gain factor. For a medium with the length L and the dopant ion density N , the gain is given by

$$G = e^{g_0 \cdot L} = e^{\sigma_g \cdot N \cdot L}, \quad 4.1$$

Here, σ_g is the gain cross section, given by

$$\sigma_g = \beta \cdot (\sigma_{em} - \sigma_{abs}) - \sigma_{abs}, \quad 4.2$$

With the absorption and emission cross sections σ_{em} and σ_{abs} , and the fraction of inverted dopant ions β [107].

The gain per single pass through the active medium can be directly measured experimentally. If the material parameters and the absorption and emission cross sections are known, the fraction of inverted dopant ions can be calculated by solving equation 4.2 for β . By replacing the gain cross section σ_g according to equation 4.1, this yields:

$$\beta = \frac{1}{\sigma_{em} - \sigma_{abs}} \cdot \left(\sigma_{abs} + \frac{\ln G}{N \cdot L} \right) \quad 4.3$$

To calculate the amount of optically accessible stored energy within the inverted gain volume, the energy per photon is considered, and multiplied by the number of excited ions within the volume.

$$\begin{aligned} E_{sto} &= \text{energy per photon} \cdot \text{number of excited ions} \\ &= h \cdot \nu \cdot \beta \cdot N_{doping} \cdot A \cdot L \end{aligned} \quad 4.4$$

Where h is Planck's constant, $\nu = \frac{c}{\lambda}$ is the frequency of the laser-active transition with the speed of light c , and A is the area of the pumped spot on the disk. The stored energy per unit gives the stored fluence J and can be calculated via

$$J_{sto} = \frac{E_{sto}}{A}. \quad 4.5$$

The material parameters for a standard Yb doped thin disk are shown in Table 4.1. The data is taken from references [75] and [113]. As the emission and absorption cross sections are dependent on the temperature, the values for 20 °C, 100 °C, and 140 °C are included.

Table 4.1: Material properties of a standard Yb doped thin disk.

Parameter	Value
Dopant ions density (N_{doping}) at 10 % at.	$1.43 \cdot 10^{27} \text{ m}^{-3}$ [113]
Dopant ions density (N_{doping}) at 7 % at.	$1.00 \cdot 10^{27} \text{ m}^{-3}$ [113]
Absorption cross section ($\sigma_{abs,(1030nm,20^\circ C)}$)	$1.49 \cdot 10^{-25} \text{ m}^2$ [75]
Absorption cross section ($\sigma_{abs,(1030nm,100^\circ C)}$)	$1.81 \cdot 10^{-25} \text{ m}^2$ [75]
Emission cross section ($\sigma_{em,(1030nm,20^\circ C)}$)	$2.79 \cdot 10^{-24} \text{ m}^2$ [75]
Emission cross section ($\sigma_{em,(1030nm,100^\circ C)}$)	$2.00 \cdot 10^{-24} \text{ m}^2$ [75]
Thermal conductivity	$\sim 7 \text{ W} \cdot \text{m}^{-1} \text{K}^{-1}$ [113]

With these considerations, the measurement of the single pass gain of an optical signal propagating through the thin disk under test allows to calculate the inversion in the gain medium, and furthermore the stored energy and stored fluence.

Measurement setup

To determine the single pass gain of the different thin disks, a multipass amplifier with 4 passes was set up. The regenerative amplifier served as a seed source and was operated at different repetition rates but equal pulse energy for the tests. The multipass thin disk was pulsed pumped with varying duty cycles and peak power levels.

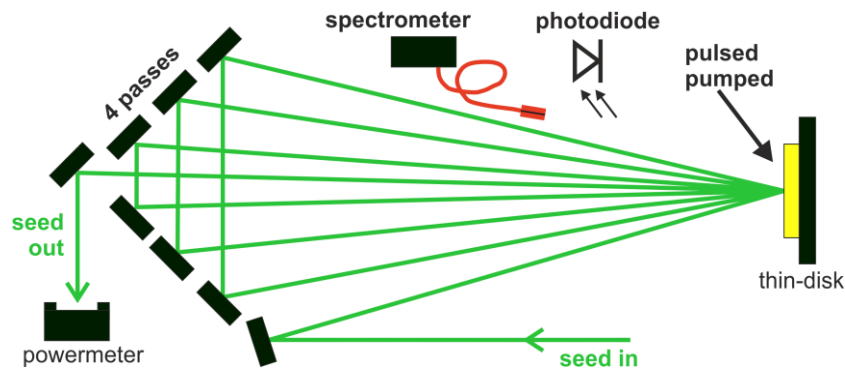


Figure 4.1: Schematic sketch of the experimental setup for the study on energy storage. 4 passes over the disk are aligned via the folding mirrors, amplifying the seed pulses. The output power is measured with a powermeter. The stray light scattered off the disk can be analyzed temporally with a photodiode and spectrally with a fiber-coupled spectrometer.

By measuring the output power, the small signal single pass gain can be calculated:

$$G = \left(\left(\frac{P_{out}}{P_{in}} \right)^{\frac{1}{4}} - 1 \right) \cdot 100\% \quad 4.6$$

4.2 Results for 3 thin-disk geometries and discussion

In this section the experimental results are presented and discussed. In total, three different disk geometries were studied. They are listed in Table 4.2 and will be referred to as Disk#1, Disk#2, and Disk#3 in the following.

Table 4.2: Studied disk geometries.

Disk	Doping concentration	Thickness
Disk#1	10 % at.	125 μm
Disk#2	10 % at.	400 μm
Disk#3	7 % at.	750 μm

With a seed pulse energy of 35 mJ the output power as a function of the pump pulse energy was measured and converted to the single pass gain (SPG) using equation 4.6. The measurements were performed at the shortest possible pump duration, while duty cycles in the range from 15 % to 70 % were used to cover the required pump energy range. See Table 10.1 in appendix A1 for the exact pumping conditions.

The measurement results are shown in Figure 4.2. In the left column of the figure the SPG values calculated according to Equation 4.6 are plotted. The corresponding values for the stored fluence calculated via the equations 4.3-4.5 are shown in the right column of the figure. From the measured data the following conclusions can be drawn.

- The single pass gain values are saturated at a certain pump energy, leading to a plateau for higher pump energies. The saturation may stem from the energy saturation of the disk when approaching the maximum of its energy storing capacity or from a parasitic depletion mechanism initiated when a certain population inversion is attained (see chapter 2.1.1).
- The maximum SPG values increase approximately linearly with the total number of dopant ions $N_{dop}^{(tot.)}$ along the thickness d_{disk} of the disks, i.e. $N_{dop}^{(tot.)} = N_{doping} \cdot d_{disk}$
- For each disk the maximum SPG values decrease when increasing the repetition rate, i.e. at higher average pump power. This can be attributed to a higher temperature of the active medium, resulting in reduced emission cross sections [75].

- The relative decrease of the SPG as a function of the repetition rate tends to be higher for thicker disks. At a pump energy of 2.53 Joule, the measured data gives a reduction of the SPG by 26 % for Disk#1, 26 % for Disk#2, and 43 % for Disk#3.

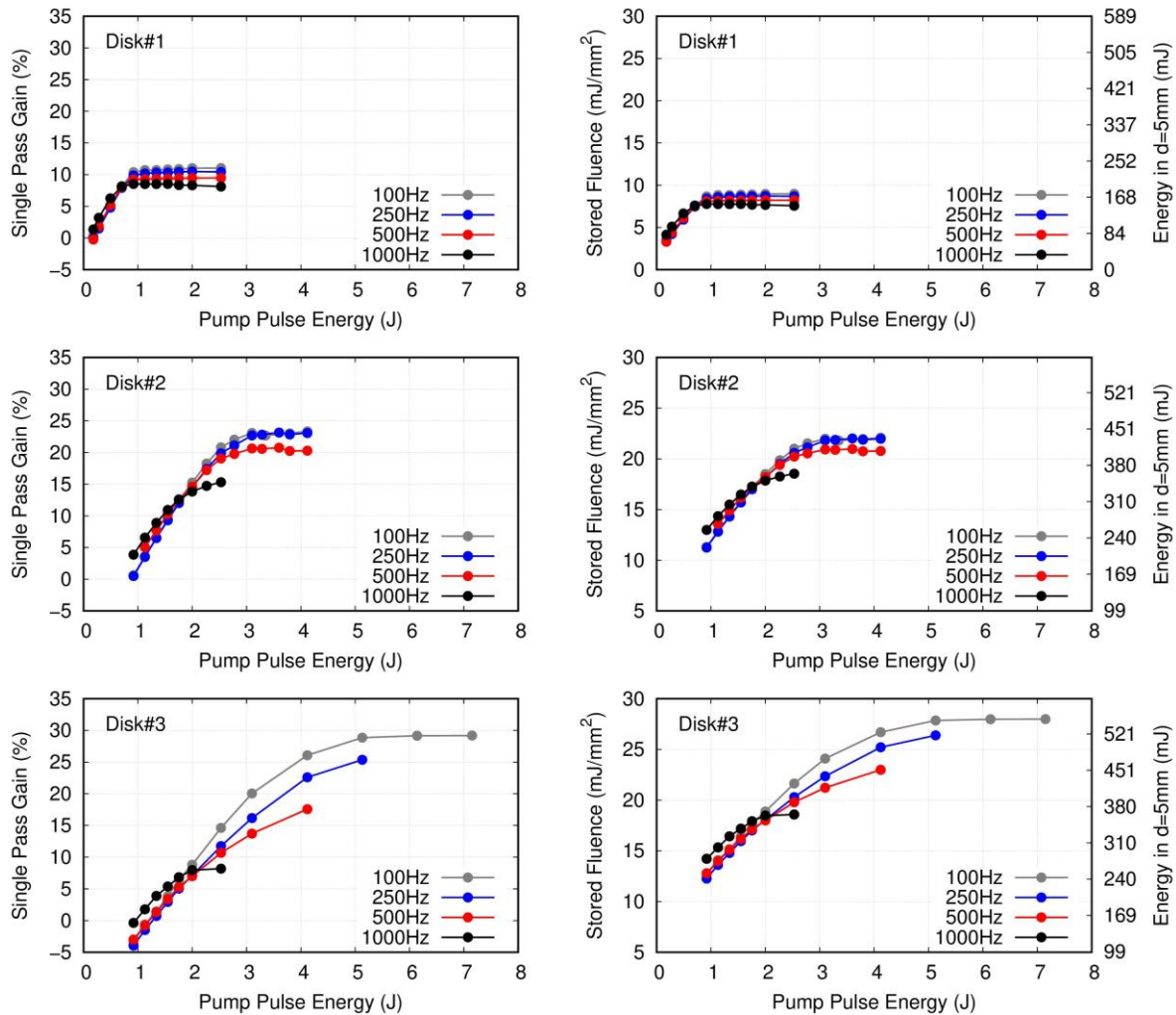


Figure 4.2: Measured single pass gain (left-hand side) and corresponding stored fluence (right-hand side) at different pump pulse energies for three disk geometries. The measurements were performed at different repetition rates between 100 Hz and 1000 Hz.

For the choice of a suitable thin disk geometry, therefore the desired repetition rate must be taken into account, in order to achieve a maximum stored energy and hence a maximum SPG. A convenient way to compare the performances of the different thin disk geometries is to plot the maximum SPG values obtained in the measurements as a function of the repetition rate, see Figure 4.3 (a). As expected, the SPG decreases with the repetition rate as the thermal load is scaled. At a low repetition rates, disk#3 would be favored for a laser application, as it provides the maximum SPG of almost 30 %, followed by disk#2 (23 %) and disk#1 (11%). At a repetition rate of 350 Hz there is a cross-over between disk#3 and disk#2, which renders

disk#2 favorable for any laser application operating at the corresponding average pump power level.

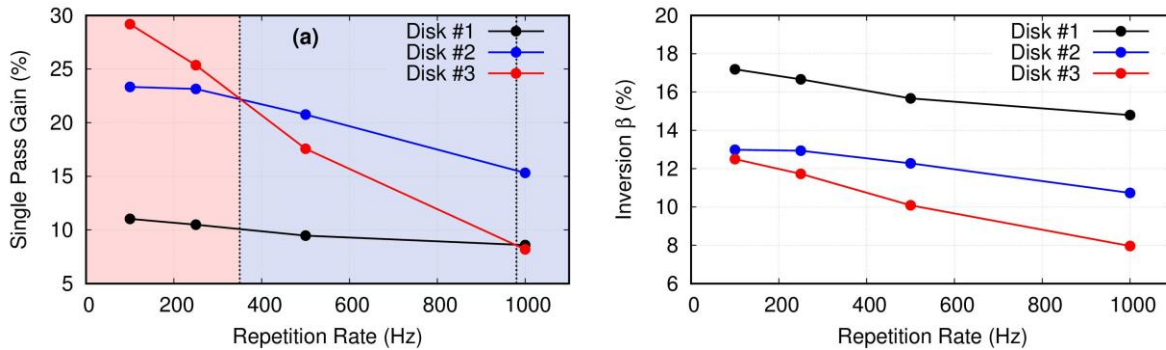


Figure 4.3: Maximum single-pass gain and inversion ((a) and (b).) as a function of the repetition rate. The thermal influence is responsible for the degradation of the gain. At low repetition rates Disk#3 provides the highest gain values (shaded in red). Above a repetition rate of 350 Hz, Disk#2 outperforms Disk#3 in terms of single pass gain. Disk#1 outperforms Disk#3 at a repetition rate of 1 kHz, but Disk#2 still provides the highest single pass gain.

When extrapolating for repetition rates beyond 1 kHz, another cross-over can be expected around 2 kHz between disk#1 and disk#2, making disk#1 the candidate for operation at this point.

Interestingly, when calculating the inversion β from the SPG values (see equation 4.3), it can be seen that the highest inversion is attained in disk#1 (i.e. the thinnest disk), followed by disk#2 and then disk#3. This can be attributed to the total intensity attained in the pumped spot on the disk, where a total of 22 pump light passes are cumulated by the multipass pump head configuration. The smaller single-pass pump light absorption for thinner laser disks¹ leads to more pump light reflections, resulting in a higher cumulated intensity, which allows for a higher achievable steady-state inversion in the disk, as discussed in chapter 2.1.1 (see Figure 2.5). An extensive discussion on modelling the pumping process can be found in [107].

Temporal and spectral analysis of the pumping process

A possible reason for the low value of the inverted fraction is the parasitic depletion of parts of the stored energy already during the pumping process. Amplified spontaneous emission (ASE) has been identified in the past to be a crucial parasitic process limiting the stored energy and the gain in thin disk laser systems [77,78]. To analyze the influence of ASE, the pumping

¹ at constant doping concentration

process was investigated in more detail with temporal and spectral measurements. With a photodiode, the temporal signal of pump light and scattered and stray light was measured, while the spectra of the emitted light could be measured using a fiber-coupled grating spectrometer (see Figure 4.1). The experimental results from the temporal and spectral analysis of the pump process are shown in Figure 4.4. The temporal measurements were performed for all of the three thin disks, while the spectral measurement was only performed for disk#1. All measurements were performed at a repetition rate of 100 Hz to reduce thermal effects. The experimental results are shown in Figure 4.4. The signal recorded by the photodiode and the spectrometer was not spectrally filtered, therefore the fluorescent emission of the laser disk is visible as well as stray pump light. The measurements were performed at different pump energies, achieved by modifying the duty cycle and hence the duration of the pump pulses. While at low pump energies the photodiode signal (panels (a), (c) and (d)) increases approximately linearly with the pump duration, an steeper increase of the signal occurs at a pump energy of 2.0 J for disk#1, 3.1 J for disk#2, and 6.14 J for disk#3.

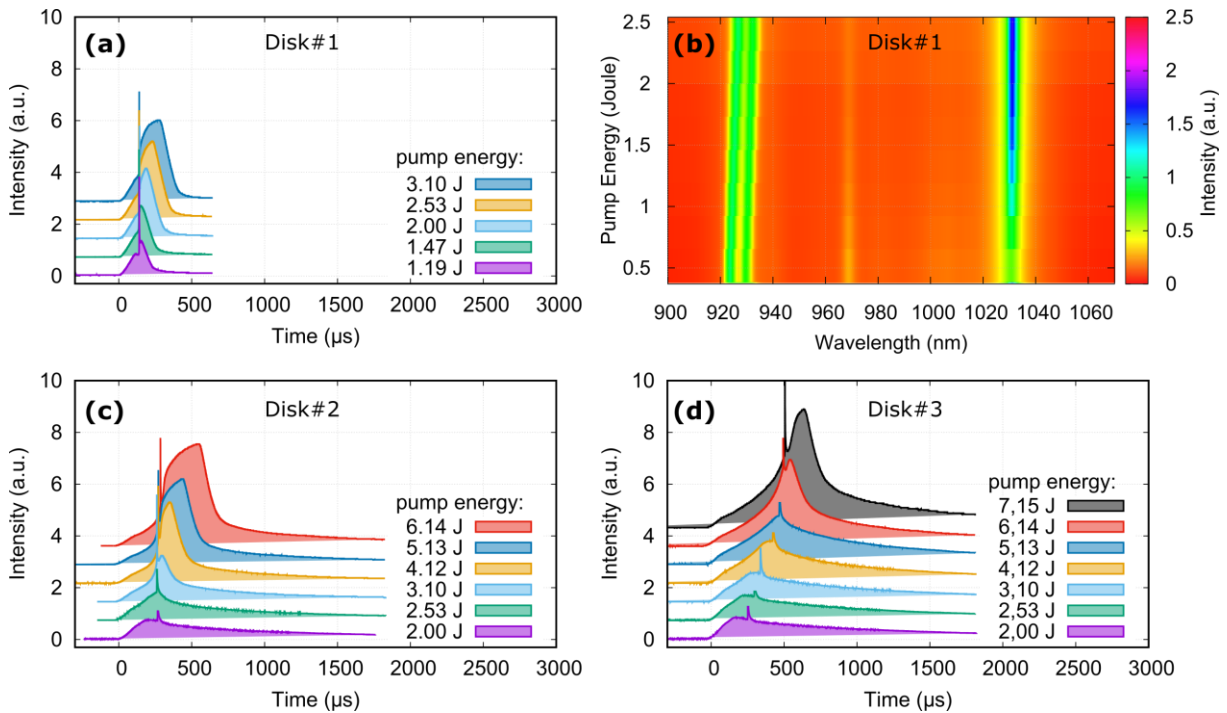


Figure 4.4: Photodiode (PD) signals and spectra measured during the experiments. In all measurements the stray light emitted from the disk in forward direction is recorded. (a) PD signal for Disk#1. (b) Emission spectra measured for Disk#1 without any seed. (c) PD signal for Disk #2. (d) PD signal for Disk#3.

The sharp peaks visible in the photodiode traces corresponds to the position of the seed pulse, and the pump-seed delay was optimized for the maximum output power before recording the data. The sudden increase of the photodiode signal after the position of the seed pulse indicates the initiation of an enhanced emission process in addition to the energy extraction by the seed pulse. Amplified spontaneous emission (ASE) can be such a parasitic process, that is initiated when a certain gain is achieved inside the gain medium. It is known from thin-disk lasers, that the multiple partial reflection at the edge of the thin disk, as well as the total internal reflection at the thin disk faces can lead to a strong ASE effect limiting the energy storage and hence, the gain [77–79]. The increase of signal visible in the photodiode traces after the optimum pump-seed delay may therefore originate from ASE losses building up in the thin disk, and being both partially scattered and reflected. A spectral measurement of the scattered light was performed for disk#1, as shown in Figure 4.4 (b). For each pump energy set point a spectrum was recorded, and the data was normalized to the double-peaks at a wavelength of 930 nm. From the data it is visible that the emission peak of the laser wavelength at 1030 nm is increased for higher pump energies. In conjunction with the temporal photodiode traces (panel (a)), this enhanced emission at 1030 nm provides a further indication of ASE being evoked above a certain pump energy.

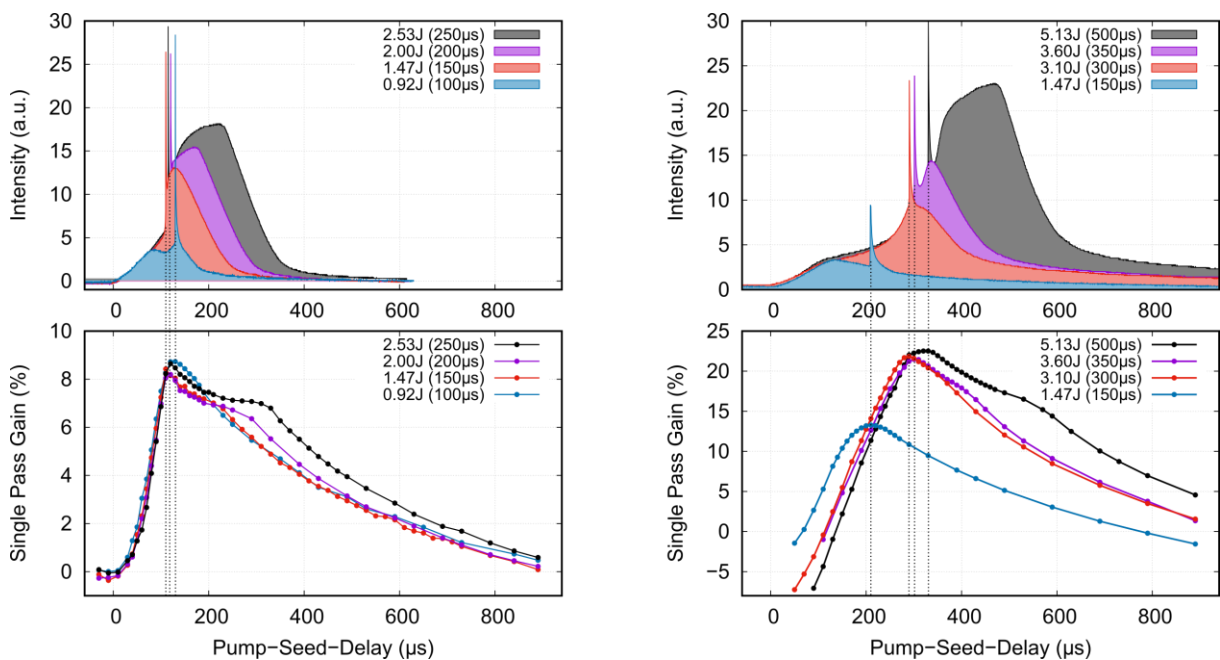


Figure 4.5: Instantaneous gain probed over the duration of the pump pulse at 100 Hz. The graphs on the top are the photodiode traces corresponding to the pump energy set points. The graphs on the bottom show the instantaneous gain measured with the setup shown in Figure 4.1. For the measurements, disk#1 (left) and disk#2 (right) were used.

Probing of the instantaneous gain

In continuation of the results indicating ASE within the pumping process, a further experiment was performed to temporally probe the instantaneous gain during a pumping cycle. The same measurement setup from Figure 4.1 was used. To obtain the instantaneous gain at a certain time delay after the beginning of the pump pulse, the delay of the seed pulse relative to the pump pulse was scanned across approximately the lifetime of the gain material, i.e. $985 \mu\text{s}$ [112]. Simultaneously, the photodiode traces were recorded, analogous to Figure 4.4. The experimental results are shown in Figure 4.5 for disk#1 and disk#2. For visualization, the photodiode traces corresponding to the delays with maximum single pass gain are plotted on the same horizontal axis as the measured gain. Therefore, the positions of the seed pulses (=sharp peaks) in the photodiode traces coincide with the delay for the maximum gain. As energy is deposited and stored in the laser disks after the beginning of the pump pulse, the gain increases as expected. For a small pump energy (i.e. a short pump pulse duration) the gain then decays exponentially over time, as expected due to the finite lifetime of the excited laser ions. When increasing the pump energy, however, a shoulder starts to emerge after the maximum of the gain. The pump energy where this shoulder emerges is different for the two disk geometries, amounting to 1.47 J for disk#1 and 3.1 J for disk#2. Interestingly, the sudden increase of the photodiode signal coincides with the emergence of the shoulder in the gain trace. In simulations, similar data has been obtained when modelling ASE in thin-disk lasers [78], showing that a further deposition of energy in the gain medium is prevented by ASE when the gain attains a certain value.

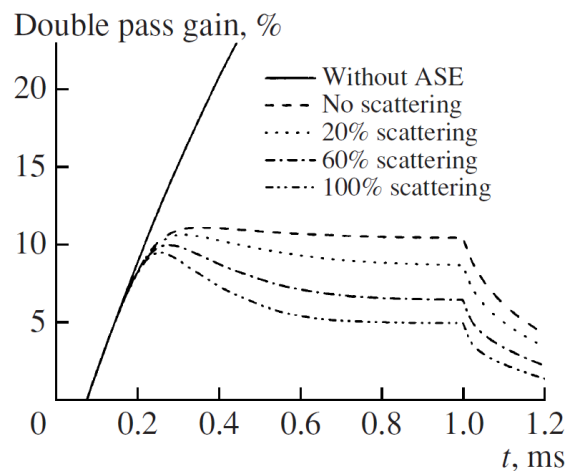


Figure 4.6: Simulation of the gain build-up as a function of time during a quasi-cw pulsed pumping cycle. When including ASE with a feedback mechanism based on scattering at the disk edge, a shoulder and a plateau emerges for long pump durations. Simulation parameters are: disk diameter 25 mm, disk thickness $150 \mu\text{m}$, pump spot diameter 11.6 mm, pump power 4 kW, pump duration 1 ms. Figure taken from [78].

A simulation of the gain in a similar Yb:LuAG thin-disk geometry is shown in Figure 4.6. The build-up of the gain during pumping is shown with different rates of backscattering at the edge of the thin-disk. It can be seen that the occurrence of the shoulder in the instantaneous gain is associated with the backscattering rate of ASE photons at the edge of the thin-disk. The rollover is attributed to repeated partial reflections of the transversely propagating parasitic radiation. For long pump durations, a stationary plateau is eventually formed representing the steady state of the dynamic balance between pumping and parasitic ASE. As a result, in order to optimize an amplifier using this thin-disk configuration, the pump-seed delay must be adjusted to the time when maximum gain is reached, i.e. at the beginning of the shoulder. For longer pump durations the gain will roll over and the amplifier be less efficient, as can be seen from the photodiode traces in Figure 4.4. Moreover, extra thermal load is induced by pump durations beyond the gain rollover point, which should be avoided.

In conclusion, the experimental results provide information for the optimum operation point for a certain thin-disk geometry and peak pump power. Depending on the repetition rate, different disk geometries have to be selected to achieve an optimum result. A maximum favorable pump pulse energy can be deduced from the measurement for the three disks, where maximum gain is attained. Pumping beyond this energy will not result in a higher gain or stored energy, but rather deteriorate the thermal behavior of the laser system.

The following **conclusions** can be drawn for the multipass amplifier developed in the framework of this thesis:

- Disk#2 is favorable among the tested geometries in the regime around 1 kHz repetition rate, as the provided gain outperforms disk#1 and disk#3 (see Figure 4.3)
- The pump energy should be limited to <3.1 J to maximize the gain while minimizing the thermal load in the thin disk. This was found by probing the instantaneous gain via scanning the pump-seed delay, where a shoulder in the gain trace indicates the prevention of further inversion build-up by ASE, in agreement with simulations [78].
- The pump energy should therefore be limited to <3.1 J to approach close to the maximum gain while minimizing the thermal load in the disk. Pumping beyond this energy will not result in higher gain or stored energy, but rather deteriorate the thermal behavior of the laser systems
- The pump power is further restricted by heat-induced damage issues, which may constitute the major limitation at high repetition rates. See chapter 5 for more details.

5 Thin-disk Multipass Amplifier

In this chapter the development of the main amplifier is summarized. Three experimental concepts were tested, in which the number of laser heads was increased from one, to two, to four. Based on the concept using four laser heads, the final design of the multipass amplifier was conceived and implemented. In addition to experiments addressing energy extraction, strategies for spatial mode conservation and optimization were analyzed. The results were applied in the amplification experiments and in the final multipass amplifier. Additionally, the key laser components used for the multipass amplifier are presented and characterized in this chapter. Furthermore, fundamental criteria for the design and layout of the Joule-class multipass amplifier are described, concerning the energy storage in the laser disks, beam guiding concepts in the amplifier.

5.1 Design Considerations

Energy storage in the laser disk

In pulsed laser amplifiers, the energy is stored in the laser medium before it is extracted by the seed pulses. The energy extraction typically occurs on a time scale of nano- to microseconds, corresponding to a seed propagation distance up to hundreds of meters inside the amplifier. For the case of diode pumped solid state lasers (DPSSL), the energy is delivered by laser diodes. By combining many diode emitters, an optical output power in the range of $P_{\text{pump}} = 10 \text{ kW}$ is routinely achieved. For the given example, a pump time $T_{\text{pump}} = \frac{E_{\text{pump}}}{P_{\text{pump}}} = 250 \text{ }\mu\text{s}$ is required to accumulate an energy of $E_{\text{pump}} = 2.5 \text{ J}$. As a consequence for the laser medium, the upper-state lifetime must be on the order of, or above the required pump time ($\approx 965 \text{ }\mu\text{s}$, for Yb:LuAG [113]) and the geometry and doping concentration of the laser medium must be designed such as to be able to store the required amount of energy.

From the measurements presented in chapter 4.2, the most suitable disk geometry was found to be Disk #2. At a repetition rate of 1 kHz, the stored fluence reached 18.5 mJ/mm^2 at a total pump energy of 2.5 J (see Figure 4.2). Under consideration of the overlap efficiency $\eta_0 \approx 40\%$ of a TEM₀₀ laser beam with a circular flat-top pump profile [114,115], the minimum stored energy necessary to provide an extractable energy of 1 Joule amounts to 2.5 J, corresponding to a pumped spot diameter $D_{2.5\text{J}} = 13.2 \text{ mm}$ in the case of Disk #2. In practice, however, a lower energy extraction efficiency can be expected due to losses and a finite number of roundtrips. Therefore, either larger pumped areas on the thin-disks or multiple, serially combined thin-disks are expected to be required for an amplifier providing an energy of 1 Joule.

Thin disk laser heads

The thin-disk laser heads chosen for the multipass amplifier can host a thin-disk with a diameter up to 20 mm. Each thin-disk can be pumped with 12 kW optical power in CW operation. In the pulsed operation, the average power is reduced with the duty cycle. Further experimental characterization of the pump modules is detailed in section A1.

The typical pump spot diameter on the thin-disk is ~12 mm, which is determined by the optical setup of the pump unit, allowing for a certain focal spot size on the laser disk (beam quality of the laser diodes, focal lengths of the imaging optics, magnification). For the thin-disk #2 (see chapter 4.2), the energy that can potentially be stored within this spot is 1.92 J. Note that a significantly higher amount of pump energy is required to achieve this stored energy.

High pump light absorption is obtained with a multipass arrangement for the pump beam. A total of 44 passes through the laser disk are realized by a parabolic mirror in combination with several prism pairs displacing the beam spatially. Due to the overlapping areas of each pump pass, the effective pump intensity on the disk is a multiple of the intensity of the pump beam. This enables to achieve a high inversion, as described in section 2.1.1 by equation 2.3 and Figure 2.5.

Beam guiding

The paramount benefit of the uni-axial heat flow provided by the thin disk laser geometry at the cost of a small longitudinal extension of the gain medium typically leads to low single-pass gain factors [42]. Therefore, the seed pulses must pass the thin-disk multiple times to achieve a high energy extraction. While in regenerative amplifiers the seed multiplexing takes place temporally within a resonator, in multipass amplifier configurations the beam is folded geometrically over the disk. Among the most important advantages of multipass amplifiers are:

- The feasibility for amplification of arbitrary temporal signal waveforms, independent of pulse duration, repetition rate, or timing jitter.
- The linear layout of the amplifier, eliminating the need for an electro-optic switch, thereby enabling large beam diameters and hence high pulse energy, that can be scaled via the apertures of thin-disk and folding mirrors.

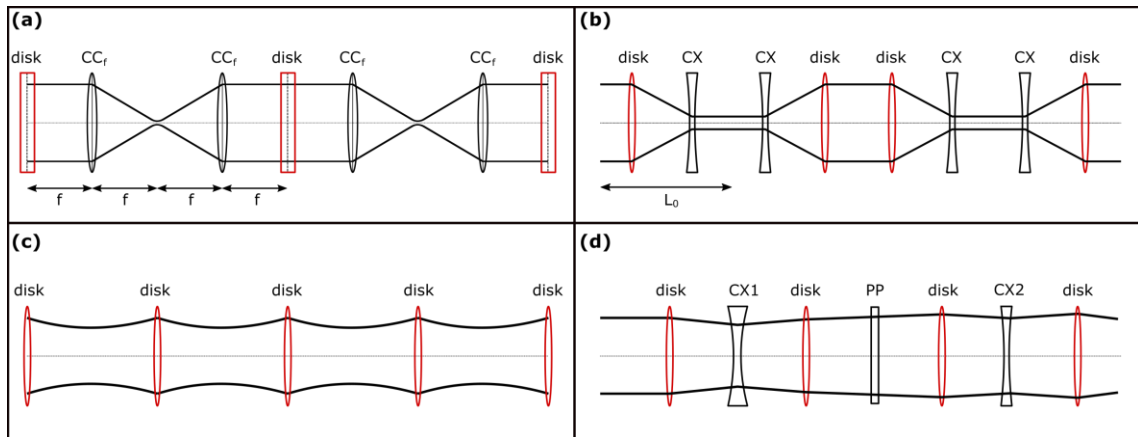


Figure 5.1: Schematic visualization of different concepts to achieve stable propagation. See the text for details.

On the other hand, the beam routing through the multipass amplifier can be challenging, as long propagation distances are realized, and small perturbations of the beam size and divergence can be amplified during propagation. Particularly for high-energy and high-power lasers, where the beam diameter must be maintained above a certain diameter to respect the damage threshold of the optics, several propagation schemes have been proposed:

1) Relay Imaging [56,116,117]

The 4- f configuration can be used to relay-image the beam at the plane of the thin-disk from pass to pass as shown in Figure 5.1 (a). As a result the beam diameter at the thin-disk is constant and independent on its spherical curvature. This allows for operation at different thermal lensing. The foci between the imaging lenses or mirrors lead to high intensities and eventually ionization of the air in the case of high peak powers. Therefore, such multipass configurations must be realized in vacuum. Another drawback is that wavefront distortions of the beam invoked by the disk surface accumulate for each pass, as the beam position and size is the same due to the imaging process.

2) Resonator-Like Propagation [79,118,119]

By unwinding the roundtrips of a stable optical resonator, stable propagation can be realized in a linear multipass setup. The beam path then follows a concatenation of stable resonator segments with length L_0 , see Figure 5.1 (b). As a result, good beam quality is achieved as higher-order modes are suppressed by higher losses. Depending on the particular layout, however, long propagation distances either as free propagation

or as effective propagation using telescope mirrors are required. Since for high-energy pulses the beam diameter must be maintained sufficiently large, a resonator-like propagation will lead to long propagation distances in this case.

3) Lens Guiding [44,120,121]

Stable propagation can be achieved via a balance between periodic focusing and the beam divergence due to diffraction. By employing a concave curved disk, the focusing takes place at each disk pass. This layout can be designed such, that the wavefront curvature matches the disk curvature for each pass, leading to a quasi-collimated propagation with stable beam diameter, see Figure 5.1 (c). For the design, the free parameters are the disk radius of curvature (ROC), the beam propagation distance between two disk passes, the seed beam diameter, and the beam quality of the seed beam. For the case of high beam quality and large beam diameters, the divergence is low. This leads to large disk ROCs and long propagation distances between two disk passes. Moreover, the beam diameter excursions in case of imperfect layout parameters are large, eventually limiting the feasibility of the concept due to laser induced damage on the optics when the beam becomes too small. An additional technological uncertainty is given by the initial disk ROC as it is slightly dependent on the manufacturing batch. A further constraint is given by the variable thermal lens, depending on the pump power. For thin-disk lasers featuring a thermal lens, this approach works only for a certain point of operation.

4) Quasi-Collimated Propagation [122,123]

A modification of approach No. 3) can be realized by employing additional curved mirrors suitable to correct the beam divergence and hence the beam diameter in case the beam diameter undergoes large excursions after different passes. The curved mirrors can be placed as transfer mirrors between two disk passes. As a result, the seed beam can propagate quasi-collimated in the multipass amplifier provided the thermal lens of the thin-disk is constant, see Figure 5.1 (d). Therefore, this approach works only for a certain point of operation at a specific pump power. On the other hand, the beam propagation can be modified and adjusted during the experiment, and high pulse energies can be achieved at a specific point of operation. At the same time, propagation distances are kept short, allowing for stable operation due to minimized pointing instability. For the multipass amplifier realized in the framework of this thesis, the quasi-collimated propagation approach was chosen.

5.2 Preparatory Experiments

5.2.1 Characterization of the pump power

The performance of the available pump modules was tested by measuring the average power using a thermal powermeter and a photodiode detecting the stray pump light. The diodes were driven in cw operation and pulsed mode at different duty cycles to characterize the dynamics. Spectra of the pump light at the different operation points were recorded using a grating spectrometer (Ocean optics HR4000). In Figure 5.2 the measurement results are shown. The output power shows a linear dependence from the diode current for the different duty cycles. In CW mode, the measurement was stopped at 12 kW output power as limited by the powermeter capability. The slopes measured at different duty cycles exhibit a linear behavior of the pump power with respect to both the pump current and to the pump duration, as can be seen from the slopes of the linear fit curves.

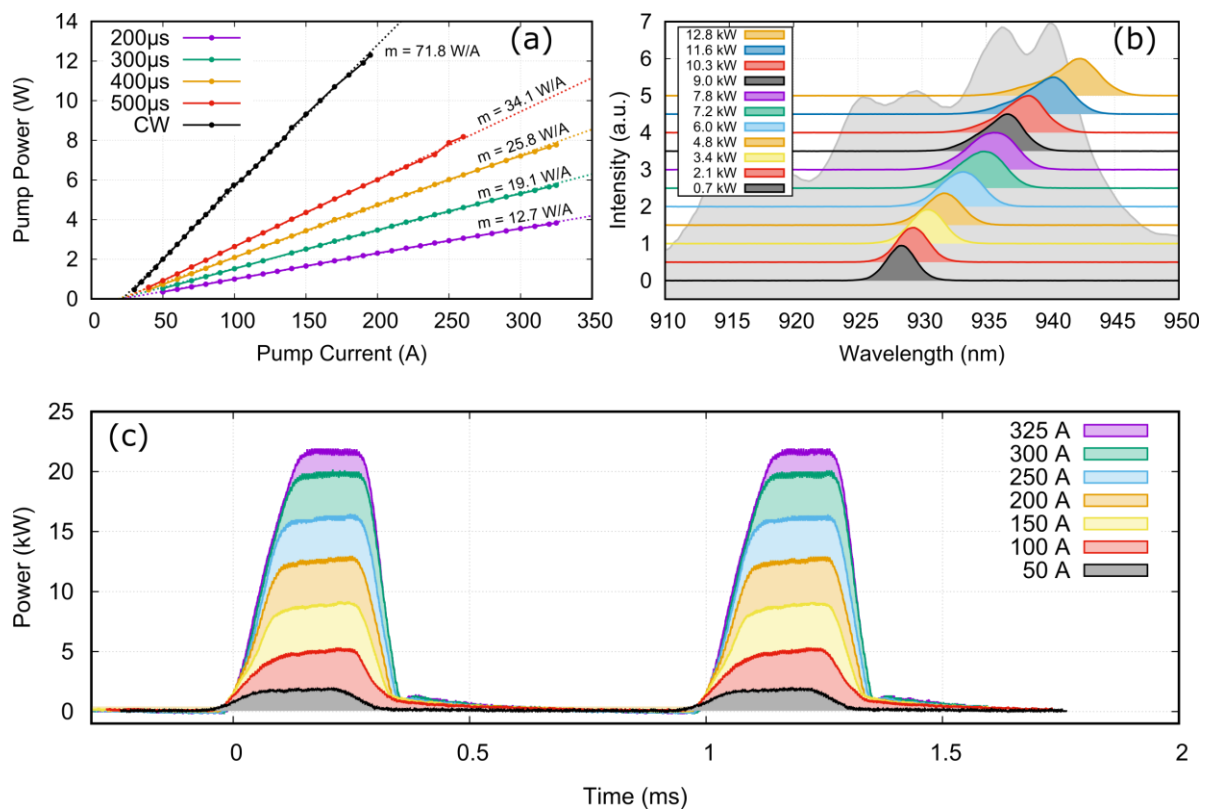


Figure 5.2: Characterization of the pump unit comprising 6 pump laser diode modules. (a) Average pump power as a function of the diode current for different duty cycles at 1 kHz. (b) Spectra of the pump light measured for different average pump powers. A central wavelength of 940 nm is reached at 12 kW average pump power. The absorption cross section of Yb:LuAG is overlaid for clarity. (c) Instantaneous pump power measured with a calibrated photodiode.

The spectrum of the pump light is shifted by approx. 1.1 nm/kW output power, which is due a decreased band gap energy during thermalization of the semiconductor material when operating at high powers. However, the broad absorption feature of Yb:LuAG around 940 nm also provides a sufficiently high absorption cross section in the range between 920 nm and 940 nm, as shown in Figure 5.2 (b). In combination with a total of 44 passes of the pump light through the thin disk a very high pump light absorption is expected [124].

5.2.2 Thermal load reduction by pulsed pumping

As mentioned in chapter 3.2, the thermal load on the disk can be reduced by pumping with reduced duty cycle at the laser repetition rate. A reduced thermal load leads to weaker wavefront distortions of a beam reflected at the laser disk, and to a reduced change of the dioptric power of the disk.

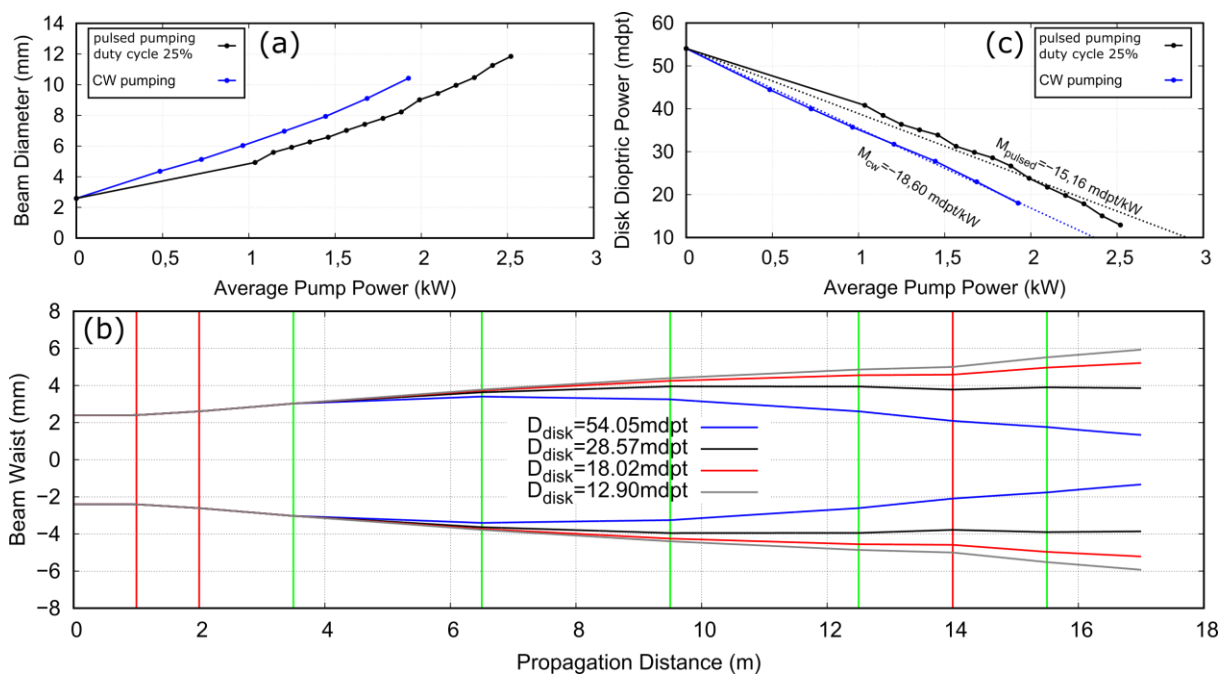


Figure 5.3: Experiment to determine the dioptric power of the thin-disk as a function of the pump power for CW and pulsed pumping. (a) Measured beam diameter after 5 disk passes as a function of the average pump power. (b) Modeled beam diameter evolution during the 5-pass beam propagation. The green lines mark the position of the thin-disk. The red lines mark the position of curved mirrors used to control the beam quasi-collimation. In the model, the dioptric power of the thin disk was adjusted such that the output beam diameter matched with the measured beam diameter at different pump powers. (c) Resulting dioptric powers of the thin disk from the model plotted as a function of the pump power.

To characterize the reduction of the thermal load, the dioptric power of the laser disk was measured as a function of the average pump power in CW and pulsed operation. In an experimental setup, the laser beam was guided five times over the disk, and the output beam diameter was measured using a beam profiler camera. The experiment is summarized in Figure 5.3.

In the experiment, the pump power was increased up to 2.5 kW for the case of pulsed pumping, and 2.0 kW for the CW case. When using pulsed pumping with a duty cycle of 25 %, the dioptric power change is reduced from -18.6 mdpt/kW to -15.16 mdpt/kW. This reflects also the reduction of wavefront distortions associated with the thermal load of the disk, which is advantageous in addition to the reduced thermal lensing when increasing the pump power. For these reasons, a reduced pump duty cycle was employed for the multipass amplifier.

Note that a maximum average pump power of 2.5 kW was defined as an upper limit throughout all experiments carried out in this thesis. This value is based on experience with thin-disk lasers using similar parameters of the laser head [125].

5.2.3 Influence of the pump spot on the propagation

General considerations

The characteristics of the pump spot or the pump volume have an important influence on the behavior and the performance of a laser. The spatial distribution of the pump intensity often causes an inhomogeneous transverse distribution of the gain coefficient. For the laser signal, the inhomogeneous gain can cause phase distortions, which are often undesired since the beam profile and the beam quality of near-fundamental mode laser beams can be altered. In laser resonators, the degradation of beam quality and transverse beam profile formally corresponds to a (resonant) coupling of the fundamental mode to higher order modes, whereby power is transferred to the higher-order modes and the beam quality suffers [126]. Common techniques to mitigate such unwanted effects are manifold. First, these concern the layout of optical resonators such that parasitic higher-order modes are non-resonant with the desired fundamental mode, i.e. a relative Gouy phase shift between the fundamental and the higher order mode does not amount to a multiple of 2π for one resonator round trip. Second, the excitation of higher order modes can be avoided by selectively introducing losses to the parasitic mode by means of apertures clipping away some of the power carried in the higher order modes. In this context, the pump spot can function as a soft aperture for the laser signal beam by favoring the fundamental mode by providing higher gain as compared to beam profile components belonging to higher-order modes. In other words, it is evident that the profile of

the pump spot can have an influence on the propagation of the signal laser beam and therefore on the beam quality at the output.

In the present multipass amplifier, the beam is propagating quasi-collimated and no resonator is present in which resonant power transfer to higher order modes could occur. However, non-resonant power transfer can still introduce significant beam profile distortion, which degrades the beam quality. To test the sensitivity of the beam profile on the pump spot, different pump spot diameters and shapes were tested for their influence on the beam quality.

Pump light transport

The pump spot is generated by imaging the end of the light homogenizer rod onto the disk multiple times using the multipass pump laser head. To collimate the pump light beam exiting the homogenizer, a collimation lens is used. By using collimation lenses with different focal lengths, the diameter of the collimated beam can be adjusted, while at the same time the focal spot size changes inversely proportional according to the magnification factor of the optical system. If the distance between the end of the homogenizer and the collimation lens does not match with the focal length of the collimation lens, the pump beam is not collimated completely and the pump beam remains slightly convergent. When focused by a parabolic mirror designed for a collimated incident beam, the thin disk appears behind the focal plane, which results in a blurred image and therefore a smoother pump profile with shallower edges. In Figure 5.4 a schematic sketch of the pump beam transport is shown for the case of a correctly aligned collimation lens at a distance f_{Coll} from the homogenizer and at a displacement of d_z . In the pump head multi-pass configuration, a total of 44 disk reflections are achieved by displacing the beam between the disk passes. In Figure 5.5 the pump spots using collimation lenses with different focal lengths are shown both for the correct alignment (disk in focus) and for the misaligned collimation lenses (disk out of focus). The distribution of the intensity is thereby transformed from a flat-top shape to a super-Gaussian with less steep edges.

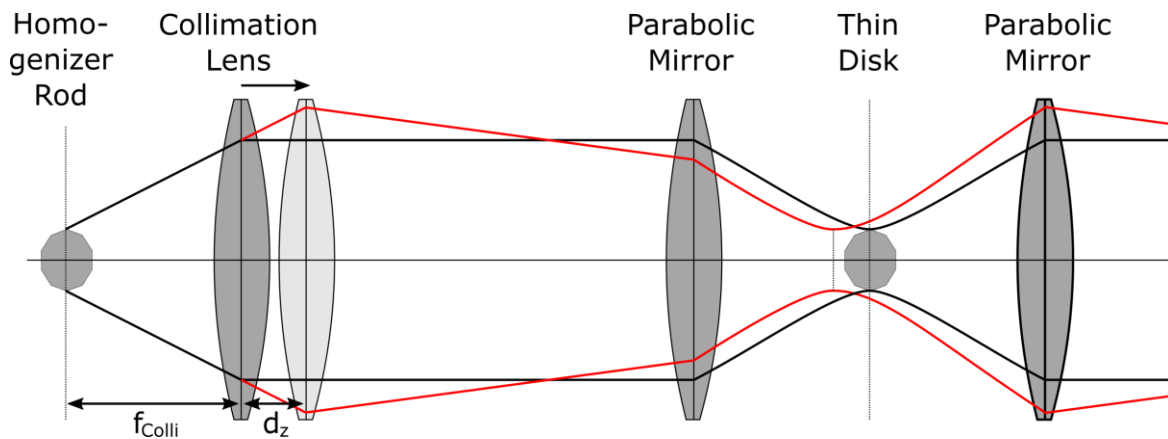


Figure 5.4: Collimation and beam transport of the pump light. from the homogenizer to the disk. The light exiting the homogenizer rod is first collimated by the collimation lens and then focused by the parabolic mirror onto the thin disk. The divergent beam is re-collimated by the parabolic mirror, displaced by a retro-reflecting mirror pair, and focused onto the thin disk again. The red line shows the beam caustic with a misaligned collimation lens.

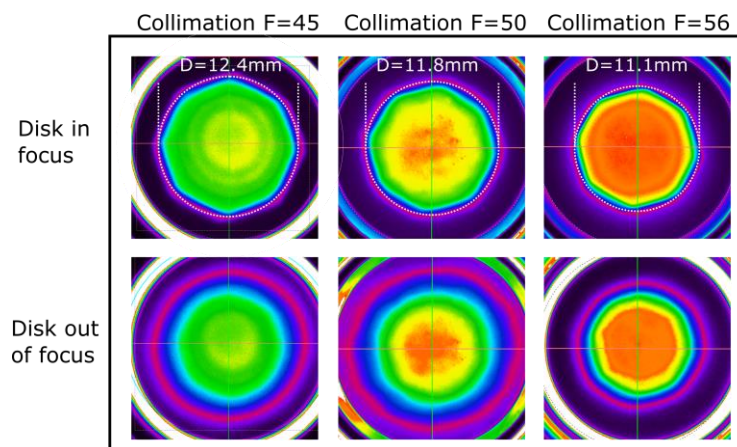


Figure 5.5: Pump spots for different focal lengths of the pump collimation lens.

Experiment on the influence of a de-focused pump spot

The influence of the focus position of the pump spot relative to the plane of the thin disk on the signal beam profile is shown in Figure 5.6. For this experiment, the Gaussian shaped output beam from the regenerative amplifier was directed onto the disk 8 times using folding mirrors. A small signal power of a few Watts was used for the experiment, however, the experimental results are also valid for higher seed power, as the influence of the spatial gain profile apply to smaller signal power equally. The disk was pumped with an average power of 1.75 kW. After

each disk reflection, the instantaneous beam profile was measured using a CCD beam profiler camera with a chip size of 12.5 mm x 10.00 mm (Spiricon LT665). Curved mirrors were implemented between the disk passes to maintain a collimated beam with constant beam diameter. From the measured beam profiles, it can be seen that the octagonal shape of the focused pump spot is slightly imprinted on beam profiles at the wings, altering the profile for each pass. Finally, this leads to an inhomogeneous intensity distribution after 8 passes. The same experiment performed with de-focused pump spot yields a more homogeneous intensity distribution after 8 passes, and also smoother beam profiles throughout the propagation. This is attributed to the enhanced radial symmetry of the de-focused pump spot on the one hand (no octagonal shape), and to the smoother intensity distribution inside the pump spot due to a small displacement for each pump pass on the other hand.

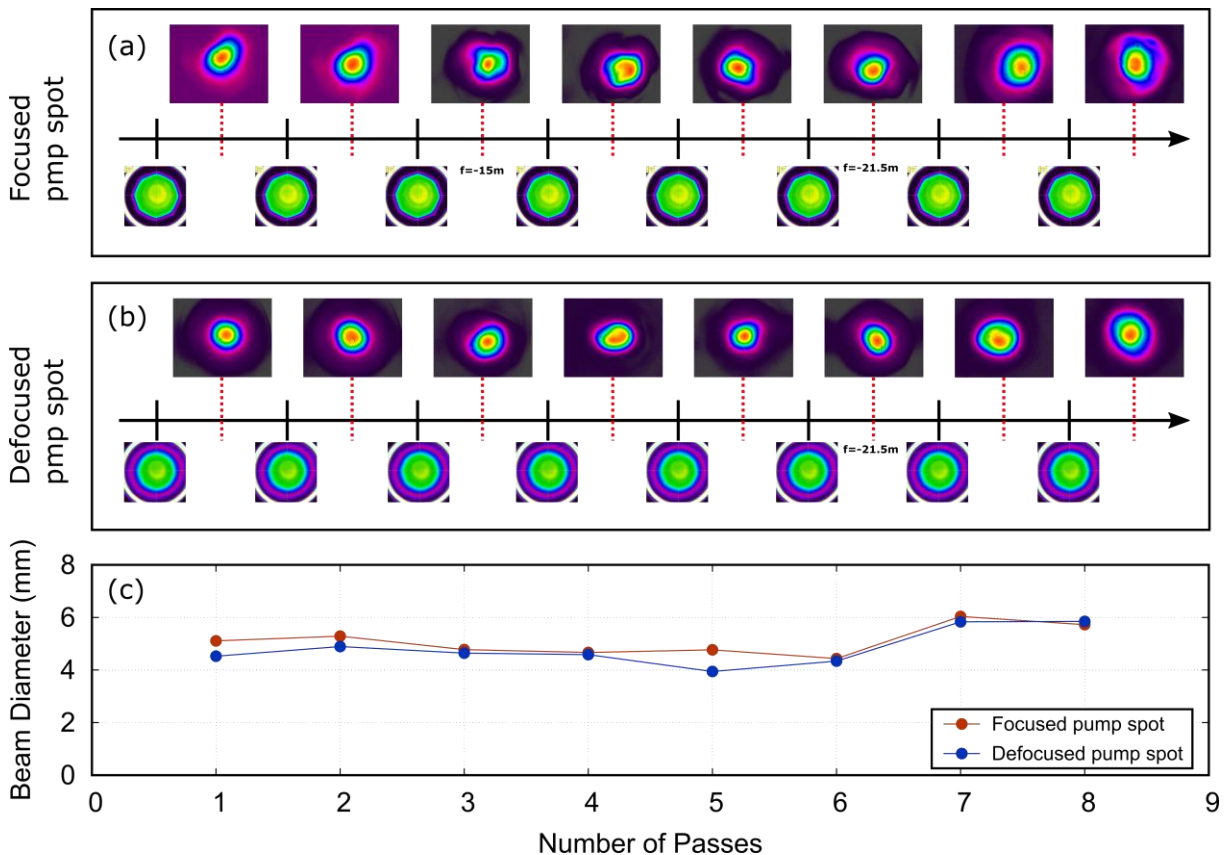


Figure 5.6: Beam profile evolution over 8 disk passes. for a focused pump spot (a) and a de-focused pump spot (b). The beam profiles are shown on the camera chip with a size of 12.5 mm x 10 mm. The pump spot diameter was ~ 12.4 mm. The black solid lines mark the position of the thin disk. The corresponding pictures of the pump spot are included. The beam profiles were recorded at the positions of the folding mirrors between the disk passes, marked by the red dashed lines. Focal lengths of the curved folding mirrors are indicated. (c) X-Y-averaged beam diameters ($1/e^2$) measured using 1D-Gaussian fit curves.

Experiment on the influence of the pump spot size

The effect of a decreased diameter of the pumped area on the thin disk relative to the diameter of the seed laser mode was tested by replacing the 45-mm pump collimation lens with a 50-mm collimation lens. A longer focal length leads to a decreased pump spot diameter, as visualized in Figure 5.4. For the experiment, the seed beam performed six passes over the thin-disk. For the case of a 12.4 mm pump spot diameter, the signal beam diameter increases during the propagation until approximately the width of the camera chip (=12.5 mm) is reached. The initially Gaussian beam profile is altered, going towards a TEM_{01} Laguerre-Gaussian mode. After exchanging the collimation lens, a pump spot diameter of 11.8 mm is achieved. With the same beam folding setup and alignment, the initially Gaussian mode is again altered. Here, the TEM_{01} Laguerre-Gaussian mode shape is more pronounced. Moreover, the beam diameter does not increase after the third pass, but the diameter of less than the height of the camera chip (=10.0 mm) is maintained.

This can be understood by considering diffraction at the soft-aperture of the pumped spot on the laser disk. The wings of the initially Gaussian beam profile overlapping with an unpumped (or lower pumped) region on the thin-disk are amplified less than the center of the beam profile. This leads to clipping of the seed beam at the soft-aperture provided by the pump spot, and hence to a deformation of the initially Gaussian laser mode.

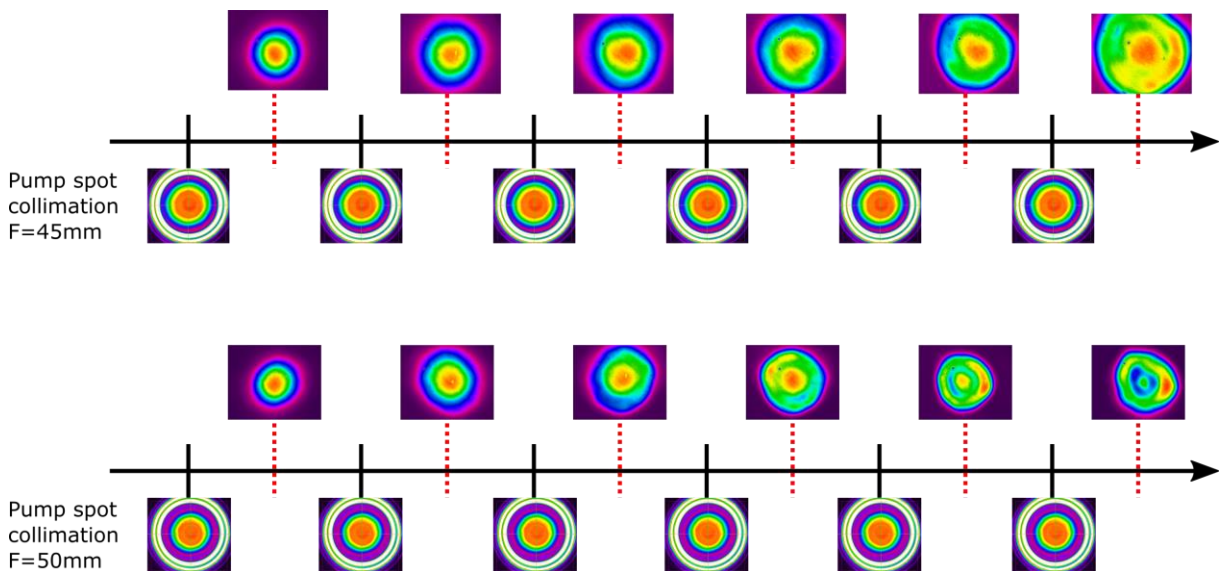


Figure 5.7: Beam profile evolution over six passes for different pump spot diameters. Top: pump spot diameter 12.4 mm. Bottom: pump spot diameter 11.8 mm. The scale is given by the CCD chip size of the beam profiler camera (12.5 mm x 10.0 mm). The pump power was 2.5 kW for both measurements.

5.3 Studies on high-energy pulse amplification

5.3.1 Concept A: Amplifier including 1 thin disk

Experimental Setup

A prototype setup was constructed to test the amplification of pulses using one thin disk amplifier head. The installation included the laser head consisting of pump unit and thin disk, and the folding mirror arrangement on a breadboard.

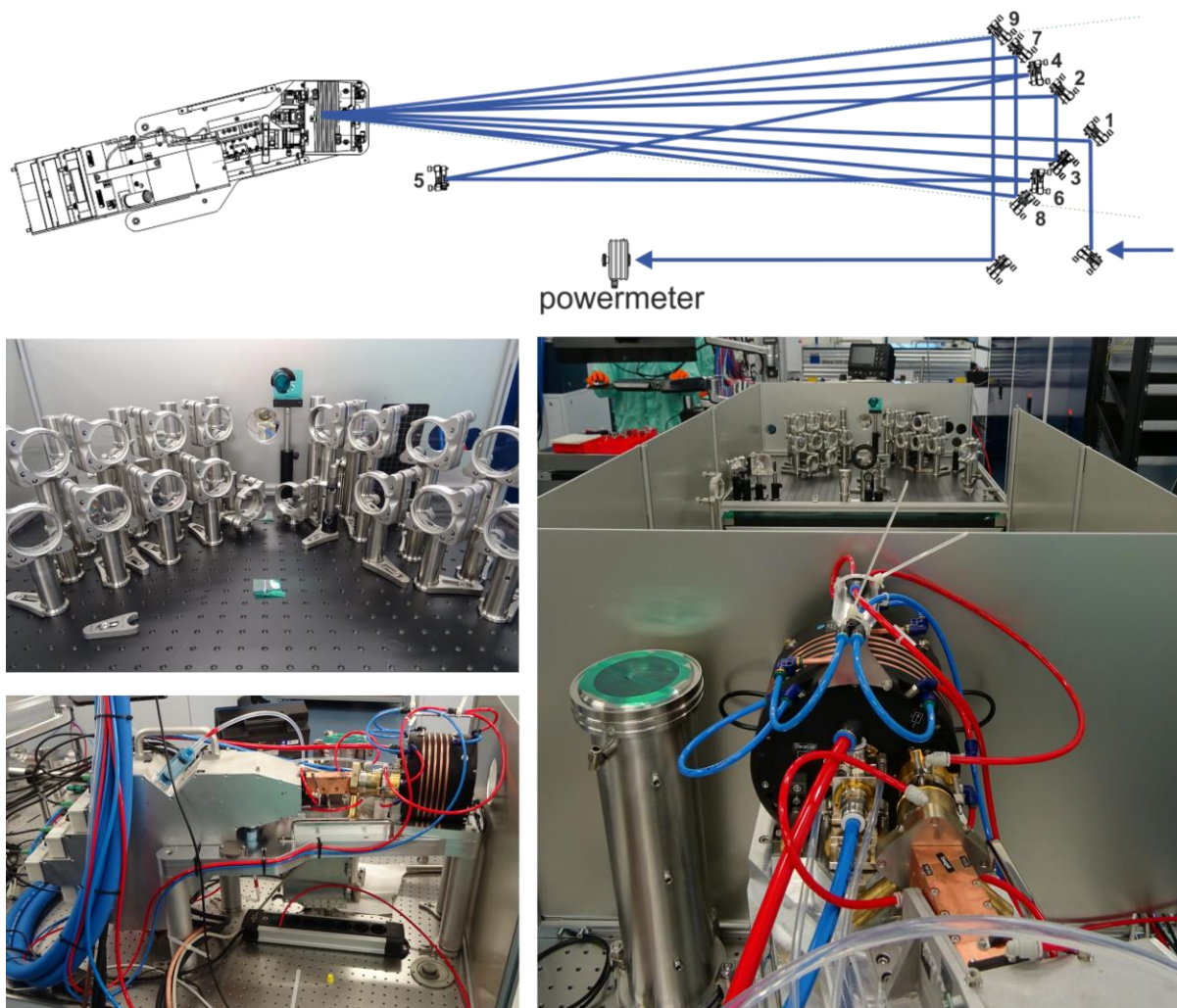


Figure 5.8 Experimental setup of the first multipass amplifier prototype. Top: Schematic top view of the beam propagation for 4 disk passes including a curved mirror after the 2nd pass. Center left: folding mirrors for the geometric multiplexing of the seed over the active medium. Bottom left: Pump unit and thin-disk laser head used for the experiments. Right: Overview of the experimental setup as seen from the side of the laser head.

Experimental results for different amplification passes

The first experiments on pulse amplification were performed using a pump power of 1.82 kW, provided by a pump duty cycle of 30 %. To scale the output pulse energy, pulse amplification measurements were performed with 4 to 10 passes over the disk. While maintaining a constant pump power, the seed pulse energy was slowly increased by increasing the output energy of the regenerative amplifier. The measured data points provide the total gain of the amplifier at the current seed energy. In combination, a characteristic slope for the fixed pump power and number of amplification passes is obtained. The measurements with up to 10 disk passes are shown in Figure 5.9. In case of a small signal, the gain is far from saturation, resulting in a high amplification factor of up to 3.1 for the case of 10 disk passes. At higher input pulse energies the gain decreases, which becomes especially pronounced at a high number of passes, as the cumulated seed fluence through the gain medium is increased. As the saturation fluence is reached, the gain is decreased by a factor $1/e = 37\%$ [4]. For the performed measurement with 4 disk passes, the gain is only reduced by approximately 20 %, while the reduction amounts to approximately 50% for the measurement with 8 disk passes. The measurement with 10 disk passes was interrupted at a seed pulse energy of 100 mJ, as the disk was damaged during the measurement by the amplified pulses.

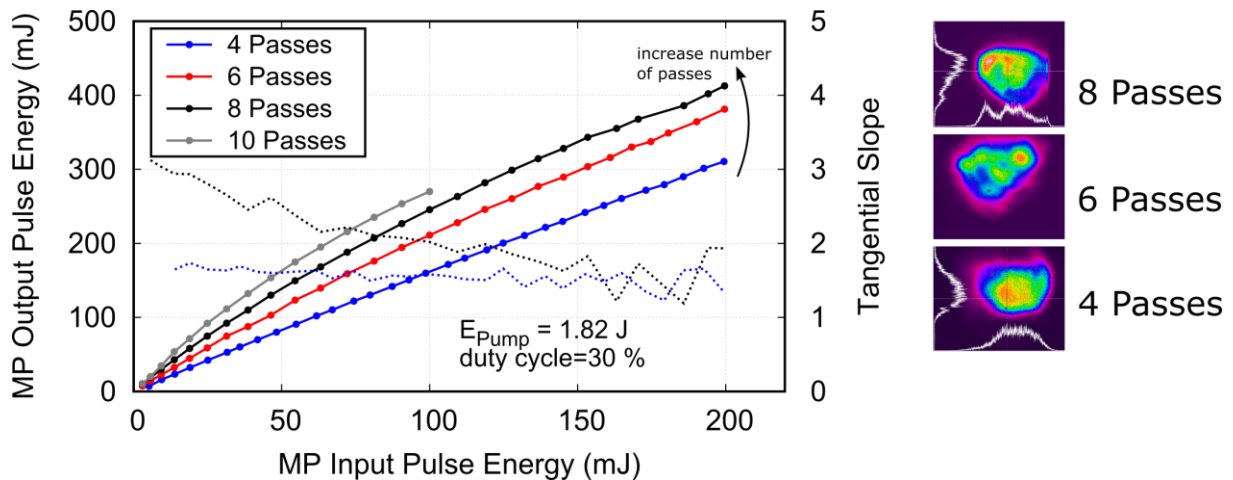


Figure 5.9: Amplification with the first multipass amplifier prototype using one thin disk laser head. Left: Measurement of the output pulse energy as a function of the input pulse energy for 4 to 10 amplification passes. The dashed lines show the instantaneous gain calculated by $G^{(n)}$ for the measurements with 4 (blue) and 8 (black) passes. Right: Near-field output beam profiles after different numbers of amplification passes.

Experiments with reduced duty cycle and increased pump power

Another parameter to increase the achievable output pulse energy from the multipass amplifier is the pump power. The amount of energy stored in the disk clearly depends on the available pump energy per pulse, on the pump intensity, and on the temperature of the gain material. The amplification of pulses at different pump conditions is shown in Figure 5.10 for a constant number of 8 disk passes, starting from the parameters used in the previous plot (see Figure 5.9). In a first step, the pump duty cycle was decreased from 30 % to 20 % while keeping the average pump power constant. Here, the peak pump power was increased from 7.8 kW to 11 kW. An improvement in terms of the output pulse energy of approximately 12 % is obtained, when comparing the previous measurements at a seed pulse energy of 110 mJ.

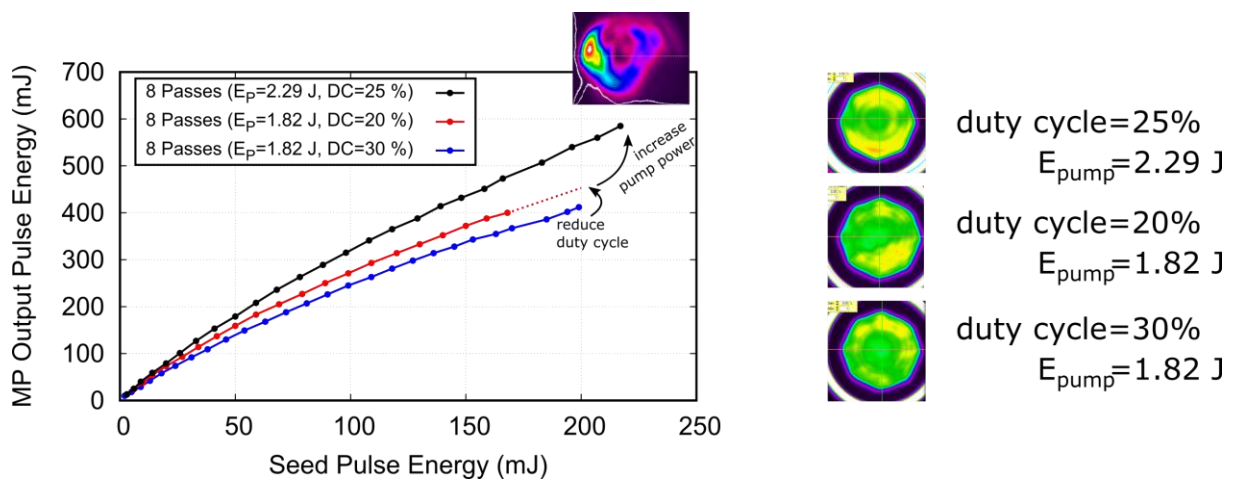


Figure 5.10: Pulse amplification with different pump energies E_p and duty cycles (DC).

This is attributed to both a higher inversion achievable by the increased pump intensity, and a lower thermal load due to the shorter pumping interval. By increasing the pump power to 2.29 kW via a duty cycle of 25 %, the output pulse energy could be increased further to maximum of 585 mJ, at a seed pulse energy of 217 mJ. By comparing the output pulse energy obtained at 110 mJ seed pulse energy, an improvement in terms of the output pulse energy of 16 % is obtained, when comparing with the 20 % duty cycle measurement.

While a high pulse energy could be already be achieved with the presented configuration, the spatial profile of the output beam was far from a fundamental Gaussian mode, as shown in the inset of Figure 5.10. On the on hand, a the relatively large mode overlap with the pump spot (see the fluorescence images in Figure 5.10) provides a high amount of stored energy that can be addressed with the seed beam. On the other hand, any inhomogeneities originating from

the disk surface or the pump intensity distribution are imprinted on the seed beam, leading to the observed wavefront distortions. Maintaining a homogeneous spatial beam profile close to a Gaussian mode is therefore be incorporated for future experiments as a necessary condition for the configuration of the experimental setup.

Experiments optimized for beam quality

As discussed previously, the distortions of the spatial seed beam profile were experimentally found to increase when the beam diameter is large. Maintaining a small beam diameter on the disk can therefore contribute to preserving a homogeneous beam profile, even after several disk reflections.

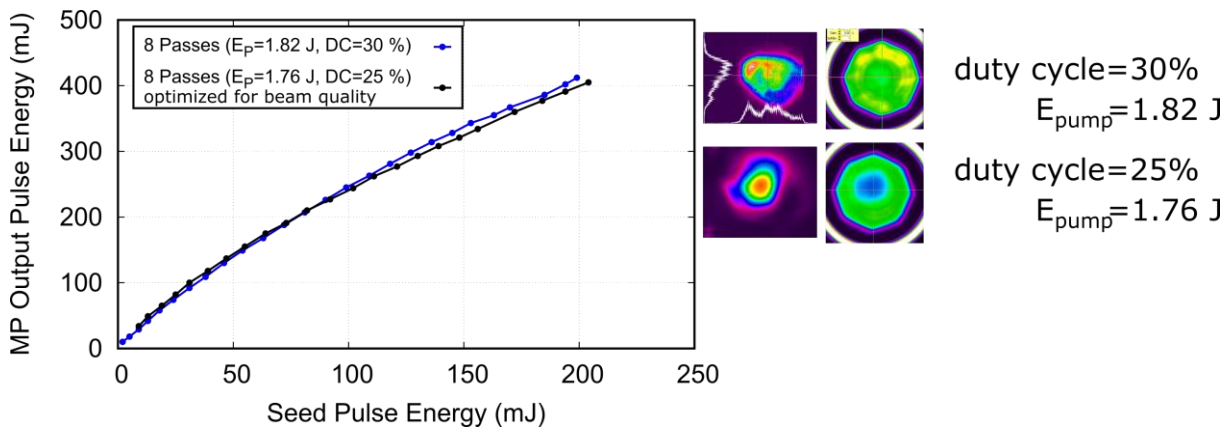


Figure 5.11: Pulse amplification with the alignment optimized for the beam quality.

Furthermore, by slightly tilting the folding mirrors, the positions of the different passes on the disk are transversely shifted. Thereby, the output beam profile can be optimized, as both the inhomogeneous gain distribution caused by the pump spot, and the roughness of the disk are imprinted at different spatial locations in the beam profile. As a cumulative effect, the overall distortion can be minimized by optimizing the alignment, as distortions can then compensate each other. Additionally, the pump power provides a free parameter that can be slightly varied within a narrow interval to optimize the output beam profile.

In Figure 5.11, the measurement of pulse amplification with a beam propagation optimized for the output beam profile is shown. For comparison, the measurement without optimized beam profile is included. The achieved output pulse energy is slightly lower for the optimized measurement, particularly at a high seed pulse energy. This can be understood by taking into account the smaller effective overlap area of the seed laser mode with the pump spot, which causes stronger local gain saturation in the case of the smaller beam diameter with optimization for the beam quality.

In conclusion, by minimizing the seed beam diameter, and by tuning the alignment via folding mirrors and pump power, the beam quality can be optimized, at the expense of a slightly degraded energy extraction efficiency.

Experiments with de-focused pump spot and many amplification passes

Due to the arising local gain saturation, the overlap between the seed beam and the pump spot must be increased in order to achieve a higher output pulse energy. With a higher number of disk passes, this can be achieved while making use of the optimization strategy mentioned in the previous section, i.e. optimizing with folding mirrors and pump power.

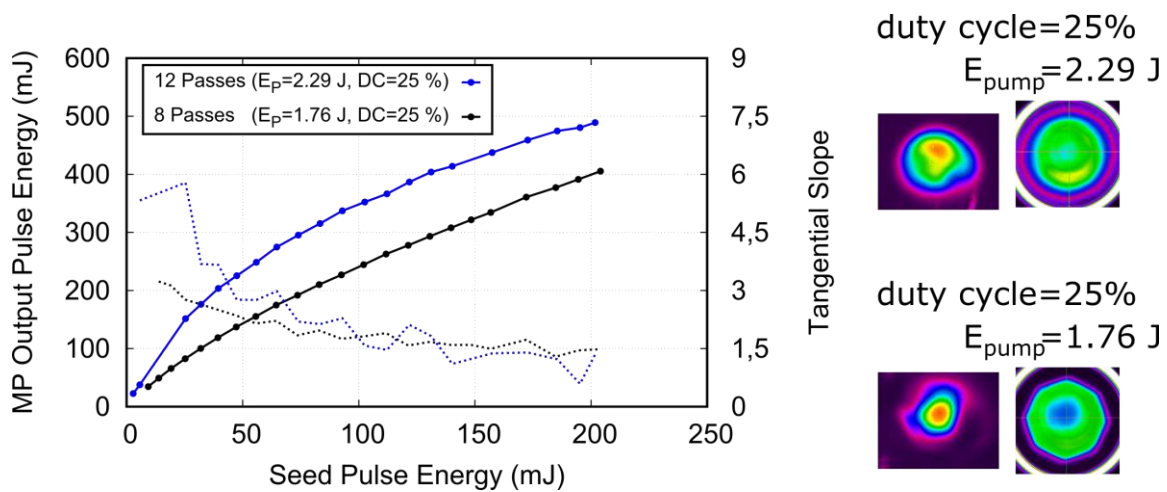


Figure 5.12: Pulse amplification using 12 disk passes and a de-focused pump spot. A maximum pulse energy of 489 mJ is achieved with a homogeneous output beam profile. The measurement with 8 passes (see Figure 5.11) is included as a comparison. The tangential slopes of the two measurements are shown with the dashed lines.

The results from an experiment for pulse amplification using 12 disk passes are shown in Figure 5.12, while the previous measurement using 8 passes is included for comparison. Again, the alignment was optimized for a homogeneous shape of the output beam profile, while the pump power was slightly increased since no beam quality degradation occurred. Additionally, the pump spot was defocused, as described in section 5.2.3. Here, an output pulse energy of 489 mJ was achieved, with a homogeneous output beam shape. The depletion zone in the pump spot also visualizes a higher overlap of the seed with the pump spot as compared with the 8-pass measurement.

An indication for the gain saturation is given by calculating the tangential gain $G^{(n)}$ from the n data points using

$$G^{(n)} = \frac{E_{out}^{(n)} - E_{out}^{(n-1)}}{E_{in}^{(n)} - E_{in}^{(n-1)}} \quad 5.1$$

The tangential gain can be interpreted as the gain for any additional small seed pulse energy at the current seed pulse energy of the n^{th} data point. For higher additional seed pulse energy, the tangential gain will be further reduced. In Figure 5.12 the tangential gain is shown for the measurements with 8 and 12 passes are shown. In the small signal region up to a seed pulse energy of 30 mJ, the tangential gain for the 12-pass measurement is at the maximum value around 6, while it is reduced to ~ 1.4 at a seed pulse energy of 200 mJ, i.e. a reduction to 23%. At the saturation fluence, the small signal gain is reduced to 37% of the initial value [127]. Therefore, the amplifier is operated in a regime above the saturation fluence, and further increasing the seed pulse energy will not significantly improve the extraction efficiency of the amplifier.

The following conclusions can be drawn from the performed experiments:

- The seed beam diameter should be as small as possible to preserve a homogeneous spatial laser mode.
- The duty cycle should be as short as possible with a peak pump power as high as possible. This minimizes the thermal load on the disk and facilitates a high population inversion, leading to a large amount of stored energy and hence, a high gain for the seed pulses.
- By optimizing the alignment of the seed beam on the disk using the folding mirrors, wavefront distortions can partially be compensated by successive passes. Slightly optimizing the pump power within a narrow interval can also contribute to achieve a homogeneous output beam profile.
- Alignment of the different disk passes for optimized output beam quality resulted in a relatively narrow depletion zone at the center of the laser disk. This is detrimental for full energy extraction, suggesting to use more than one laser disk for amplification to higher pulse energies.

Medium-power multipass amplifier based on 1 laser head

Finally, an experimental study was performed using the multipass amplifier layout with one laser head, focusing on a high beam quality, qualified by M^2 measurements according to the ISO16444 standard. Though the output pulse energy could not be amplified to the Joule-level, such an amplifier system can still provide a laser output with competitive parameters, so far unattained by regenerative amplifiers. Moreover, a medium-high pulse energy of 400-500 mJ could be used as a pre-amplifier stage for further amplification. To demonstrate medium-energy pulses with good beam quality, 6 disk passes were aligned on the disk while optimizing pump power, beam diameter, and the seed beam reflection positions on the disk for the spatial output mode homogeneity.

The M^2 measurement setup is shown in Figure 5.13. The beam height is adapter from the multipass amplifier to the M^2 measurement setup using a periscope. A wedged beam sampler (Thorlabs BSF20-B) reflects a portion of 0.5 % of the pulse energy to the M^2 measurement stage. A thin-film polarizer with a half-waveplate is used to adjust the power in the measurement arm. A $f=750$ mm lens is used to focus the beam.

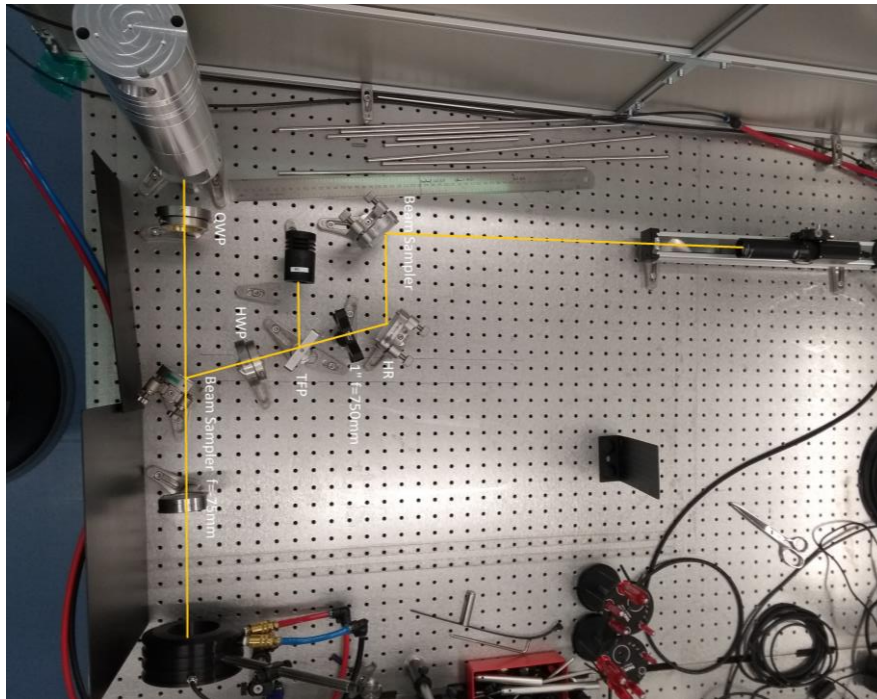


Figure 5.13: M^2 measurement setup for the medium-pulse energy output of the multipass amplifier setup with 1 thin disk laser head. HWP: Half-wave plate. TFP: thin-film polarizer, QWP: Quarter-wave plate.

The results of the M^2 measurements are shown in Figure 5.14. By fitting the measured beam diameters along the z-axis with the model, the M^2 parameter is obtained. For the chosen alignment, the pump power could be adjusted between 2.0 kW and 2.5 kW while the output laser mode diameter was only increased slightly, as can be seen from the measured beam profiles. By increasing the pump power up to 2.5 kW, a pulse energy of almost 440 mJ could be achieved. The corresponding M^2 parameters are plotted on the same axis, showing that no deterioration occurs up to an output power of 420 mJ. As a result, a pulse energy of 420 mJ can be delivered from such a system with an excellent beam quality of $M^2 < 1.5$.

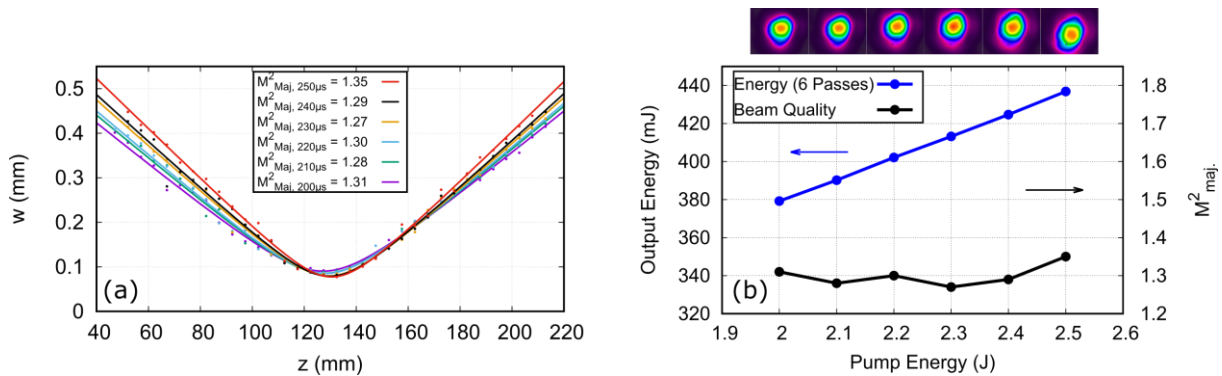


Figure 5.14 M^2 measurements from the 1-head multipass amplifier optimized for the output beam quality. (a): Measured beam caustics along the major axis for the pump power interval from 2.0 kW to 2.5 kW. (b): Output pulse energy and M^2 parameters as a function of the pump pulse energy. The near-field output beam profiles shown on the top correspond to the pump set points.

In summary, pulse amplification with the multipass amplifier comprising 1 thin disk laser head was shown up to an energy of 585 mJ when optimizing the setup for the output power. In this case, however, the beam profile was strongly distorted, caused by inhomogeneities of the thin disk surface due to the thermal load, as well as an inhomogeneous gain across the pump spot. To obtain a homogeneous output beam profile, the experiments showed that the seed beam diameter must be kept as small as possible, and that the positions of the seed passes on the disk must be chosen according to the best output beam profile. Here, 489 mJ could be achieved using 12 amplification passes, but strong gain saturation occurred as most amplification passes were centered on the laser disk. Higher pulse energy can therefore be achieved by providing more stored energy. The number of laser heads was therefore increased for the following concept studies.

5.3.2 Concept B: Amplifier including 2 thin disks

The experimental setup including 2 thin disk amplifier heads is presented in Figure 5.15. Similarly to the previous setup, the beam is folded over the laser disks multiple times using mirrors. A powermeter (Coherent PowerMax PM1k) is used to measure the output power. In this setup, the disks were used in a serial configuration, meaning that the seed pulses are passing them alternatingly. In the example shown in Figure 5.15, 4 passes are realized over each disk by the folding mirrors (FM). Here, thin disk 1 (D1) and thin disk 2 (D2) are passed in the order (D1-FM^{0°}-D2-FM^{45°}- FM^{45°}) x 4. Note that the folding mirrors between D1 and D2 are used under an angle of incidence (AOI) of ~0° (FM^{0°}), while the folding mirrors between D2 and D1 are two AOI=45° mirrors (FM^{45°}). In this layout, curved mirrors to compensate for the thermal lens of the thin disks can be placed between the disks. Thereby, the propagation distance is minimized, as compared to the 1-head setup in Figure 5.8, where transfer mirrors are needed for each pass containing a curved mirror². To increase the number of passes, the folding mirrors can be arranged in different vertical planes, as shown in the photograph (b) of Figure 5.15. The pump units and the thin disk laser heads are shown in the panels (c) and (d).

With this configuration, experiments for pulse amplification were performed in an analogous way as for the experimental setup with one laser head. As described in section 5.3.1, the configuration was optimized to achieve a homogeneous beam profile at the output of the setup. To achieve this, after the finalization of the beam alignment, the input folding mirror was slightly tuned and the pump power slightly adjusted. For the experiments, the seed pulse energy was increased to 233 mJ, to obtain a better extraction efficiency. The output power of this multipass amplifier setup was measured after 2, 4, 6, 8, 10, and 12 disk passes, i.e. after each round-trip in the 2-head experimental setup. The measurement results are shown in Figure 5.16, along with the corresponding output beam profiles. Note that for the measurements with 10 and 12 disk passes, the average pump power was increased from 2.0 kW to 2.2 kW and 2.3 kW, in order to optimize for the output beam profile via the thermal lens of the disks. A pulse energy of 785 mJ was measured at the maximum number of passes (12 passes). The beam profile at this point of operation shows some distortions compared to a Gaussian, however, a homogeneous profile with only low spatial frequencies is maintained.

² Note that in theory off-axis spherical or parabolic mirrors the compensating mirrors can also be integrated in AOI=45° mirrors. However, the cost of such custom shaped optics is much higher than that of conventional spherical mirrors. With the small angles of incidence (typically less than 7°) the astigmatism induced by the spherical mirrors is small.

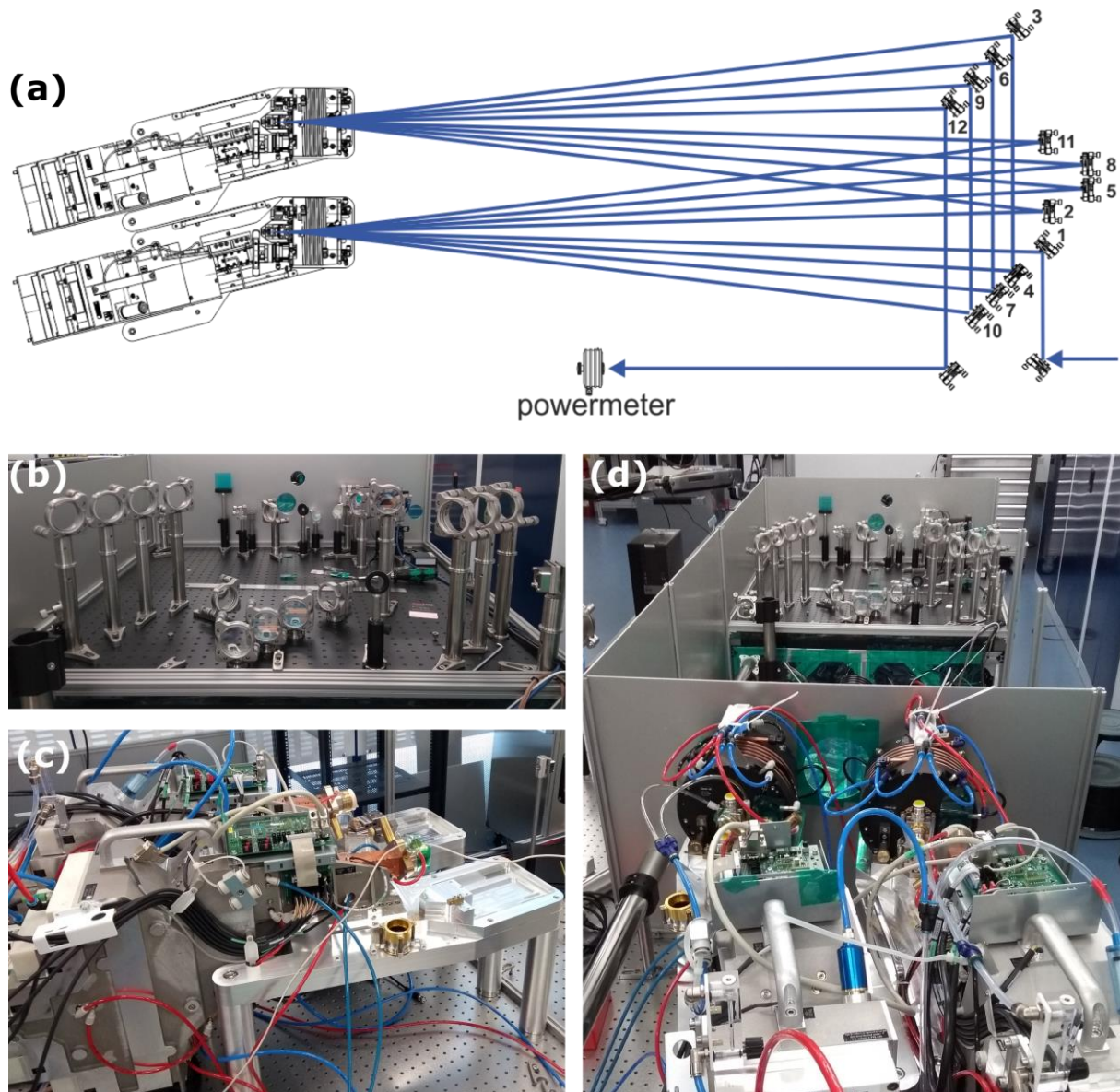


Figure 5.15: Experimental setup of the second multipass amplifier prototype including two thin disk laser heads. (a): Schematic sketch of the beam propagation for 4 disk passes over each disk. The mirrors 2, 5, 8, and 11 can be replaced by curved mirrors, if necessary. The mirror are numbered according to propagation of the beam. (b): folding mirrors setup. (c): Pump units used for the experiments. (d): Overview of the experimental setup as seen from the side of the laser heads.

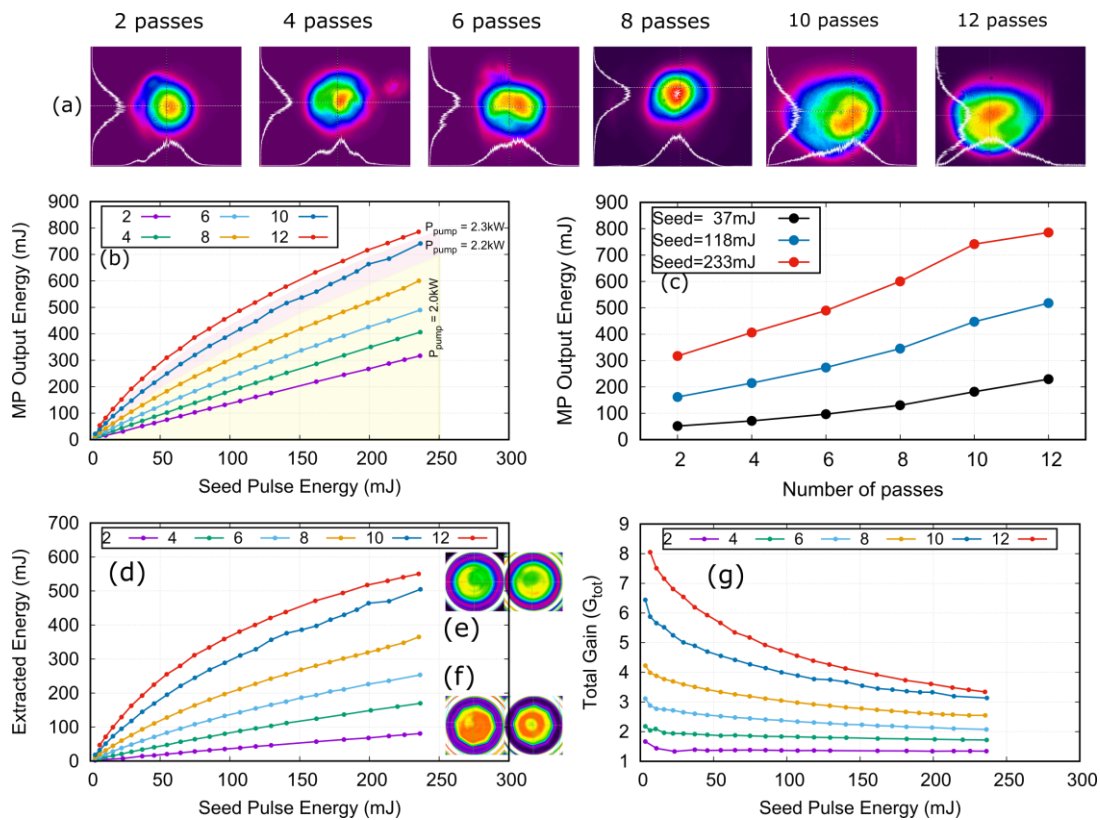


Figure 5.16: Experimental results from pulse amplification with 2 laser heads. (a) beam profile of the amplified output after different numbers of passes. (b) Experimental results of pulse amplification using the setup with two laser heads. (c) The experimental results plotted as a function of the number of passes. (d) Extracted energy calculated from the measured data. The insets show the partially depleted pump spot after 12 (e) and after 2 (f) passes. (g) Total gain of the experimental multipass amplifier setup, calculated from the measured data.

It is interesting to plot the measured output pulse energy as a function of the number of passes, as shown in Figure 5.16 (b). While for a low seed energy, the amplification scales rather exponentially with the number of passes, the amplification is saturated when increasing the seed fluence to 233 mJ. At this point, an increased number of amplification passes will yield only little extra output pulse energy. When plotting the energy extracted from the disks by each seed pulse (Figure 5.16 (d)), a strong reduction of the extraction efficiency (extracted energy per seed pulse energy) can be seen from the measurement with 12 amplification passes³. Here, the gain in the 12 pass measurement is reduced from a factor 8 to a factor 3.3, as shown in Figure 5.16 (g).

³ A constant extraction efficiency would result in an energy extraction scaling linearly with the seed pulse energy.

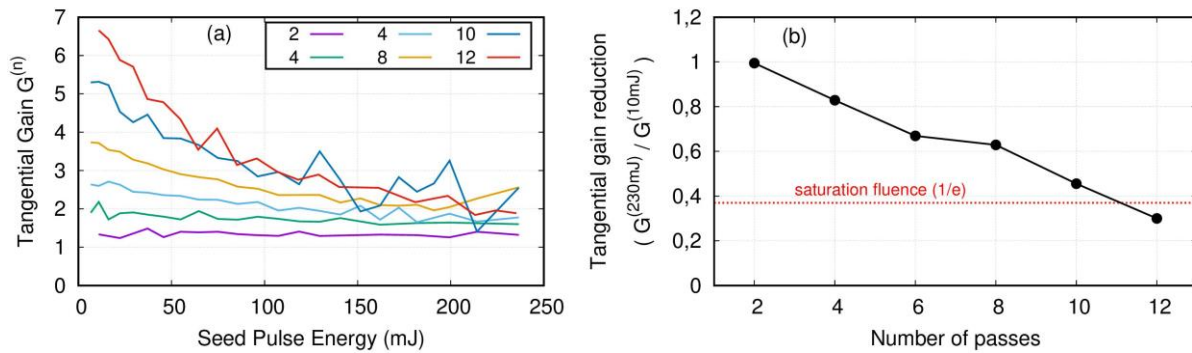


Figure 5.17: Reduction of the tangential gain as a function of the seed pulse energy. for different numbers of amplification passes. The data is calculated from the measurements shown in Figure 5.16. using equation 5.1. (a) Tangential gain for the experimental results. (b) Gain reduction when comparing the gain at high seed fluence ($G^{(230mJ)}$) with low seed fluence ($G^{(10mJ)}$).

To compare the gain saturation with the multipass amplifier concept using only 1 laser head, the tangential gain $G^{(n)}$ curves were calculated according to equation 5.1 for the measured slopes, which is shown in Figure 5.17. In panel (a) the tangential gain is shown for the slopes with 2 to 12 amplification passes. The maximum reduction of the tangential slope with respect to the small signal values at low seed energy was calculated according to $G^{(230mJ)} / G^{(10mJ)}$, which is shown in panel (b) of the figure 4. While for a small number of passes the tangential gain is only reduced to >80% of the initial value, a maximum gain reduction to 30 % is achieved for 12 amplification passes. This means that the cumulated seed fluence at this point has already surpassed the saturation fluence at the depleted zone of the pump spot, which would reduce the gain to 37 % of the initial value [127]. A way to reduce the cumulated seed fluence on the disk is given by increasing the cumulated area of the seed on the disk, which can be achieved either by increasing the seed beam diameter, or by scanning across the disk area with different amplification passes. It was shown in section 5.3.1 that with these methods the energy extraction efficiency can indeed be increased, however, the beam quality is strongly deteriorated. On the other hand, attempting to further increase the output pulse energy by realizing more than the 12 amplification passes will further reduce the tangential gain. Therefore, a significantly higher output pulse energy is not expected.

Results from the experimental setup using two laser heads including high-energy pulse compression (470 mJ, 900 fs) have been presented in 2019 by the author of this thesis [128].

⁴ Note that for the strongly fluctuating curves (8 and 12 passes), the mean value of $[G^{(200mJ)}; G^{(200mJ)}; G^{(230mJ)}]$ was taken.

Comparison to concept A

The improvement of the amplifier system achieved by integrating a second laser head into the experimental setup can be visualized by comparing the amplification slopes of the experiments performed at the same number of passes (=12) and the same pump power (=2.3 kW). The slopes are shown in Figure 5.18. First, the output pulse energy could be increased from approximately 500 mJ to 780 mJ. This corresponds to an extracted energy of 280 mJ for the first setup and 550 mJ for the second setup, i.e. 275 mJ per laser disk. The output pulse energy could therefore be scaled via the number of integrated laser disks. Second, to achieve a high output beam quality (i.e. homogeneous output laser mode), the experimentally optimized alignment resulted in a depletion zone with limited stored energy content that can be addressed by the seed. Therefore, higher output pulse energy could not be achieved from this setup.

To achieve higher output pulse energy, a straight-forward and simple possibility is given by up-scaling the number of laser heads integrated in the amplifier. This effectively results in more total pump power and more total stored energy that is available for pulse amplification. Though for small signals the same total gain is expected at an equal number of disk passes, at high seed fluence the gain is expected to saturate less. This route was realized for the multipass amplifier concept C which is presented in the next section.

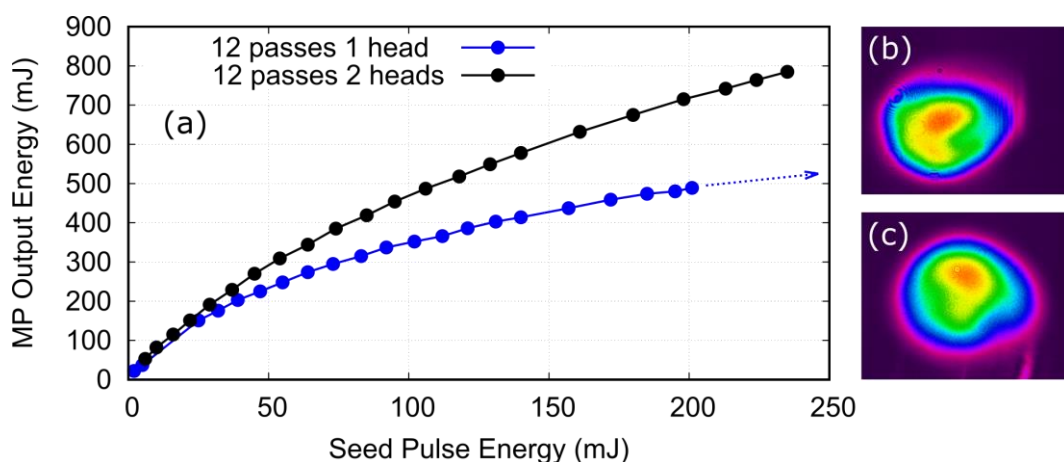


Figure 5.18: Comparison of experimental results using 1 laser head and 2 laser heads. (a) Experimental results for the pulse amplification. (b) Collimated output beam profile for the measurement with 2 laser heads. (c) Collimated output beam profile for the measurement with 2 laser head.

5.3.3 Concept C: Amplifier including 3 and 4 thin disks

In the third experimental setup, a total number of 4 thin disk laser heads were integrated and arranged similar to concept B, as described in section 5.3.2. An overview of the setup is provided in Figure 5.19. The beam routing is indicated by the numbering of the folding mirrors as an example for an experimental setup including 4 laser heads, with 3 amplification passes on each disk.

As a first step, experiments with 3 disks were performed for different numbers of amplification passes. The experimental results are shown in Figure 5.20 (a) and (b). Up to the maximum number of 9 amplification passes, the tangential gain of the slopes is only reduced to 75 % of the initial value (i.e. from ~ 4 to ~ 3), indicating that unextracted energy is still stored in the disks. Note that the pump power was slightly increased (+ 10%) after achieving the full seed energy. In panel (b), the experimental results are plotted as a function of the number of passes. For comparison, the experimental results using only 1 and 2 laser heads are included. Clearly, an improved performance can be seen when comparing the output energy after 9 amplification passes when using 3 laser disks (720 mJ) and 2 laser disks (~ 620 mJ).

As a second step, a measurement using all four laser disks was performed. The experimental results are included in Figure 5.20 for comparison with the other results. Again, the pump energy was increased by $\sim 10\%$ after achieving a seed pulse energy of 217 mJ. Finally, an output pulse energy of 863 mJ was achieved. At this point of operation, laser-induced optical damage on the thin-disk prevented to obtain even higher pulse energy with the setup.

In conclusion, the integration of further thin-disk laser heads for the multipass amplifier allowed to gradually achieve higher pulse energy while maintaining a smooth beam profile. The high amount of stored energy available in the amplifier with four thin-disk laser heads allowed for a pulse energy above 860 mJ obtained with a maximum number of 12 disk passes. In this configuration, the amplifier is still operated in a regime with relatively low energy extraction (i.e. below the saturation fluence for the seed). The gain at the full seed energy is therefore still high. As a consequence, the beam propagation in the amplifier is not altered significantly while ramping up the seed energy, and the alignment and beam quality of the small signal at low seed energy is maintained also for the full output power. Moreover, compared to the multipass amplifier concept B, the same pulse energy can be achieved here with at least one disk pass less, which can be crucial when aiming for an optimal beam quality. Despite a relatively poor overall power efficiency, this concept allows for a stable amplifier with cutting-edge laser parameters that have not been attained with other concepts.

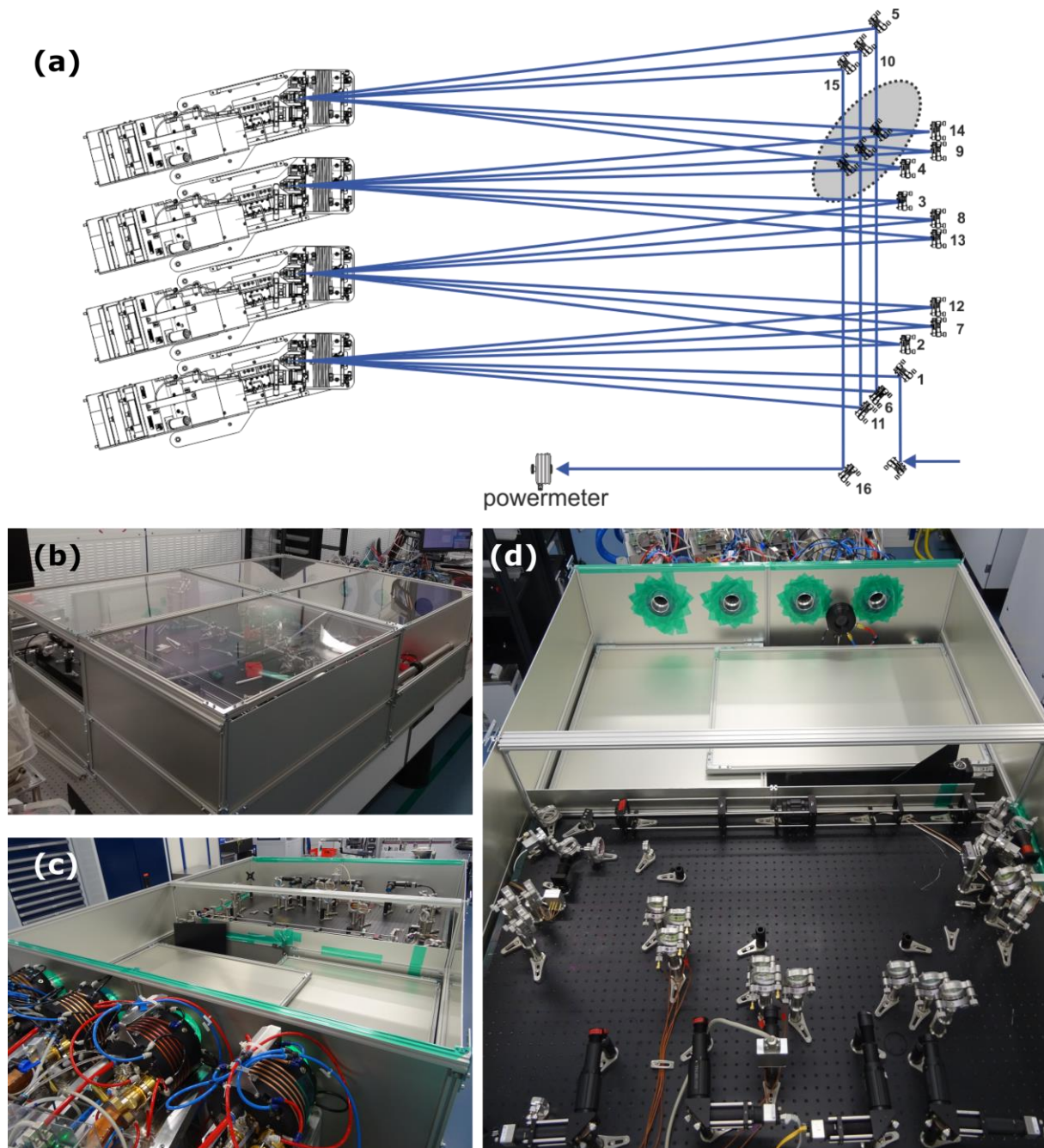


Figure 5.19: Experimental setup of concept C with 4 thin disk lasers heads integrated. (a) Schematic sketch of the beam propagation in a zig-zag path alternatingly passing the four laser disks. In the sketch, 3 passes over each disk are indicated. For the experiments using only 3 laser heads, the mirrors in the grey shaded area were used. (b) Photograph of the closed experimental setup used to reduce air turbulence during pulse amplification. (c) Photograph of the experimental setup as seen from the side of the 4 serial laser heads. (d) Top view photograph of the experimental setup.

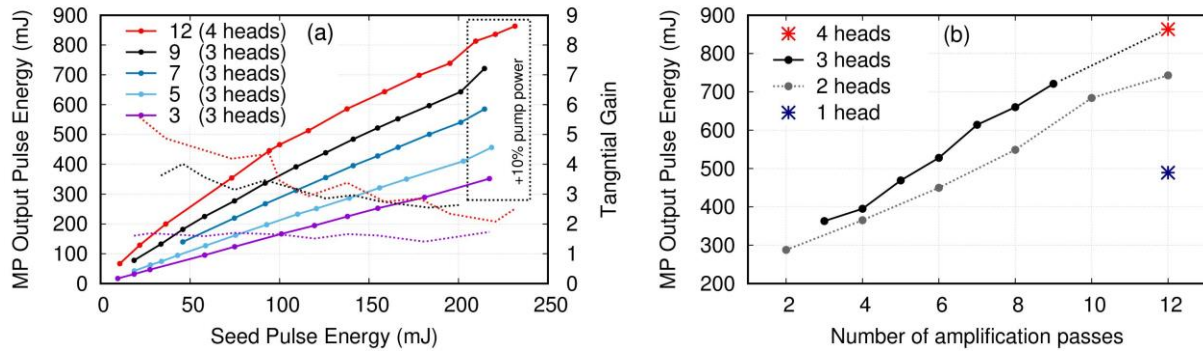


Figure 5.20: Experimental results from the setup including up to 4 thin disk laser heads. (a) Output pulse energy as a function of the input pulse energy. The dashed lines indicate the tangential gain of the curves with equal color. For clarity, the curves with 5 and 7 passes have been spared. (b) Measured data plotted as a function of the number of amplification passes. For comparison, some experimental data from the setups using 1 and 2 laser disks are included.

5.4 Final Multipass Amplifier Layout

The final design for the multipass amplifier is based on the experimental concept C, as presented in the previous section (5.3.3), including 4 thin-disk laser heads. Differently to concept C, the final amplifier was divided into two stages to achieve an optimal trade-off between beam quality and output pulse energy. A schematic drawing of the setup is shown in Figure 5.21, where the two stages are marked. The input beam is stabilized against pointing fluctuations using a piezo-controlled beam stabilization stage before entering the multipass amplifier. Here, the first two thin-disk laser heads are used to amplify the 240 mJ seed pulses from the regenerative amplifier to an energy of 550 mJ. The next two laser heads are used for the final amplification of the pulses to 800 mJ, before the temporal compression of the pulses. To actively stabilize the beam inside the amplifier against thermal drifts, piezo-controlled mirrors are used together with position-sensitive detectors in a closed-loop configuration. ASE and other stray light emitted from the laser heads is shielded to a large degree by the water-cooled pinholes in order to minimize heating of the optomechanical parts.

Separating the amplification process in two stages has two advantages. First, the beam diameter can be varied and adapted for different seed pulse energies, limited by the laser-induced damage threshold (LIDT) of the optics. In the first stage, the diameter of the seed beam is kept as small as possible to minimize the phase aberrations induced in the gain medium. In the second stage, the beam diameter is slightly increased, in order to account for the higher pulse energy.

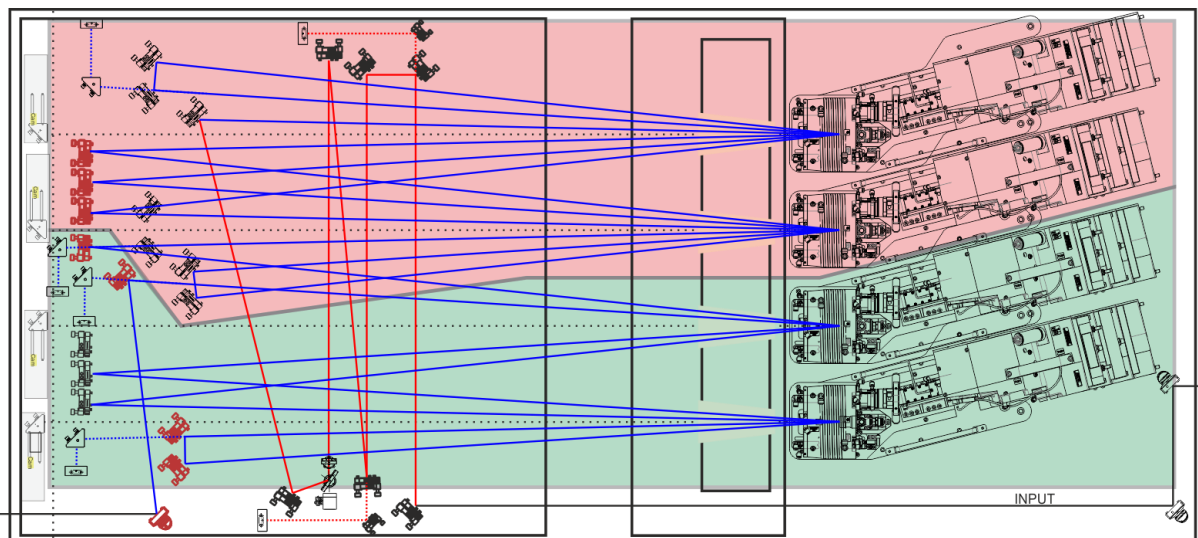
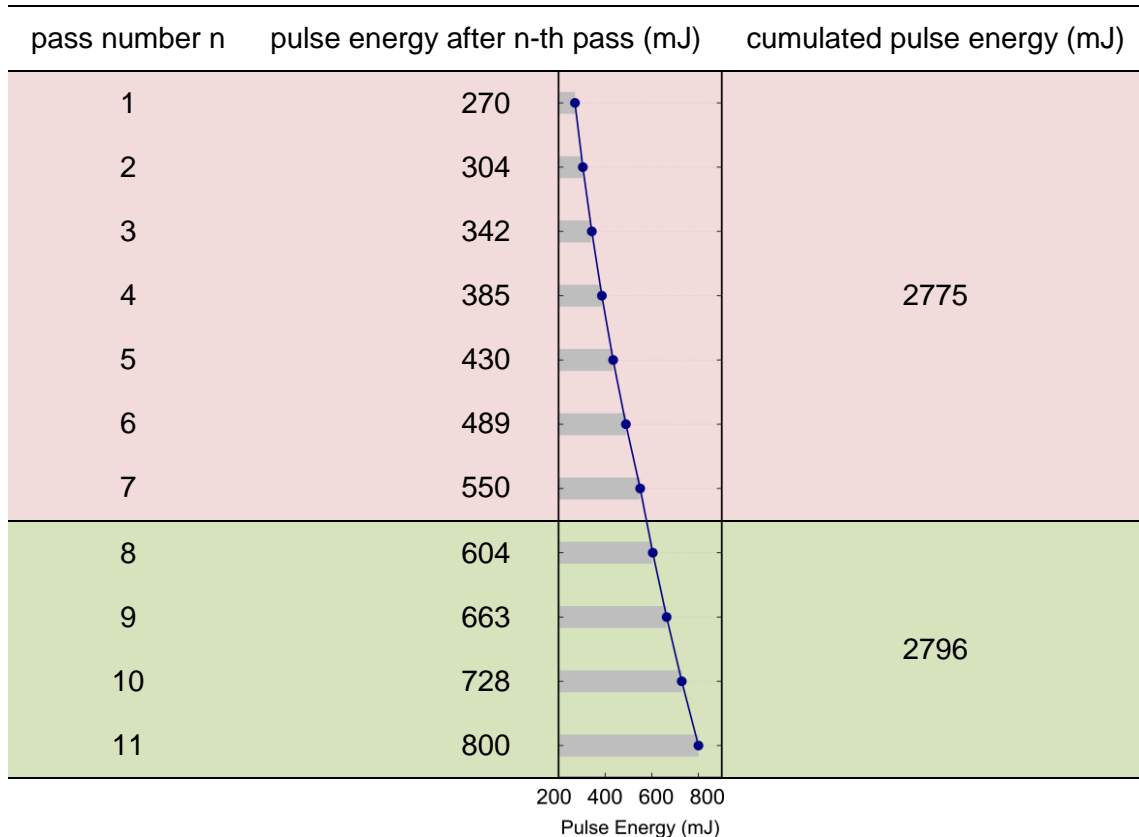


Figure 5.21: Schematic top view of the final multipass amplifier. The stages 1 and 2 are marked shaded in red and green, respectively. Beam propagation of in-coupling and input stabilization is marked in red. Beam propagation in the multipass amplifier is marked in blue. Beam propagation at the input and output is marked in black.

As a second advantage, the number of passes performed in each amplifier stage can be chosen such that the cumulated seed pulse energy in each stage is similar (see Table 5.1). This allows for the operation of the two stages in similar regimes with respect to energy extraction, optimizing the overall achieved gain. Moreover, a similar effective seed mode area on the disks of both stages can be achieved by slightly scanning the reflection positions of the smaller spots on the disks of stage 1, while the same positions are maintained for the larger seed beam on the disks of stage 2.

The beam diameters after different numbers of amplification passes are shown in Figure 5.22. The typical beam diameter in stage 1 is around 5 mm, which is increased to approximately 6 mm in stage 2. The beam profiles used to measure the beam diameter are stacked on top of Figure 5.22. It is interesting to note that the beam profiles at some intermediate positions in the multipass amplifier may be inhomogeneous and far from round (see eg the beam profile after pass number 6). However, the beam profile may restore its roundness and homogeneity after performing more amplification passes, where phase distortions and lateral inhomogeneous gain may be compensated. The optimum alignment can be found by slightly optimizing the alignment via the folding mirrors.

Table 5.1: Cumulated fluence in the two multipass amplifier stages.



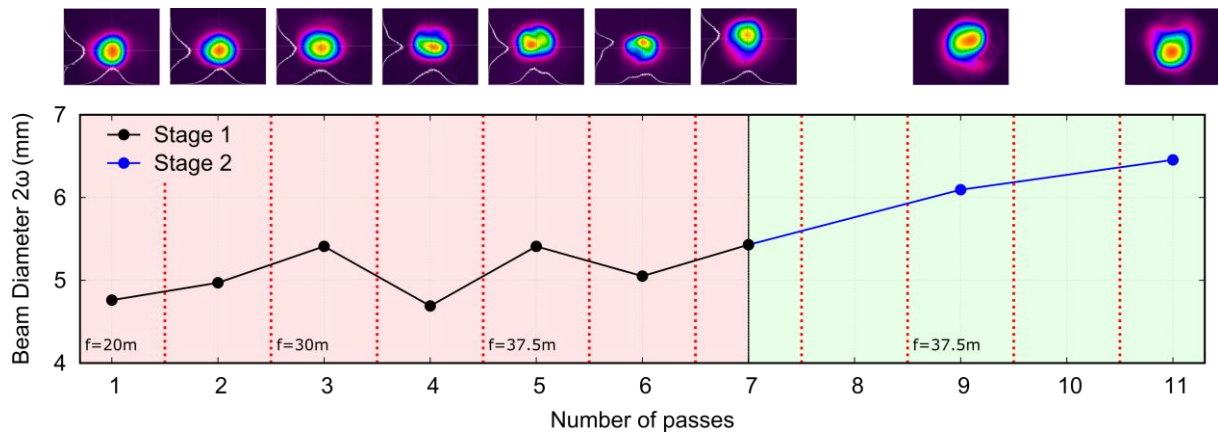


Figure 5.22: Beam propagation inside the final multipass amplifier setup. The average of the beam diameter along the x and y directions after each of the disk passes is plotted, obtained from the measured beam profiles. The positions of the disk passes are marked with red dashed lines. 7 passes are performed in stage 1 (red shading), 4 passes are performed in stage 2 (green shading). The beam profiles are measured using the leakage behind the folding mirrors. The focal length of the refractive optics between the disk passes is indicated.

Performance characterization of the final multipass amplifier

The results of the characterization of the final multipass amplifier output are summarized in Table 5.2, together with the measurement instrument and method.

Table 5.2: Summary of the output parameters of the final multipass amplifier.

Laser Parameter	Instrument	Value
average output power	powermeter	<810 W
pulse energy	photodiode	<810 mJ
pulse duration	SHG autocorrelator	>920 ps
Spectral bandwidth	grating spectrometer	1.7 nm (FWHM)
collimated output beam profile	CCD camera	
beam quality after compression (M^2)	CCD camera & lin. stage	
pulse energy stability ⁵	photodiode	0.76 % (rms)
long term stability ⁶	photodiode	0.56% (rms)

⁵ Statistics of 10,000 consecutive laser pulses.

⁶ Statistics of the mean pulse energy values calculated every 1000 consecutive laser pulses.

The measurement of the output pulse energy as a function of the seed pulse energy is shown in Figure 5.23 for different numbers of amplification passes in the final multipass amplifier system. The corresponding profiles of the output beam are included. A pulse energy of 550 mJ is reached after stage 1 at a seed pulse energy of 240 mJ. With two more passes in stage 2, the pulse energy is increased to 660 mJ, and after 4 passes in stage 2 the maximum of >800 mJ is obtained. The spatial profiles of the collimated output are shown in the insets (b) - (d). The beam quality of the output beams at the different pulse energies was characterized by determining the M^2 parameter according to the ISO 11146 standard [110,111], using a home-built setup including a linear stage and a CCD camera. A lens with a focal length of 1000 mm was used for the measurements. The experimental results are shown in Figure 5.24 (a) - (c), together with the corresponding beam profiles of the collimated beam (near field) and the beam profile near the waist position (far field). The average of the M^2 parameter along the major and minor axis for the output beams before pulse compression is rather constant with $(M^2_{\text{Major}} + M^2_{\text{Minor}})/2 = 1.6$. However, an increased astigmatism can be deduced from the measurement at 800 mJ, which may be due to curved optics (thin disk, compensating mirrors) being used with non-zero degree angles of incidence. The beam profiles measured near the waist position (see the insets on the right-hand side) resemble Gaussian modes and show that the beams can be tightly focused, despite the deviation from a fundamental Gaussian mode in the near field.

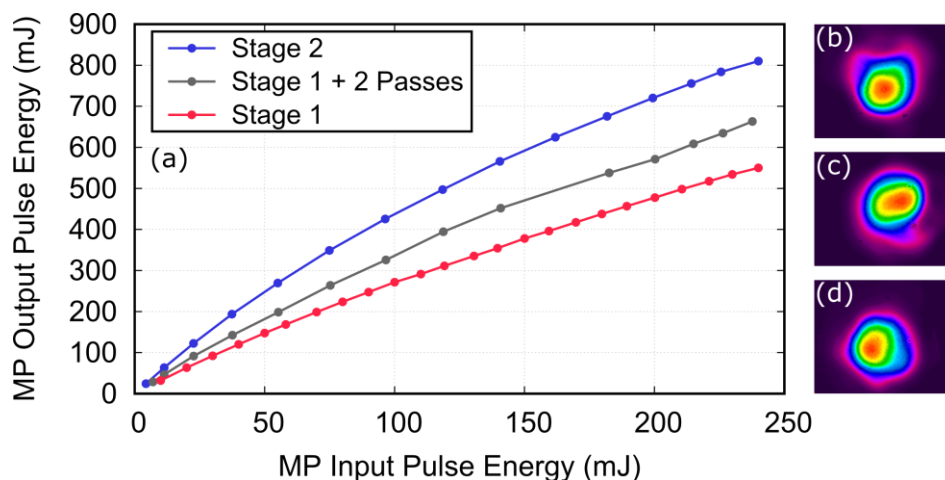


Figure 5.23: Performance of the multipass amplifier. (a) Slopes from operation using 7 (Stage 1), 9 (Stage 1 + 2 Passes), and 11 (Stage 2) disk passes. (b)-(d) Collimated beam profiles measured at the output of the multipass amplifier at 800 mJ (b), 660 mJ (c), and 550 mJ (d).

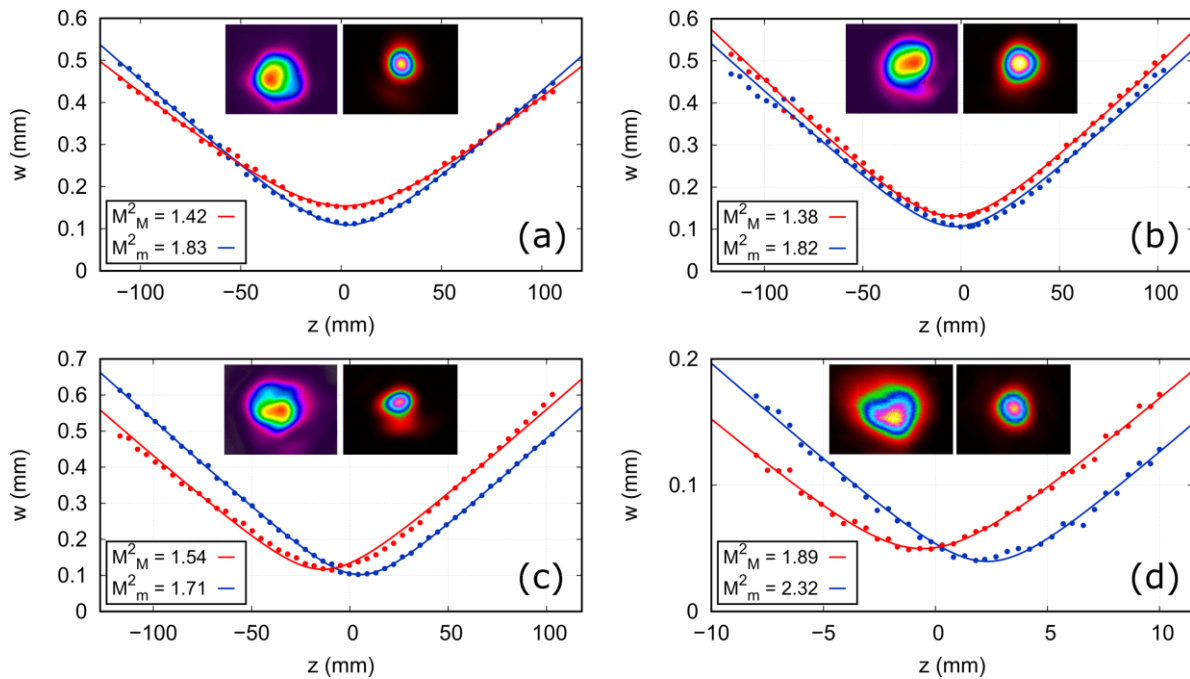


Figure 5.24: M^2 measurements at of the two multipass stages. The insets show the collimated output beam profile (left) and the beam profile in the focus (right). (a)-(c) Measured before compression. (a) Stage 1 at 500 mJ output pulse energy (7 disk passes). (b) Stage 1 plus 2 passes in stage 2 (in total 9 disk passes) at 660 mJ. (c) Stage 2 at 800 mJ (11 disk passes). (d) Measured after compression at 720 mJ pulse energy.

The beam quality is deteriorated after pulse compression, as can be seen from the M^2 measurement in Figure 5.24 (d). The mean M^2 parameter is increased to 2.1, however, the mode profile near the beam waist (see right-hand side inset) still appears round, again indicating a high intensity enabled by the tight focus. Note that the beam was expanded by a factor of 4 before pulse compression. Therefore the focal beam diameter is also decreased by a factor of 4 down to $<50 \mu\text{m}$, which introduced a higher amount of noise in the measurement, as the spatial resolution by the CCD camera pixels remains constant ($3.75 \mu\text{m}$ pixel pitch).

After compression, the pulse duration was measured using an SHG autocorrelator (APE pulseLink 150). The corresponding spectrum was measured with a commercial grating spectrometer (Ocean Optics HR4000). Both measurements are shown in Figure 5.25 (a) and (b). A spectral bandwidth of 1.71 nm (FWHM) was measured, while from the autocorrelation a temporal pulse duration of 920 fs (FWHM) was obtained by fitting a sech^2 curve to the experimental data. Note that here, the convolution factor that converts between the width of the optical pulse and the SHG autocorrelation signal was calculated by a Fourier analysis of the measured spectrum. To obtain a realistic result of the Fourier-transform limited pulse duration, the spectrum was hard cut off at the wings as visualized in Figure 5.25 (c).

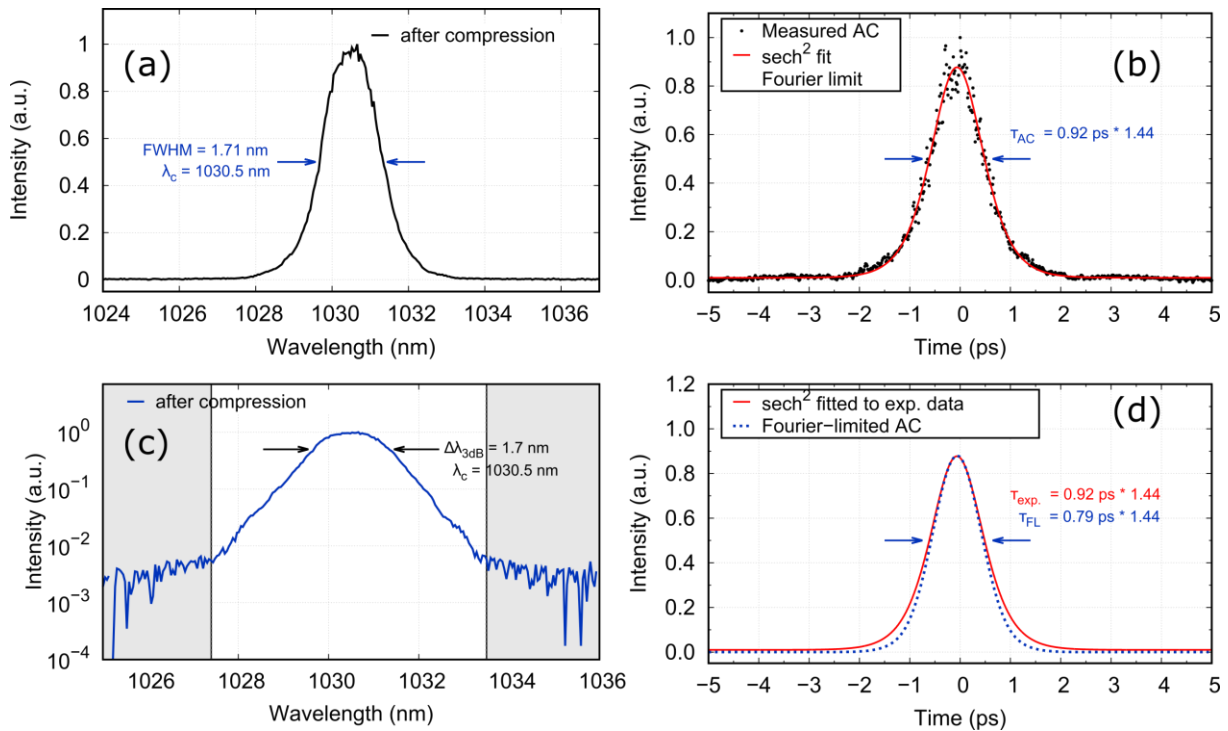


Figure 5.25: Spectrum and autocorrelation trace of the compressed output at 720 mJ. (a) Spectrum measured with a commercial grating spectrometer. (b) Autocorrelation trace fitted by a sech^2 curve, resulting in a FWHM of 920 fs. (c) Spectrum from (a) plotted on a log scale. The grey shaded data (<1027.4 nm & >1033.5 nm) is cut off for the Fourier analysis. (d) Autocorrelation of the Fourier-limited pulse calculated from the measured spectrum. The sech^2 fit from (b) is included for visualization. A deconvolution factor of 1.44 is obtained.

The determination of the cut-off position is based on an educated guess, taking as a reference the enhanced noise which is clearly visible when plotting the data on a logarithmic scale (see Figure 5.25 (c)). From the remaining spectral intensity, a Fourier-transform limited pulse duration of 790 fs was obtained, which corresponds to the dashed autocorrelation trace shown in Figure 5.25 (d). Despite experimental efforts to approach closer to the Fourier transform-limited pulse duration via compressor alignment, no further improvement was possible. This could indicate higher-order dispersion of the spectral phase of the pulses, which could originate from a mismatch between the dispersion of the CFBG and the grating compressor, and could thus not be reversed completely.

The output beam profiles of stage 1 and stage 2 were measured using CCD camera, both before and after passing the pulse compressor. The results are shown in Figure 5.27. Note that the beam profiles are not to scale relative to each other, as different cameras were used for the beams before compression (Spiricon LT665) and after compression (Basler Beat beA4000-62km). This was due to the 4-fold beam expansion between the multipass output and the compressor realized by a telescope based on curved mirrors.

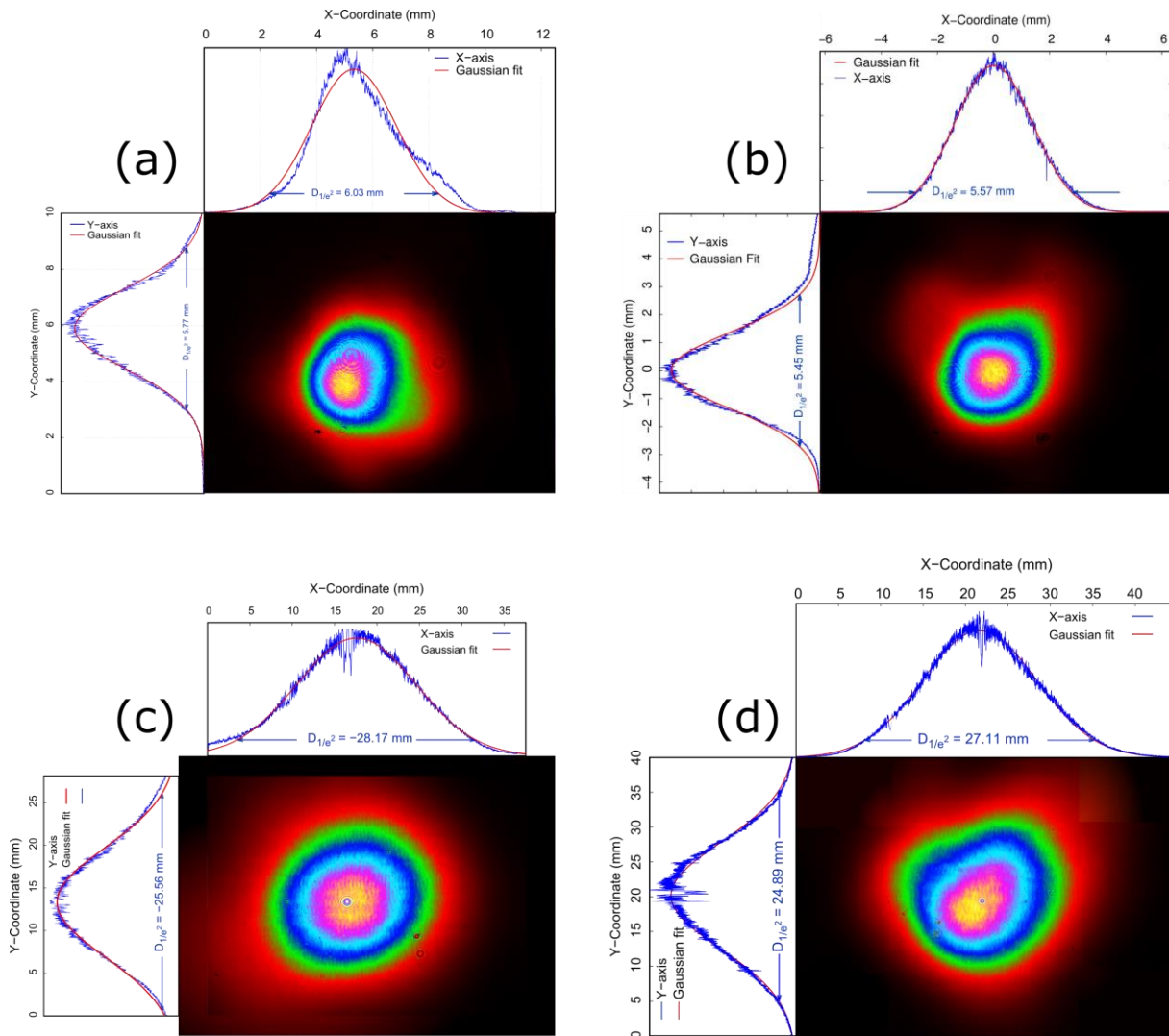


Figure 5.26: Collimated output beam profiles. (a): Before compression after stage 1 (550 mJ). (b): Before compression after stage 2 (800 mJ). (c): After compression after stage 1 (495 mJ). (d): After compression after stage 2 (720 mJ).

The beam profile in Figure 5.26 (c) was recorded after being de-magnified by a lens by a factor of 0.5. The beam profile in Figure 5.26 (d) was recorded without de-magnification at different transverse locations, which were stitched to obtain the full beam profile. When comparing the beam profiles before and after passing the compressor, it can be seen that a similar shape is obtained despite the 4-fold magnification.

The stability of the final multipass amplifier was characterized both on a short-term and a long-term scale. The pulse energy was measured using a photodiode which was calibrated with a powermeter by dividing the measured average power by the repetition rate.

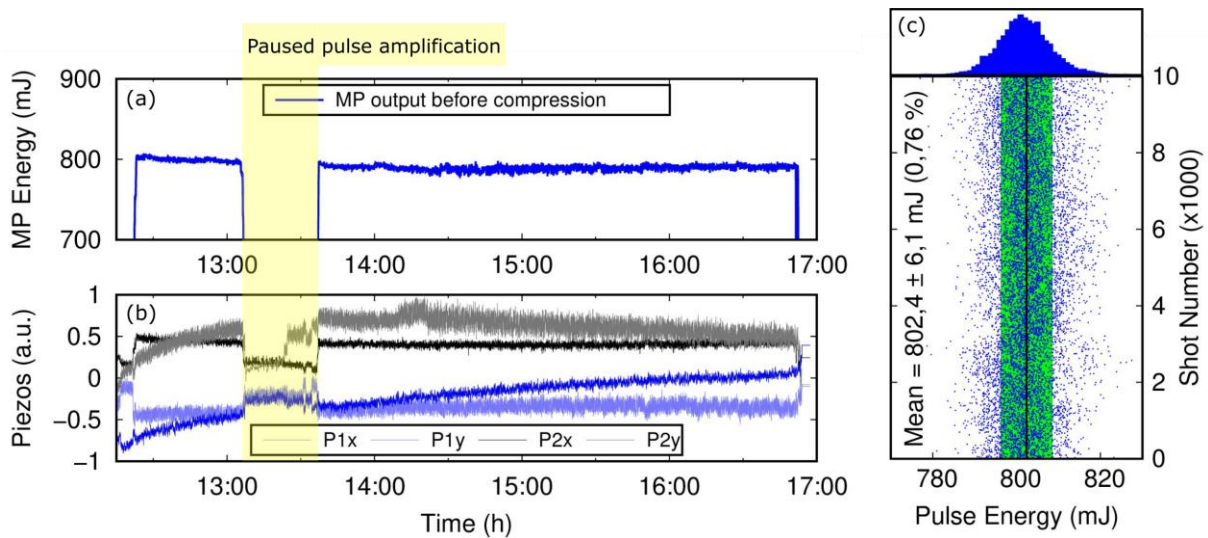


Figure 5.27 Stability of the multipass amplifier. (a) Output pulse energy measured with a calibrated photodiode over a time period of >5 hours. During the marked time interval, the seed pulse energy was ramped down but the pump remained at full power. (b) Simultaneously recorded positions of the piezo-controlled mirrors used to stabilize the beam against thermal drift. (c) Pulse-to-pulse energy stability determined from the measurement of 10,000 consecutive laser pulses. On the top the data is summarized in a histogram.

To measure the short-term stability, the energy of 10,000 consecutive laser pulses was measured and analyzed, as shown in Figure 5.27 (c). From the measurement, an rms energy stability of 6.1 mJ was obtained, corresponding to an rms-fluctuation of 0.76 % around the mean value of 802.4 mJ. To determine the long-term stability, the mean energy values of 1,000 laser pulses were recorded, providing one data point per second. The measurement was performed over approximately 4.5 hours, as shown in Figure 5.27 (a). The measurement contains a period of 30 min where the pump power was maintained, but the seed energy was ramped down. Therefore, thermalization continued, as the main heat source is the pump light. This can be seen from the positions of the piezo-controlled mirrors stabilizing the beam inside the multipass amplifier, which are shown in Figure 5.27 (b). While the mirror positions in y-direction are drifting during the first hour when warming up, the positions are more stable after the first hour of the measurement. The continued thermalization is thereby reflected by the recurrence of the piezo mirrors to the same positions before ramping down and after re-ramping up the seed energy. In conclusion, long-term stable operation over more than 4.5 hours could be demonstrated with a short-term (pulse-to-pulse) energy stability of 0.76 % rms.

5.5 Completed LLR Laser System

In this section an overview of the completed laser system is given, as it was delivered to the field experiments performed in the framework of the LLR project. Its performance including first results on laser filament generation is described in detail in a recent publication by the author of this thesis [62]. A schematic overview is presented in Figure 5.28. As the front end, the seed laser with the CFBG and the regenerative amplifier described as in chapter 3 are used. For the multipass amplifier, the final layout presented in section 5.4 was implemented. The pulse compressor was realized as described in the next chapter 6.

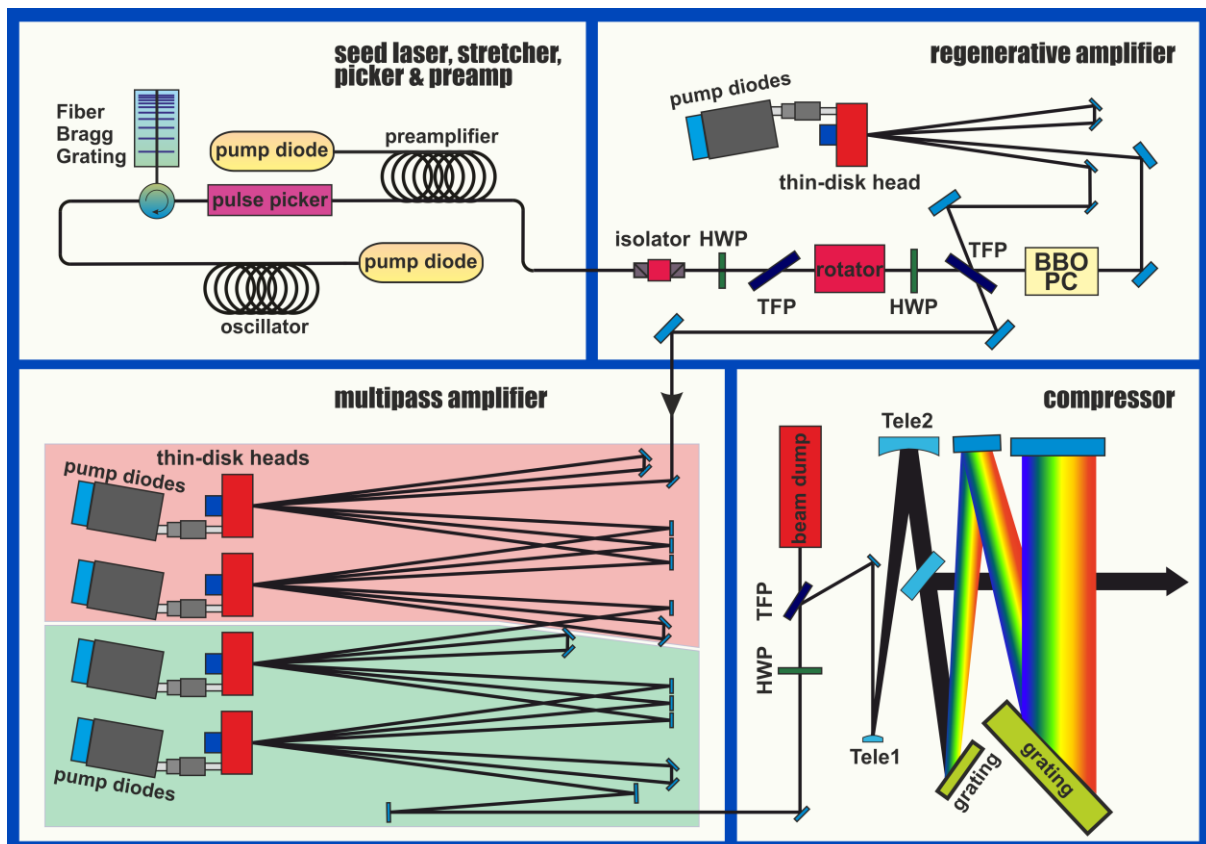


Figure 5.28: Schematic sketch of the final setup of the developed laser system. The seed pulses are stretched by a CFBG and pre-amplified in a fiber amplifier. The pulses are amplified to 240 mJ in the regenerative amplifier. Final amplification takes place in the multipass amplifier, which is set up in two stages (stage 1 shaded in red, stage 2 shaded in green). A grating pair is used to compress the pulses to <1 ps before the output.

For the experimental deployment, the laser system was divided into five modules, that can be transported separately and assembled at the experimental site. Each module is supported by an aluminum frame featuring castor wheels. The alignment of the modules is preserved by centering pins, and rigidity between the modules is achieved by several large-diameter bolts and screws in the support frame. A photograph of the assembled laser system at the first experimental site (LAL, Orsay, France) is shown in Figure 5.29. The overall dimensions of the system are 8.0 x 1.4 m x 1.2 m. The laser is protected by a tent with an air conditioning unit reducing large ambient thermal excursions. A mobile fan filter unit is used to provide filtered air locally for laser alignment and maintenance. The output beam is housed by a metal tube and fed through the tent wall. In the final experiment, a factor-7 beam expander will be used to magnify and steer the laser beam (see Figure 7.7), and the beam will be fully housed all along its propagation path to prevent strong turbulence before beam expansion. More details can be found in [64].



Figure 5.29: Photograph of the completed laser system used for experiments. From left to right, the regenerative amplifier, multipass amplifier, and grating compressor are visible.

6 Dispersion Management and Pulse Compression

6.1 CPA Design and Pulse Stretching

Chirped pulse amplification (CPA) was first demonstrated by D. Strickland and G. Mourou in 1985 as a novel method to achieve prior unattained pulse energies and peak powers [6], which has unlocked a new era for the field of ultrafast lasers. By temporally stretching the seed pulses, the peak power can be decreased by several orders of magnitude, allowing for much higher pulse energies below the laser-induced damage threshold (LIDT) of optical components as compared to the original pulse duration. At the same time, nonlinear effects such as self-focusing and self-phase modulation are strongly reduced or even avoided, which is beneficial for the beam quality and the linear (spectral) behavior of the laser amplifier. Since its invention, the technique has been technologically matured and is today indispensable for state of the art ultrafast lasers with peak powers at or significantly above the terawatt level.

Temporal pulse stretching

The laser system at hand is implemented as a chirped-pulse amplification chain. Before amplification first to the multi-millijoule level and finally to the Joule level, stretching of the seed pulses is achieved by two chirped fiber Bragg gratings (CFBG), matched to the dispersion of the grating compressor described in 6.2. Compared to grating-based pulse stretchers, the CFBGs require much less space and they can be integrated into the fiber-based seed laser by using an optical circulator (see Figure 5.28). The spectral transmission of the CFBGs is shown in Figure 6.1 together with the group delay as a function of the wavelength.

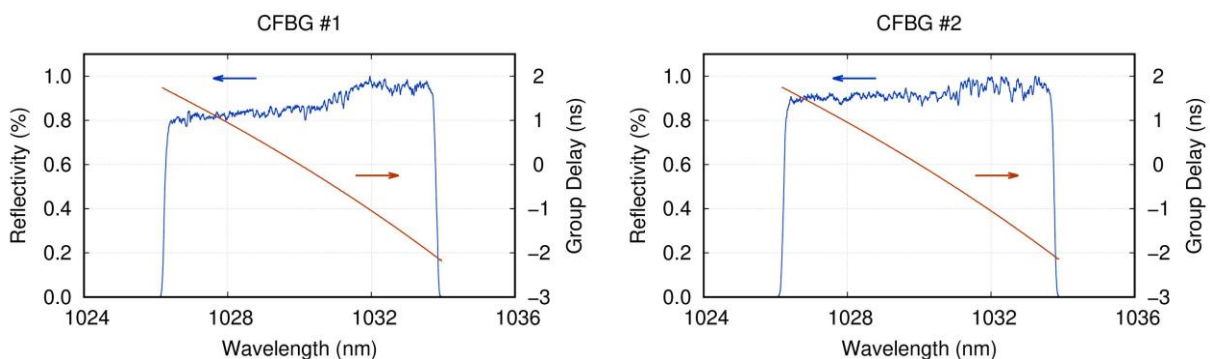


Figure 6.1: Transmission and dispersion of the two chirped fiber Bragg gratings used for stretching the low-power seed pulses. The reflectivity is approximately 70 % with a bandwidth of 8 nm centered around 1030 nm. A GDD of approximately -500 ps/nm can be deduced for each CFBG, which amounts to an effective GDD of approximately -1 ns/nm used to stretch the seed pulses.

From the slope of the group delay, a group delay dispersion of approximately -500 ps/nm can be deduced for each CFBG, amounting to -1000 ps/nm effectively seen by the seed pulses. With the measured spectra for the seed and amplified output pulses shown in Figure 6.8, this translates to a stretched FWHM pulse duration of ~4 ns for the seed pulses (spectral FWHM ~4 nm), and ~1.7 ns for the amplified pulses with 800 mJ before the compressor (FWHM ~1.7 nm).

Waveshaper

After the CFBGs, a waveshaper (Finisar WaveShaper 1000A) was implemented in the seed laser, providing additional flexibility in the dispersion management. This includes:

- Spectral amplitude shaping of the seed pulses to pre-compensate for gain narrowing during pulse amplification.
- Spectral phase shaping to compensate for any dispersion mismatch between the CFBGs and the grating compressor.
- Spectral phase shaping to introduce additional dispersion without realignment of the grating compressor, which can be used to control the final pulse duration for application in experiments where the pulse duration must be swept.

In Figure 6.2 the response of the pulse duration on the manipulation of the GDD with the waveshaper is shown. For the measurement, the compressor alignment was optimized for a pulse duration of 1 ps, and the pulse duration (FWHM) was measured using an intensity autocorrelator. The measurement shows an approximately linear increase of the pulse duration with the absolute value of GDD added with the waveshaper. Note the opposite directions of the frequency chirp for positive and negative dispersion values.

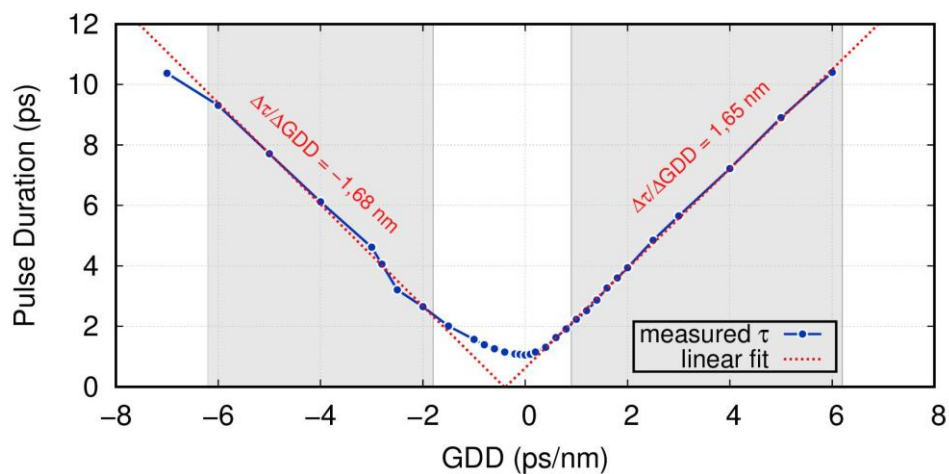


Figure 6.2: Pulse duration as a function of the GDD, controlled by the waveshaper. Linear curves are fitted to the data within the shaded areas. The slopes of the fit give the spectral bandwidth corresponding to the temporal pulse width (both FWHM).

From a practical perspective, negative values of the dispersion parameter D_λ in units of ps/nm mean positive dispersion by definition of the group delay dispersion (see section 2.1.2.2). Therefore, when negative values in ps/nm are applied with the waveshaper, the long-wavelength part of the pulse spectrum is temporally promoted to the front of the pulse, while the short-wavelength part is delayed to the end of the pulse. This corresponds to a pulse after propagation in a normal chromatically dispersive medium such as fused silica or air. Therefore, to (pre-)compensate for chromatic dispersion, positive values have to be used for the dispersion parameter D_λ . When no additional dispersion is introduced by the waveshaper, the pulses are fully recompressed after passing the grating compressor. The layout and the alignment of the grating compressor are described in the following sections.

6.2 Layout of the Grating Compressor

In this section, the layout of the pulse compressor for the constructed laser system is described. The compressor is based on multilayer dielectric reflection gratings, arranged in a Treacy-type configuration [85], i.e. with each grating being passed twice by each pulse. The grating size and line frequency is chosen to meet the requirements regarding

- Total spectral bandwidth with hard cut-offs as limited by the aperture of the gratings.
- Maximum fluence on the gratings allowed to prevent optical damage.
- Optimized diffraction efficiency.
- Sufficient vertical extension of the small grating for beam separation after compression.

In Figure 6.3 a sketch of a grating compressor in the Treacy-configuration is shown. The dimensioning of the optical components is outlined in the following.

Minimum input beam size

With a laser-induced damage threshold (LIDT) of 2 J/cm² at a pulse duration of 10 ps [129][PGL]⁷, the LIDT at the targeted pulse duration of 900 fs can be estimated by using the scaling law proposed in [130]:

$$\begin{aligned} \text{LIDT} &\propto \tau^k \\ \Rightarrow \text{LIDT}(0.9\text{ps}) &= \text{LIDT}(10\text{ps}) \cdot \left(\frac{0.9\text{ps}}{10\text{ps}}\right)^{0.33} = 0.9 \text{ J/cm}^2. \end{aligned} \tag{6.1}$$

For a beam with a Gaussian profile, the peak fluence surpasses that of a rectangular pulse by a factor ~2. Hence, to obtain an accurate value with respect to the pulse energy and the (1/e²) beam diameter, the LIDT must be divided by 2, resulting in a value of 0.45 J/cm². For the further calculation, an additional safety factor of 3 is included, leading to an effective damage threshold LIDT_{eff} = 0.15 J/cm². Together with the maximum expected compressed pulse energy E_{max}=1 J, the minimum beam diameter 2w at a pulse energy E_{max}=1 J can be calculated:

$$\begin{aligned} F &= \frac{E_{\max}}{A} < \text{LIDT}_{\text{eff}} \\ \Rightarrow 2w &> \sqrt{\frac{E_{\max}}{\pi \cdot \text{LIDT}_{\text{eff}}}} = 29.1 \text{ mm}. \end{aligned} \tag{6.2}$$

⁷ Note that the given damage threshold refers to the plane perpendicular to the beam which is incident at an angle of 60° onto the grating surface, so the value can be directly used for the calculations.

Here, F is the real fluence, and $A = \pi \cdot r^2$ is the area inside the beam diameter.

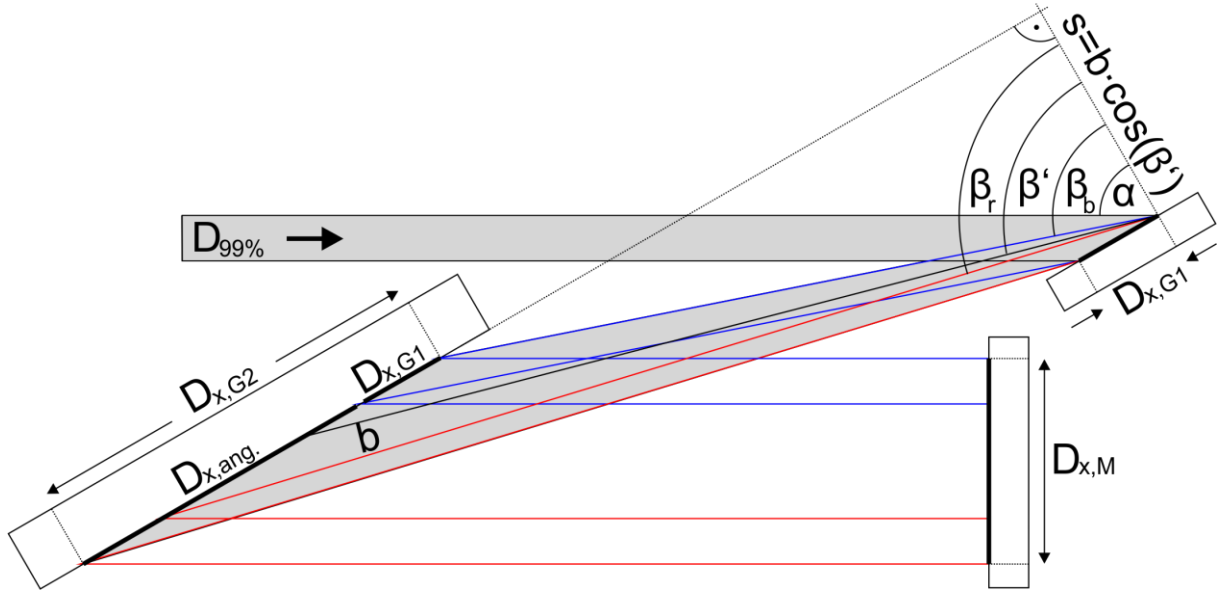


Figure 6.3: Schematic sketch for the layout of the grating compressor (not to scale). See the text for details.

The calculated minimum beam diameter $2w = 29.1$ mm refers to the $1/e^2$ width of the beam, containing 86% of the total energy. To determine the minimum size of the gratings, the beam width corresponding to an energy content of 99%, $D_{99\%} = 1.52 \cdot 2w = 44,23$ mm is considered. The dimensions for the following analysis of the compressor are visualized in Figure 6.3.

Beam spot size on the first grating

Projection of the $1/e^2$ beam diameter onto the first grating under the designed incidence angle of $\alpha=60^\circ$ gives the illuminated width $D_{x,G1}$ in horizontal direction:

$$D_{x,G1} = \frac{D_{99\%}}{\cos(60^\circ)} = 88.4 \text{ mm.} \quad 6.3$$

An approximately double-sized width of 170 mm was chosen for the first grating, in order to provide some buffer space for alignment and to ensure no diffraction or power loss due to the hard aperture.

The beam spot size in the vertical direction remains unchanged, as the grating is tilted in the horizontal direction only. To ensure no optical power loss at the hard aperture, the grating must extend over a minimum of $> D_{99\%} = 88.4$ mm in the vertical direction. In order to spatially separate the input and output beam, the dimension must be doubled, i.e. >176.8 mm. An additional space of 20 mm between the spots of the input and output beam as well as $\sim 15\%$ buffer space lead to a total height of the small grating of 230 mm.

Beam spot size on the second grating

To determine the illuminated width on the second compressor grating, first, the beam diameter in x-direction $D_{x,G1/G2}$ between the two gratings in the plane perpendicular to the propagation direction is calculated under neglect of the angular dispersion of the gratings. It is given by the projection of the spot on the first grating to the plane perpendicular to the propagation direction of the central wavelength components:

$$D_{x,G1/G2} = D_{x,G1} \cdot \cos(\beta'_{(\lambda_c)}) = 28.5 \text{ mm} \quad 6.4$$

The length of the grating compressor b is determined by the dispersion of the CFBGs ($D_2 \approx -1000 \text{ ps/nm}$) according to equation 2.31, with the dispersion angle of the central wavelength $\beta'_{(\lambda_c)}$ given by equation 2.25:

$$b = \frac{cd^2}{2\lambda} \cos^2(\beta'_{(\lambda_c)}) \cdot D_2 = 4.87 \text{ m} \quad 6.5$$

The width of beam spot size on the second grating is determined by both the width of the beam under projection onto the grating surface, and by the maximum angular dispersion of the longest (β_r) and shortest (β_b) wavelength component of the pulses. From the CFBGs, a maximum bandwidth of approximately 7 nm is given. For the calculation, therefore the shortest wavelength component is at 1026.5 nm, and the longest at 1033.5 nm. This results in an angular separation of 2.19° (see equation 2.25), which leads to a spatial separation after propagation from the first to the second grating of $D_{x,ang.} = b \cdot \tan(2.19^\circ) = 186 \text{ mm}$. The combined beam width on the second grating $D_{x,G2}$ can then be calculated using:

$$D_{x,G2} = (D_{x,G1/G2} + D_{x,ang.}) \cdot \frac{1}{\cos(\beta'_{(\lambda_c)})} = 668 \text{ mm} \quad 6.6$$

With a safety space of 10 %, the required grating width would therefore amount to 701 mm.

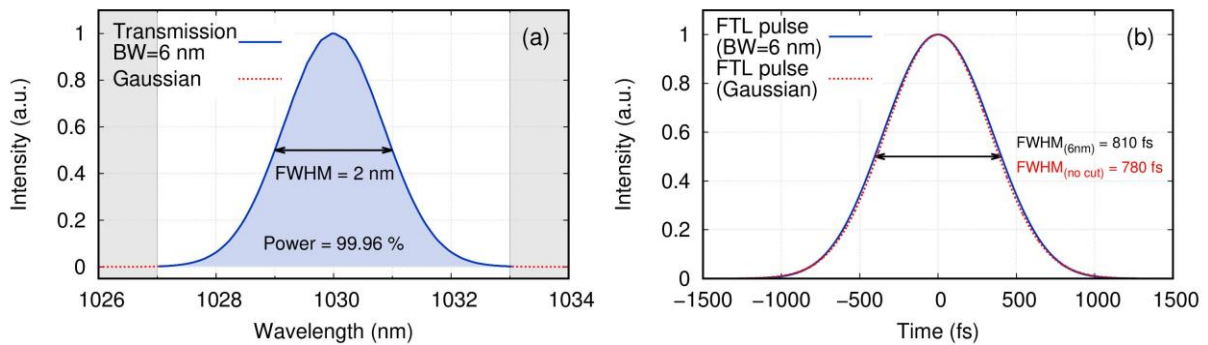


Figure 6.4: Fourier transform limited pulse duration before and after a bandpass. (a) Gaussian spectrum with FWHM=2.0 nm. (b) Fourier transform-limited pulse durations for the Gaussian spectrum before and after cutting-off the spectrum beyond a bandwidth of 6 nm.

On the other hand, a smaller grating aperture can be sufficient for efficient pulse compression as argued in the following. The FWHM of a typical pulse spectrum after amplification to a few hundreds of mJ is expected to be around or below 2 nm for the case of room-temperature Yb:YAG disk lasers [51,105,131–133]. When assuming a Gaussian spectral intensity distribution with a FWHM of 2 nm, 99.96 % of the optical power are contained within a cut-off bandwidth of 6 nm centered at 1030 nm, while the Fourier-limited pulse duration remains at 810 fs. Hence, the Fourier-limited pulse duration of 791 fs obtained from with a cut-off bandwidth of 7 nm is only slightly altered. This is illustrated in Figure 6.4, by comparing the Fourier transform-limited (FTL) pulse duration of a Gaussian spectrum with a FWHM of 2 nm with the FTL pulse duration of the same spectrum after cutting-off the components beyond a spectral bandwidth of 6 nm. With a cut-off bandwidth of 6 nm, the required width of the second grating is decreased according to equation 6.6:

$$D_{x,G2}^{BW=6 \text{ nm}} = (D_{x,G1/G2} + D_{x,ang.}^{BW=6 \text{ nm}}) \cdot \frac{1}{\cos(\beta'_{(\lambda_c)})} = 585 \text{ mm.} \quad 6.7$$

With a safety buffer space of ~5 %, a required grating width of 620 mm is obtained for the second compressor grating.

The height of the second grating is obtained by considering the beam spot size in the vertical direction, $D_{99\%} = 88.4 \text{ mm}$. Additionally, 15 % of buffer space and 30 mm extra space to account for the vertical offset between input and output beam and for alignment flexibility are included. This leads to a height of the second grating of 130 mm.

Experimental Implementation of the Grating Compressor

A scale model of the compressor was implemented in a CAD drawing software, as shown in Figure 6.5. With a ray tracing engine⁸, the beam propagation was simulated. For the simulation, a bandwidth of 6 nm was used, centered at a wavelength of 1030 nm. In Figure 6.5 (a) and (b) a top view and a side view of the model are shown. The central wavelength is indicated in green, while the long and short-wavelength edges of the spectrum are indicated in red and blue. To separate the output from the input beam, the end mirror is tipped by 0.45° to direct the beam pointing down by 0.9°. The resulting vertical spatial separation of output and input beam at the first grating amounts to 100 mm. This enables to pick up the output beam below the input beam using a HR mirror. By using one end mirror instead of a vertical roof mirror pair at the symmetry plane of the compressor, a small amount of spatial chirp is induced for the beam at the compressor output.

⁸ Autodesk Inventor in combination with the LambdaSpect raytracing plugin.

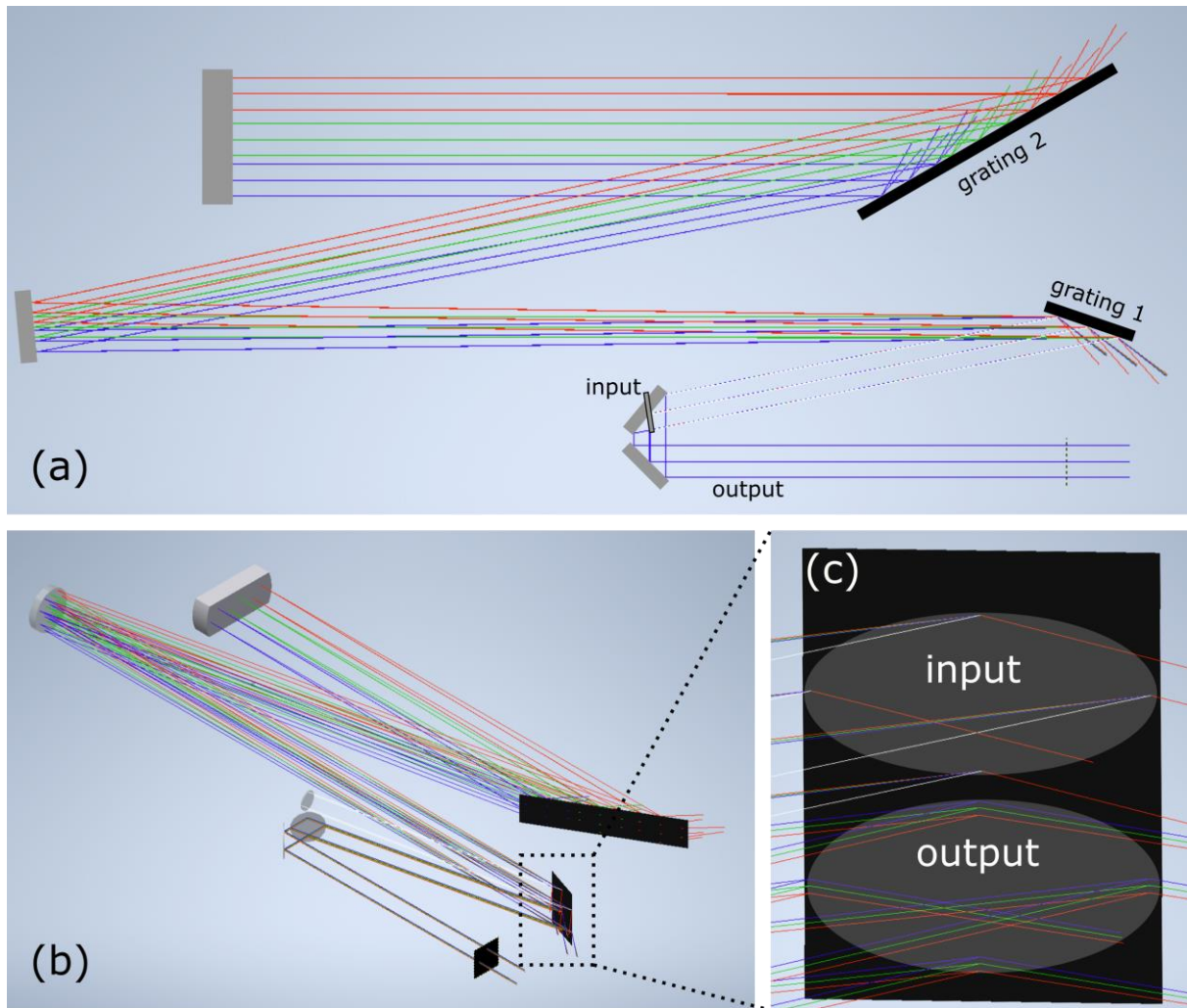


Figure 6.5: Layout of the grating compressor. (a) Top view of the compressor. Mirrors are indicated with grey blocks. (b) 3D view of the pulse compressor layout. (c) Zoom-in on the small grating. The little amount of residual spatial chirp is visible from the ray tracing at the position where the output beam is incident on the small grating.

This is due to the spectrally different optical path lengths between the compressor gratings, leading to a stronger vertical displacement for longer-wavelength spectral components. In Figure 6.5 (c) the residual spatial chirp is shown with a zoom-in on the small grating. While all spectral components of the input beam overlay at the grating, the vertical displacement is visible for the output beam, causing spatial chirp. The maximum vertical displacement for a bandwidth of 6 nm is 8.2 mm, which leads to an altered minimum pulse duration at the vertical edges of the output beam with diameter $D_{1/e^2} \approx 27$ mm [89]. Moreover, the spatially separated spectral components within the collimated beam overlay in the center of the output beam; only at the edges, the residual vertical spatial chirp alters the pulse duration and the pulse spectrum.

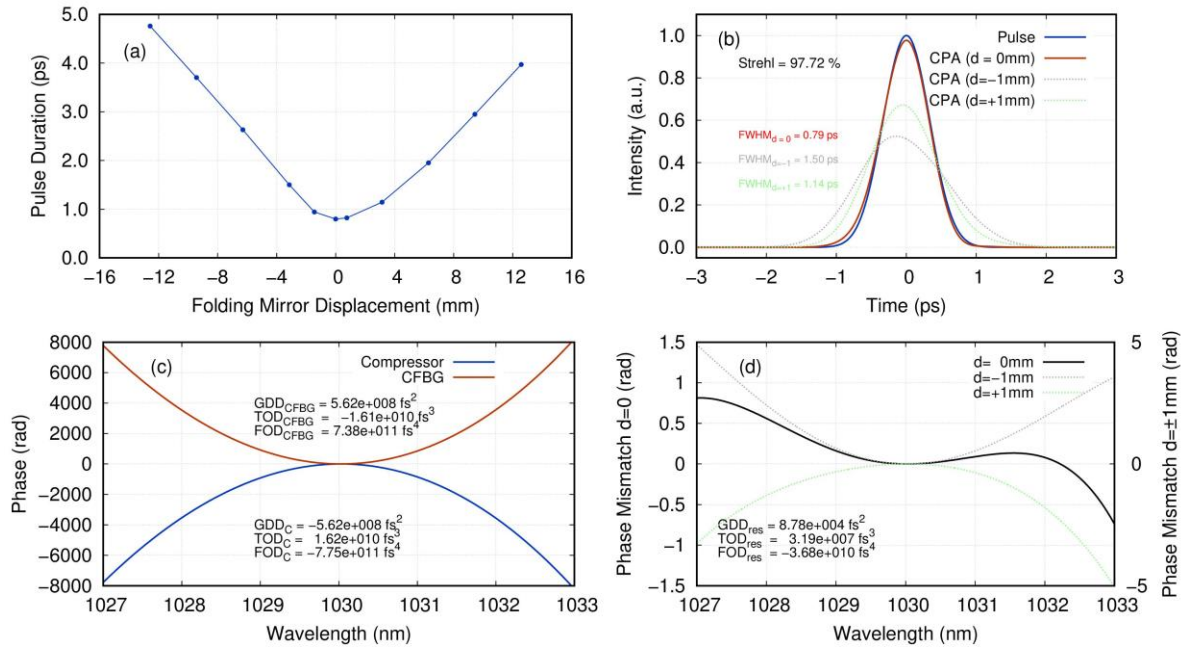


Figure 6.6: Results from the compressor ray-tracing. (a) Resultant output pulse durations (FWHM) for different linear displacement of the compressor folding mirror. (b) Output pulses after stretching and recompression for different displacements of the compressor folding mirror. (c) Spectral phases introduced to a pulse after passing through the two CFBGs and the modelled grating compressor as a function of the optical wavelength. (d) Residual spectral phase of a pulse after passing through both the CFBGs and the grating compressor. The curve is calculated by taking the sum of the data in (d).

When locally sampled, the pulse duration remains short and the spectrum remains at its full width, which is in agreement with the experiments (Figure 6.8 and Figure 6.9).

The dispersion introduced by the compressor was numerically analyzed via the optical path difference (OPD) obtained from the raytracing simulation. The compressor length b was swept in the simulation, while keeping the input angle of incidence (AOI) on the first grating fixed at the design value from the CFBGs, i.e. $AOI=60^\circ$. By converting the OPD into a temporal delay and fitting the data with a polynomial, the first three dispersion orders were obtained. The fit curve then represents the group delay, which can be converted into the spectral phase via integration over ω . In Figure 6.6 (c) the spectral phases of the CFBGs and the grating compressor are plotted. The residual spectral phase after passing both CFBG and compressor is plotted in Figure 6.6 (d). The residual values for group delay dispersion (GDD), third order dispersion (TOD), and fourth order dispersion (FOD) are indicated. The linear group delay dispersion value $GDD = -5.564 \cdot 10^{-8} \text{ fs}^2$ can be converted to the dispersion parameter D_λ via equation 2.20:

$$D_\lambda = -\frac{2\pi c}{\lambda^2} GDD = 1000.68 \frac{\text{ps}}{\text{nm}}. \quad 6.8$$

As per the layout of the CPA design, therefore the dispersion introduced by the CFBGs (see Figure 6.1) at the beginning of the CPA chain is finally compensated by the compressor dispersion, which can be seen by comparing the dispersion curves of the CFBGs and the compressor in Figure 6.6. The higher-order discrepancy between the two curves is eliminated experimentally by mutually optimizing the grating distance and the grating tilt angles. In addition, the waveshaper can be used to correct the effective discrepancy of the spectral phase of the CFBGs and the compressor. In Figure 6.6 (a) the resultant pulse durations for different positions of the folding mirror are shown. Figure 6.6 (b) shows the resultant temporal pulse shape for three different positions of the folding mirror as an example.

6.3 Compression of high-energy output pulses

Compressor alignment

For a detailed analysis of the stability and alignment sensitivity of grating compressors, as well as on compressor grating misalignment mitigation strategies, further information is given in reference [89]. In the following, a short summary of the compressor alignment procedure is given, which was followed during the setup of the compressor. To refer to the three possible rotation directions of the gratings, the chosen coordinate system is shown in Figure 6.7.

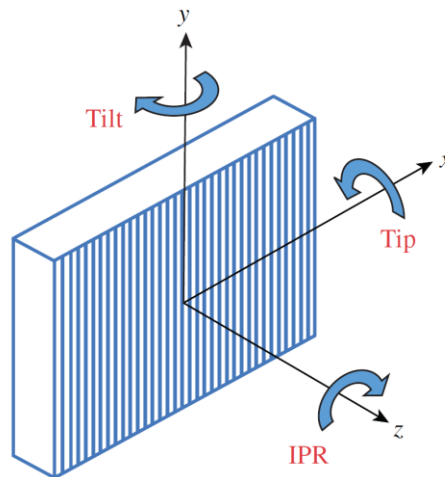


Figure 6.7: Coordinate system and convention of the rotation direction denomination. Figure taken from [89].

The following steps were undertaken for the compressor alignment procedure:

- 1) Geometrical positioning of all compressor optics according to the dimensions calculated with the CAD-model.
- 2) Definition of the position and direction of the input beam using two irises. This enables to use the compressor as a pre-aligned black box for the laser to be compressed.
- 3) Definition of the zero tip and tilt angles of incidence of the first grating. This is achieved by overlaying the zeroth-order reflection of the grating with the incident beam, eg by using a pinhole for the input beam far from the grating for enhanced angular precision.
- 4) Tilt of the first grating to the designed AOI with the precision rotation stage.
- 5) Definition of the zero in-plane rotation (IPR) angle by adjusting for horizontal propagation of the diffracted beam in the x-z-plane.
- 6) Segregation of the central wavelength component from the diffracted laser beam with a pinhole aperture close to the second grating.

- 7) Definition of the zero tip and tilt angles of the second grating by retroreflecting the central cut wavelength component. The reference aperture can be placed far from the compressor input for enhanced angular precision.
- 8) Tilt of the second grating to the calculated diffraction angle of the central wavelength component according to the grating equation (2.25).
- 9) Definition of the zero IPR angle by adjusting for horizontal propagation in the x-z-plane.
- 10) Alignment of tip and tilt of the end mirror yielding an only vertically displaced output beam that can be picked up by an HR mirror.
- 11) Elimination of the residual angular chirp stemming from non-parallel grating orientation along the x-axis, i.e. misaligned tilt. To achieve this, as described in [89], the focal spot of the output beam is monitored with a CCD camera. Any elongation of the focal spot in the x-z-plane may stem from misaligned relative tilt angles of the gratings, and can be identified by a x-z-movement in the focus when blocking certain wavelength components as aligned at the position of the end mirror, eg by using a NIR laser detector card.
- 12) Optimization of the compressor length to minimize the pulse duration. The linear translation stage used to mount the folding mirror can be used to scan the compressor length. The pulse duration is simultaneously monitored with an autocorrelator.
- 13) Optimization of the tilt angles of the compressor gratings to minimize the pulse duration. Both grating tilt angles have to be adjusted simultaneously while maintaining the output beam at a fixed position. A CCD camera can be used to monitor the output beam position. The pulse duration is simultaneously monitored with an autocorrelator.
- 14) Iteration of steps 12) and 13) until the minimum pulse duration is obtained.

Gain narrowing and minimum pulse duration

During pulse amplification, gain narrowing is a well-known phenomenon which can lead to a narrowed pulse spectrum and an increased Fourier transform-limited (FTL) pulse duration [127]. The reason for the narrowing is due to the inhomogeneous shape of the spectral emission cross section of the active laser material, leading to an inhomogeneous gain for the different spectral components of the laser pulses. In consequence, the spectrum becomes narrowed around the peak of the emission cross section.

For the developed laser system, gain narrowing of the amplified pulse spectra was identified both in the regenerative amplifier and in the multipass amplifier. The spectra of the stretched

pulses was measured with a commercial grating spectrometer at the output of the seed laser (TruMicro2000), at the output of the regenerative amplifier, and after the multipass amplifier.

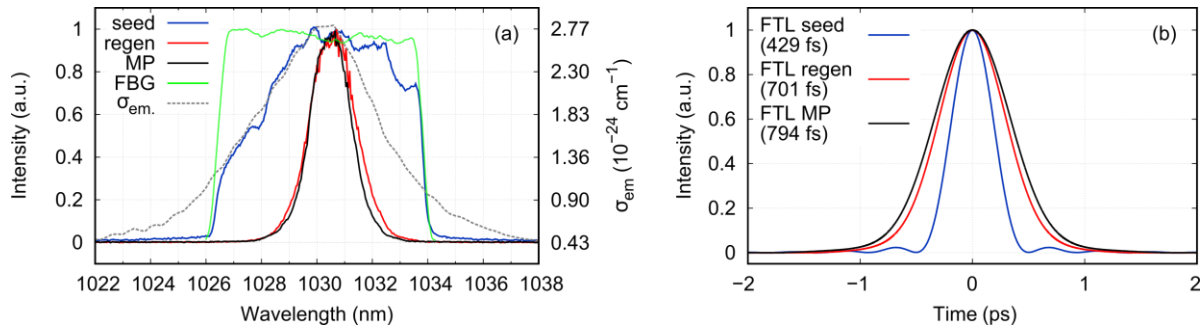


Figure 6.8: Spectral characteristics of the amplification chain. (a) The final spectrum (MP) is narrowed during the CPA process. The transmission curve of the FBG and the spectral emission cross section are included for visualization. (b) Fourier transform-limited pulse durations calculated from the spectra in (a). All data is normalized to the peak value.

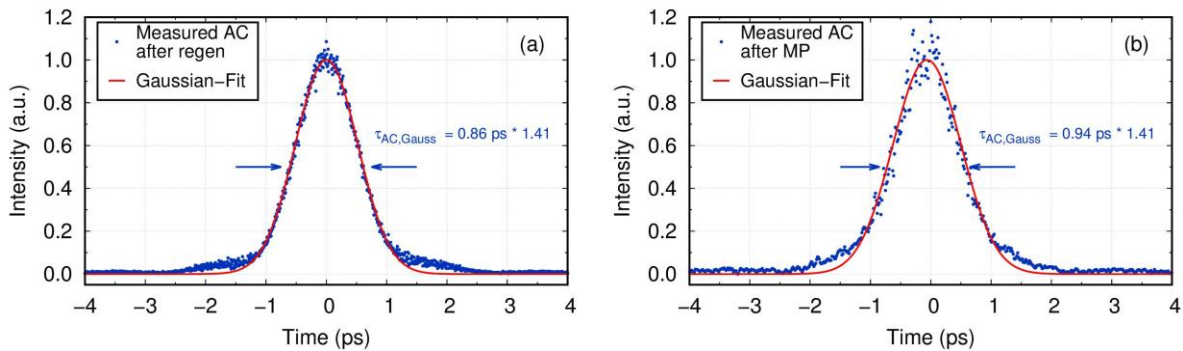


Figure 6.9: Compression of the pulses from the regen. (240 mJ before compression) and the multipass (800 mJ before compression). The data was measured using an autocorrelator and the pulse duration was determined assuming a Gaussian pulse shape. The longer pulse duration for the higher-energy pulses is attributed to stronger gain narrowing.

The measurements are shown in Figure 6.8 (a) together with the transmission spectrum of the CFBG and the spectral emission cross section of the Yb-doped active laser material. The consecutive narrowing of the spectra can be seen clearly from the data. Note that the spectrum of the seed pulses was cut at the long-wavelength side by the finite transmission window of the CFBG and the red-shifted central seed wavelength of ~ 1031.2 nm. During amplification in the regenerative amplifier and in the multipass, the central wavelength is shifted towards the peak of the emission cross section, as the corresponding spectral components are promoted by the maximum gain. Theoretically, the central wavelength of the pulse spectra is expected to converge to the peak wavelength of the emission cross section for even larger amplification factors.

In Figure 6.8 (b) the FTL pulse durations calculated from the measured spectra are shown. A pulse duration below 500 fs can still be achieved with the seed pulse spectrum even after cutting-off the long-wavelength wing. Due to the narrowed pulse spectrum after the regenerative amplifier, the calculated FTL pulse duration is increased to ~ 700 fs. After the multipass, the FTL pulse duration increases to ~ 800 fs.

Experimentally, the minimum compressed pulse durations after the regenerative amplifier and the multipass were measured with an autocorrelator, as shown in Figure 6.9. From a Gaussian curve fitted to the data, a pulse duration of 860 fs is achieved when compressing the 240-mJ pulses after the regen. A pulse duration of 940 fs is achieved for the compression of the 800-mJ pulses after the multipass. Although the calculated FTL pulse durations calculated from the pulse spectra (Figure 6.8) could not be reached, the effect of gain narrowing limiting the pulse duration is therefore still observed qualitatively.

7 Experiments

In this chapter first experimental results on filament generation performed with the developed laser system are presented. Aiming for the ultimate atmospheric application of triggering lightning at the Säntis Station in Switzerland, these preparatory experiments show that the controlled generation of filaments is possible not only on a small laboratory scale, but also on a long-range scale in the ~ 100 m range. Parts of these results were published in [134].

7.1 HV Discharge Triggering

Laboratory experiments on high-voltage discharge triggering and guiding were performed in the laboratory of TRUMPF Scientific Lasers GmbH & Co.KG using the compressed output of the regenerative amplifier of the LLR laser system. Details on the measurements and the results of the experiments can be found in [134]. An important result is shown in Figure 7.1. When increasing the laser pulse energy, the breakdown voltage for a triggered discharge between the HV electrodes first decreases and then reaches a plateau, which is due to the saturation of the filament density between the HV electrodes. In this regime, filamentation starts already before the first electrode, which is not captured by the measurement setup. If the laser energy is partially converted to the second and third harmonic, the reduction of the breakdown voltage takes place already at lower initial laser pulse energy. This means that the filaments generated by pulses with shorter wavelength are more efficient to trigger and guide HV discharges compared to the longer-wavelength infrared laser wavelength.

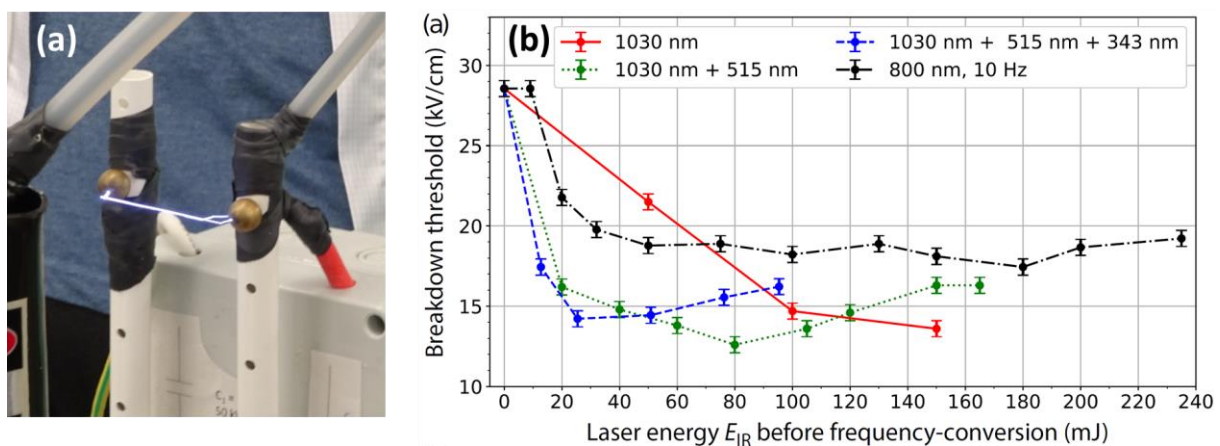


Figure 7.1: HV discharge triggering in the laboratory. Photograph of a triggered and guided HV discharge between two spherical electrodes. (b) Breakdown voltage between the electrodes for different wavelength compositions as a function of the laser pulse energy. Figure adapted from [134].

Importantly, the conversion of parts of the laser energy to the second or third harmonic results in a net-benefit for the efficiency in triggering HV discharges, where the energy loss due to the limited conversion efficiency is overcompensated by the shorter wavelength. As a consequence, the implementation of a second-harmonic or third-harmonic nonlinear optical crystal may provide an additional tool for the campaign aimed at triggering atmospheric discharges.

7.2 Short Range Filament Generation

To test filament generation, an experiment was performed in the laboratory of TRUMPF Scientific Lasers GmbH & Co.KG on a few-meters scale. To generate the filaments, the compressed output laser beam was focused using a concave mirror with a 12-m radius of curvature, i.e. a focal length of 6 m. With a beam diameter of approximately 30 mm, the expected distance until beam collapse $L_{c,f}$ can be calculated according equations 2.62 and 2.63 using the given beam waist radius (~ 14 mm), pulse energy (~ 580 mJ), and pulse duration (~ 1 ps) [11]. It amounts to $L_{c,f}^{theory} = 4.72$ m when neglecting the propagation distance before the focusing element. In the experiment, an additional distance between grating and focusing mirror was realized as shown in Figure 7.2 due to space constraints in the laboratory. Filament generation was performed as a function of the output pulse energy up to 580 mJ, while the onset of the filament was observed via the characteristic emission due to plasma recombination lines of nitrogen in the air, as shown in Figure 7.3. [135]. The onset of the filament (filamentation length, $L_{c,f}$) as a function of the input pulse energy is [plotted in Figure 7.4. At small pulse energies, theoretical ($L_{c,f}^{theory}$) and experimental ($L_{c,f}^{experiment}$) filamentation lengths closely coincide. However, at high output pulse energies, the discrepancy significantly increases. While $L_{c,f}^{experiment}$ shifts by 3.61 m towards the laser aperture, $L_{c,f}^{theory}$ moves only by 1.08 m. Note that equation 2.62 describes the filamentation distance accurately only for Townes-beam profiles at input powers up to $100 \cdot P_{crit}$ in purely Kerr-nonlinear media. Moreover, spatial beam profile perturbations are not captured by the equation, which tend to result in earlier beam collapse due to spatial modulational instabilities [11]. The discrepancy between $L_{c,f}^{theory}$ and $L_{c,f}^{experiment}$ may be therefore partially be due to these modelling inaccuracies. Moreover, the prediction of $L_{c,f}^{theory}$ for high-energy pulses is incomplete regarding this experiment, as the additional ~ 2 -m pulse propagation distance of the fully compressed pulses between the last compressor grating and the focusing mirror is not taken into account. At small pulse energies, the 2-m pulse propagation takes place in a more linear regime, resulting in a more accurate agreement between theory and experiment.

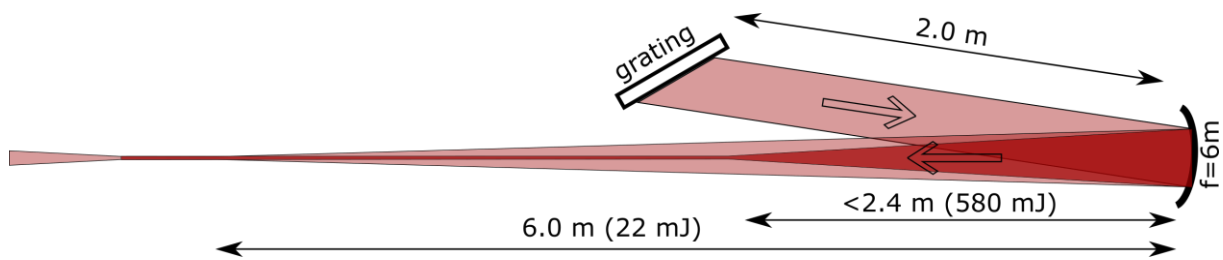


Figure 7.2: Schematic sketch of short-range filamentation experiments in the laboratory.



Figure 7.3 Filament generation at different output pulse energies. The arrows indicate the starting point of the visible part of the laser filaments.

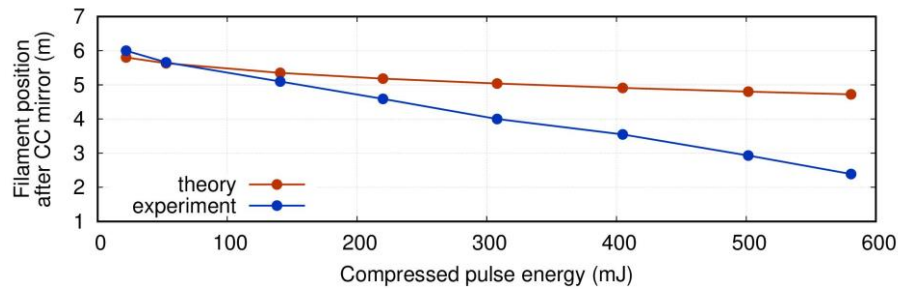


Figure 7.4: Theoretical and experimental filamentation length measured from the $f=6\text{m}$ concave mirror as a function of the output pulse energy.

7.3 Long-Range Filament Generation

In a further experimental campaign, the developed laser system was installed at the end of the hall of a former linear accelerator facility at Orsay, France⁹. This site offers up to 140 m of linear horizontal indoor distance where the laser beam can propagate and be examined during experimental studies. To investigate on the maximum filament length which can be achieved with the laser system, a first experiment was performed using the full laser output power of 720 W, i.e. with 720 mJ pulse energy. The collimated output beam was sent along the $\sim 140\text{-m}$ hallway and filamentation was tested. Due to LIDT constraints of the transfer mirrors after the laser output aperture, a linear chirp of $D_2 = 4 \text{ ps/nm}$ was applied to the stretched seed pulses using the waveshaper (see Figure 6.2). This amount of chirp remains after the compressor, as the latter was optimized for no additional waveshaper dispersion.

Generally, in experiments using broadband femtosecond pulses, the direction of chirp is sometimes chosen such as to compensate for the positive GVD of the air during long-range propagation [11,14,94]. Beam collapse is then retarded due to the reduced peak power associated with the longer pulse duration, while the initial peak power associated with the original pulse duration is still attained after some propagation through the air due to the nonlinear effect of self-steepening. However, for this experiment the GDD contribution of the air during approximately 200 m of propagation only amounts to $GDD_{air} = GVD_{air} * d = -3.55 \cdot 10^{-5} \frac{\text{ps}}{\text{nm}\cdot\text{m}} \cdot 200 \text{ m} = 4.97 \cdot 10^{-3} \frac{\text{ps}}{\text{nm}}$ [136], which is negligible compared to the GDD applied by the waveshaper.

Photographs of long-range filamentation experiments using the propagation of the collimated output beam are shown in Figure 7.5. Here, filamentation was observed over a length of $>70 \text{ m}$ when using the full output power. A concrete wall was used as a beam blocker at a distance

⁹ Laboratoire de l'accélérateur linéaire (LAL), Université Paris-Saclay (<https://www.lal.in2p3.fr/en/>)

of approximately 140 m. The conically emitted white-light (supercontinuum) generated during the propagation was caught at the concrete wall, as shown in the inset of Figure 7.5 (b). With low ambient illumination, the plasma luminescence could be seen along the filamentation zone. In addition, an LBO crystal was used to frequency-double the infrared light. This can be used as a sophisticated scheme to trigger high-voltage breakdown, as described in [134].

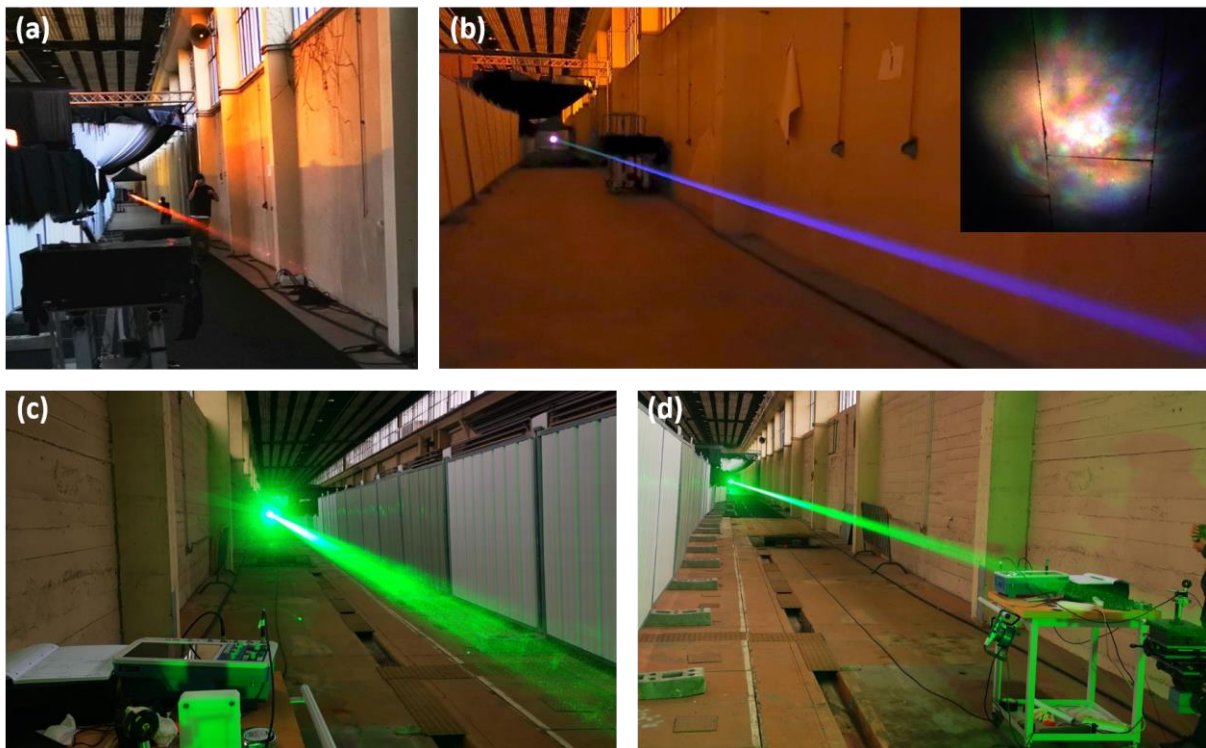


Figure 7.5: Long-range filament generation with the developed laser system. (a,b) Filaments generated by the collimated output beam of the laser. In the inset of (b) the white-light generated in the filament is shown as visualized on the beam blocker. (c,d) Filaments generated by the collimated and partially frequency-doubled output beam. Photographs provided by courtesy of Pierre Walch, ENSTA ParisTech.

In this experiment, the visible green light was visible along the entire beam propagation due to Mie scattering of the green light on dust particles in the air. Photographs of the SHG filamentation experiments are shown in Figure 7.5 (c) and (d).

The experimental evidence for filament generation can be based on the impact on photographic paper when illuminated by the laser beam. The darkening of the paper is dependent on the optical intensity, which reveals the small-diameter filaments as small-diameter burned spots within the larger area darkened by the laser beam profile. Moreover, a streak image of the temporal pulse train is captured on the photographic paper when moving the paper quickly through the 1-kHz pulsed laser beam. Two examples of detected filaments

are shown in Figure 7.6. In (a) the evidence of a multi-filamentation region is shown, which leads to a disordered ensemble of simultaneous impacts. In (b) the evidence of a region with single filamentation is shown. Here, the temporal pulse separation within the pulse train (1 ms) is mapped to a spatial train of impacts on the photographic paper. More information and results were published in [137].

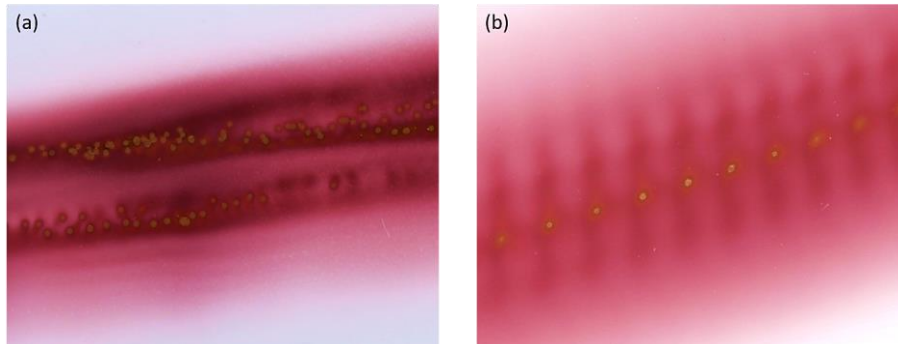


Figure 7.6: Filament detection with photographic paper. The paper is moved through the filamentation zone transversely in the direction from the top right to the bottom left. (a) Multiple filamentation is indicated by a distribution of several burned spots. (b) At the beginning of the filamentation zone, single filaments are present, leading to a series of impacts on the photographic paper mapping the laser repetition rate. Photographs provided by courtesy of Pierre Walch, ENSTA ParisTech.

For further experimental studies within the Laser Lightning Rod project, a telescope will be used to expand the output beam by a factor 7. This will retard the onset of filamentation according to equation 2.62, which will be important for the vertical lightning campaign, aiming at the initiation of lightning strikes to and from a conductive tower. Here, the onset of filamentation must be retarded at least by the height of the tower, i.e. approximately 120 m for the Sântis station. Detailed information on the experimental strategy, the underlying physics, and the frame of the project can be found in reference [64].



Figure 7.7: Beam expanding telescope for remote filament generation. A magnification factor 7 is implemented in an off-axis Dall-Kirkham Cassegrain configuration. The telescope is conceived and realized by the Université de Geneve. Picture provided by courtesy of Thomas Produit, GAP, Université de Geneve.

8 Summary and Outlook

Summary

In this thesis, the development of an ultrafast laser system specialized for the application in atmospheric research on a laser lightning rod was presented. Industrial-grade thin-disk technology was employed as base technology for the development of a multi-stage picosecond CPA system with unprecedented laser output parameters. A regenerative amplifier based on the Dira-200-1 series serves as the first power amplifier, seeded by an industrial-grade fiber laser (TRUMPF TruMicro2000). The stretched 240-mJ output pulses of the regenerative amplifier are used to seed a multipass amplifier serving as the main amplifier. Here, a pulse energy of 800 mJ is attained. After the pulse compression in a grating compressor, a pulse energy of 720 mJ remains at a pulse duration of 920 fs (FWHM). All amplifiers are operated at a repetition rate of 1 kHz. For the high-power amplifiers, Yb:LuAG serves as active medium, providing a low quantum defect and high thermal conductivity enabling high pump and average output power. The laser system was developed in the frame of the FET-open project *Laser Lightning Rod*, addressing a novel approach for lightning protection based on laser filamentation.

The **thin-disk regenerative amplifier** was implemented in a ring resonator configuration. A pump power of up to 4 kW is available from the pump laser diodes at a wavelength of 940 nm. Pulse coupling is realized using a BBO-based Pockels cell. At the output, pulse energies of 240 mJ are obtained with an optical-to-optical power efficiency of 25 %. As expected from a thin-disk regenerative amplifier, an excellent beam quality with an $M^2 < 1.2$ is conserved. The amplifier is energy-stabilized via active pump power modulation, and intra-cavity pointing stabilized via piezo-controlled cavity mirrors. Long-term stability was demonstrated over more than 13 hours continuous operation at the full energy.

A **study of energy storage and ASE** in three different thin-disk geometries was performed to test their applicability for the multipass amplifier. Depending on the repetition rate of the amplifier, the most suitable thin-disk could be identified for each one. To study the occurrence of ASE in the thin-disks, a technique was implemented that allowed to probe the instantaneous gain and hence the instantaneous inversion and stored energy during and after the pump process. The measurements revealed that ASE is the limiting mechanism for the energy storage and hence the amplification in the thin-disks employed for the multipass amplifier. The results provide a guideline on the maximum useful pump energy to be delivered per pulse.

For the development of the **thin-disk multipass amplifier** with the chosen thin-disk geometry, three experimental setups were conceived. Up to 12 disk passes were aligned each time, while the beam propagated near-collimated, assisted by adequate curved mirrors. The first setup

included 1 thin-disk laser head with a peak pump power of up to 10 kW. Here a typical pulse energy of 490 mJ was achieved with a homogeneous output beam profile. Higher pulse energy up to 593 mJ was demonstrated with an alignment optimized for maximum energy extraction from the thin-disk, however, with a strongly distorted spatial output mode. As a conclusion, it was found that by maintaining the beam diameter as small as possible on the laser disk, the optimum spatial mode shape is obtained. With the second setup including two thin-disk laser heads, a pulse energy up to 785 mJ was obtained with a homogeneous output mode. In this configuration, gain saturation was observed with a high number of amplification passes, limiting the maximum output pulse energy. Finally, an experimental setup using four thin-disk laser heads was used, leading to a maximum pulse energy of 863 mJ. At this point of operation, the damage threshold of the disk limited further pulse amplification, as a small beam diameter was necessary to maintain a smooth spatial output mode.

For the **CPA design** of the laser system, a **chirped fiber Bragg grating** in combination with a Treacy-type **grating compressor** were used. In addition, a **waveshaper** was included to fine-tune the remaining spectral phase mismatch after manual compressor alignment. Spectral amplitude pre-shaping to counteract gain narrowing in the regenerative amplifier was demonstrated. Furthermore, additional dispersion can be introduced by the waveshaper to adjust the compressed pulse duration for experimental applications. After compression, a pulse duration of 920 fs was measured at full output power. The pulse energy remained at 720 mJ due to the limited diffraction efficiency of the gratings.

First experiments were performed with the compressed output pulses of the regenerative amplifier in the framework of the Laser Lightning Rod project. High-voltage discharges were triggered by **dual and triple-frequency laser filaments** with a breakdown voltage significantly reduced compared to the fundamental-frequency case.

The completed laser system has been deployed, commissioned and used for horizontal experiments on **remote and long-range filament generation** at LAL, Orsay. A filamentation zone over >70 m was measured. The onset of filamentation could be retarded beyond 120 m via temporal and spatial pulse expansion. An experimental outdoor campaign at the summit of Mt. Säntis, CH, is planned for the lightning-active season in summer 2021.

Outlook

In the future, several steps may be feasible to further optimize the performance of laser systems comparable to the one at hand. To finally traverse the Joule milestone, a key parameter is the **seed pulse energy** provided by the regenerative amplifier in this case. Recently, pulse energies above 500 mJ at 1 kHz repetition rate have been achieved from a similar regenerative amplifier using two thin-disk laser heads that was developed by TRUMPF Scientific Lasers GmbH & Co. KG [138]. With such high seed pulse energy, energy extraction from the multipass thin-disks will be much more efficient, and less disk passes will be necessary to attain the same output energy, i.e. to achieve a cumulated seed fluence on the order of the saturation fluence¹⁰. This approach will also allow for a better beam quality as wavefront distortions induced for each pass through the thin-disk are reduced.

Another possibility to achieve higher output pulse energy is to utilize **thin-disks with a bonded undoped anti-ASE cap**. This approach has been proposed, analyzed and tested by several research groups [59,60,80,139–144]. With such optimized thin disks, much higher inversion levels can be achieved, increasing the single pass gain for the signal and the amount of stored energy per disk. As a consequence, higher pulse energy can be achieved with an equal number of disk passes. However, the development, optimization and the procurement of these specialized disks is time consuming and costly and will require some dedicated effort and capacity.

Finally, technological progress regarding the **heat sinks** is ongoing (stiffer substrates, improved disk cooling technology) which will directly reduce the thermo-mechanical deformation of the pumped thin-disks. Beam quality, gain via reduced lower level thermal population, and amplifier alignment will benefit from such next-generation technology.

The **pulse duration** may in the future be decreased by **pre-shaping the spectral intensity** of the seed laser to compensate for the gain narrowing occurring during high-power amplification in the regenerative and multipass amplifiers. Recently, a pulse duration below 500 fs was achieved at a pulse energy of 206 mJ with a similar regenerative amplifier by using this method [50]. For the LLR laser system, the spectral bandwidth and hence the pulse duration will eventually be limited by the hard aperture of the currently employed second compressor grating rather than the spectral bandwidth of the high-energy pulses.

Joule-class kilohertz laser systems with ultrashort pulse duration are facing a broad spectrum of **novel applications**. In the near future, the developed laser system will enable atmospheric

¹⁰ As illustrated in Table 5.1, the first 4 to 5 passes in the multipass amplifier were required to reach the 400 mJ-level when seeded with 240 mJ.

research on the laser lightning rod in an experimental campaign at Mt. Säntis. The outcome will potentially have a major impact on lightning protection, if experiments are successful. Other fields of research and technology will equivalently benefit from the achieved laser parameters. Besides the more classical use in OPCPA pumping and attosecond time-resolved measurements via high-harmonic generation, the driving of **secondary radiation sources** has emerged as a growing field of application. X-ray and EUV generation via plasma generation or by inverse Compton scattering off electrons, and Terahertz generation are among them. Furthermore, **electron acceleration** will be tangible with high-energy femtosecond pulses obtained by nonlinear post-compression schemes based on spectral broadening in gas-filled Herriott-type multipass cells [145–149].

9 Bibliography

1. T. H. Maiman, "Stimulated Optical Radiation in Ruby," *Nature* **187**, 493–494 (1960).
2. A. Thoss, "50 Jahre Laser - und wie weiter?," *LTJ* **7** (2010).
3. J. Hecht, "The First Half-Century of Laser Development," *LTJ* **7**, 20–25 (2010).
4. W. Koechner and M. Bass, *Solid-State Lasers. A Graduate Text* (Springer-Verlag New York Inc, 2003).
5. M. J. Weber, *Handbook of laser wavelengths* (CRC Press, 1999).
6. D. Strickland and G. Mourou, "Compression of amplified chirped optical pulses," *Optics Communications* **55**, 447–449 (1985).
7. C. N. Danson, C. Haefner, J. Bromage, T. Butcher, J.-C. F. Chanteloup, E. A. Chowdhury, A. Galvanauskas, L. A. Gizzi, J. Hein, D. I. Hillier, N. W. Hopps, Y. Kato, E. A. Khazanov, R. Kodama, G. Korn, R. Li, Y. Li, J. Limpert, J. Ma, C. H. Nam, D. Neely, D. Papadopoulos, R. R. Penman, L. Qian, J. J. Rocca, A. A. Shaykin, C. W. Siders, C. Spindloe, S. Szatmári, R. M. G. M. Trines, J. Zhu, P. Zhu, and J. D. Zuegel, "Petawatt and exawatt class lasers worldwide," *High Pow Laser Sci Eng* **7**, 255 (2019).
8. The Nobel Prize in Physics 2018. NobelPrize.org. Nobel Prize Outreach AB 2021. <https://www.nobelprize.org/prizes/physics/2018/summary> (2018).
9. The Nobel Committee for Physics, Scientific Background on the Nobel Prize in Physics 2018. Groundbreaking Interventions in Laser Physics. www.nobelprize.org, 2018.
10. A. Braun, G. Korn, X. Liu, Du D, J. Squier, and G. Mourou, "Self-channeling of high-peak-power femtosecond laser pulses in air," *Opt. Lett.* **20**, 73–75 (ts).
11. A. Couairon and A. Mysyrowicz, "Femtosecond filamentation in transparent media," *Physics Reports* **441**, 47–189 (2007).
12. L. Bergé, S. Skupin, R. Nuter, J. Kasparian, and J.-P. Wolf, "Ultrashort filaments of light in weakly ionized, optically transparent media," *Rep. Prog. Phys.* **71**, 109801 (2008).
13. J. Kasparian and J.-P. Wolf, "Physics and applications of atmospheric nonlinear optics and filamentation," *Optics express* **16**, 466–493 (2008).
14. J. P. Wolf, "Short-pulse lasers for weather control," *Reports on Progress in Physics* **81**, 26001 (2017).
15. G. Schimmel, T. Produit, D. Mongin, J. Kasparian, and J.-P. Wolf, "Free space laser telecommunication through fog," *Optica* **5**, 1338 (2018).
16. A. Hening, D. Wayne, M. Lovern, and M. Lasher, "Applications of laser-induced filaments for optical communication links," in *Laser Communication and Propagation through the Atmosphere and Oceans III* (SPIE, 2014), pp. 163–170.

17. L. de La Cruz, E. Schubert, D. Mongin, S. Klingebiel, M. Schultze, T. Metzger, K. Michel, J. Kasparian, and J.-P. Wolf, "High repetition rate ultrashort laser cuts a path through fog," *Appl. Phys. Lett.* **109**, 251105 (2016).
18. P. Rohwetter, J. Kasparian, K. Stelmaszczyk, Z. Hao, S. Henin, N. Lascoux, W. M. Nakaema, Y. Petit, M. Queißer, R. Salamé, E. Salmon, L. Wöste, and J.-P. Wolf, "Laser-induced water condensation in air," *Nature Photon* **4**, 451–456 (2010).
19. S. Henin, Y. Petit, P. Rohwetter, K. Stelmaszczyk, Z. Q. Hao, W. M. Nakaema, A. Vogel, T. Pohl, F. Schneider, J. Kasparian, K. Weber, L. Wöste, and J.-P. Wolf, "Field measurements suggest the mechanism of laser-assisted water condensation,"
20. Y. Liu, H. Sun, J. Liu, H. Liang, J. Ju, T. Wang, Y. Tian, C. Wang, Y. Liu, S. L. Chin, and R. Li, "Laser-filamentation-induced water condensation and snow formation in a cloud chamber filled with different ambient gases," *Optics express* **24**, 7364–7373 (2016).
21. J. Kasparian, M. Rodriguez, G. Méjean, J. Yu, E. Salmon, H. Wille, R. Bourayou, S. Frey, Y. B. Andre, A. Mysyrowicz, R. Sauerbrey, J. P. Wolf, and L. Wöste, "White-light filaments for atmospheric analysis," *Science* **301**, 61–64 (2003).
22. Q. Luo, H. L. Xu, S. A. Hosseini, J.-F. Daigle, F. Théberge, M. Sharifi, and S. L. Chin, "Remote sensing of pollutants using femtosecond laser pulse fluorescence spectroscopy," *Appl. Phys. B* **82**, 105–109 (2006).
23. G. Mjean, J. Kasparian, J. Yu, S. Frey, E. Salmon, and J.-P. Wolf, "Remote detection and identification of biological aerosols using a femtosecond terawatt lidar system," *Appl. Phys. B* **78**, 535–537 (2004).
24. J.-C. Diels and X. M. Zhao, Discharge of Lightning With Ultrashort Laser Pulses, US Patent No. 5175664 (1992) .
25. S. Tzortzakis, B. Prade, M. Franco, A. Mysyrowicz, S. Hüller, and P. Mora, "Femtosecond laser-guided electric discharge in air," *Physical review. E, Statistical, nonlinear, and soft matter physics* **64**, 57401 (2001).
26. X. M. Zhao, J.-C. Diels, C. Y. Wang, and J. M. Elizondo, "Femtosecond ultraviolet laser pulse induced lightning discharges in gases," *IEEE J. Quantum Electron.* **31**, 599–612 (1995).
27. P. Rambo, J. Biegert, V. Kubecek, J. Schwarz, A. Bernstein, J.-C. Diels, R. Bernstein, and K. Stahlkopf, "Laboratory tests of laser-induced lightning discharge," *J. Opt. Technol.* **66**, 194 (1999).
28. B. Forestier, A. Houard, I. Revel, M. Durand, Y. B. André, B. Prade, A. Jarnac, J. Carbonnel, M. Le Nevé, J. C. de Miscault, B. Esmiller, D. Chapuis, and A. Mysyrowicz, "Triggering, guiding and deviation of long air spark discharges with femtosecond laser filament," *AIP Advances* **2**, 12151 (2012).

29. M. Durand, A. Houard, B. Prade, A. Mysyrowicz, A. Durécu, B. Moreau, D. Fleury, O. Vasseur, H. Borchert, K. Diener, R. Schmitt, F. Théberge, M. Chateauneuf, J.-F. Daigle, and J. Dubois, "Kilometer range filamentation," *Optics express* **21**, 26836–26845 (2013).
30. S. Uchida, Y. Shimada, H. Yasuda, S. Motokoshi, C. Yamanaka, T. Yamanaka, Z.-i. Kawasaki, and K. Tsubakimoto, "Laser-triggered lightning in field experiments," *J. Opt. Technol.* **66**, 199 (1999).
31. J. Kasparian, R. Ackermann, Y.-B. André, G. Méchain, G. Méjean, B. Prade, P. Rohwetter, E. Salmon, K. Stelmaszczyk, J. Yu, A. Mysyrowicz, R. Sauerbrey, L. Wöste, and J.-P. Wolf, "Electric events synchronized with laser filaments in thunderclouds," *Optics express* **16**, 5757–5763 (2008).
32. A. Houard, V. Jukna, G. Point, Y.-B. André, S. Klingebiel, M. Schultze, K. Michel, T. Metzger, and A. Mysyrowicz, "Study of filamentation with a high power high repetition rate ps laser at 1.03 μm ," *Optics express* **24**, 7437–7448 (2016).
33. E. Schubert, L. de La Cruz, D. Mongin, S. Klingebiel, M. Schultze, T. Metzger, K. Michel, J. Kasparian, and J.-P. Wolf, "Dual-scale turbulence in filamenting laser beams at high average power," *Phys. Rev. A* **94** (2016).
34. G. Point, C. Milián, A. Couairon, A. Mysyrowicz, and A. Houard, "Generation of long-lived underdense channels using femtosecond filamentation in air," *Journal of Physics B: Atomic, Molecular and Optical Physics* **48**, 94009 (2015).
35. F. Paschen, "Ueber die zum Funkenübergang in Luft, Wasserstoff und Kohlensäure bei verschiedenen Drucken erforderliche Potentialdifferenz," *Ann. Phys. Chem.* **273**, 69–96 (1889).
36. C. J. Saraceno, D. Sutter, T. Metzger, and M. Abdou Ahmed, "The amazing progress of high-power ultrafast thin-disk lasers," *J. Eur. Opt. Soc.-Rapid Publ.* **15**, 4169 (2019).
37. S.-S. Schad, V. Kuhn, T. Gottwald, V. Negoita, A. Killi, and K. Wallmeroth, "Near fundamental mode high-power thin-disk laser," *Proc. SPIE 8959, Solid State Lasers XXIII: Technology and Devices*, 89590U (28 February 2014).
38. "Data Sheet TRUMPF TruDisk," https://www.trumpf.com/no_cache/en_US/products/laser/disk-lasers/trudisk/product_data_sheet/download/TRUMPF-technical-data-sheet-TruDisk.pdf.
39. "Datasheet IPG YLS-U Series," <https://www.ipgphotonics.com/en/202/FileAttachment/YLS-U+Series+Datasheet.pdf>.
40. P. Russbuedt, T. Mans, J. Weitenberg, H. D. Hoffmann, and R. Poprawe, "Compact diode-pumped 1.1 kW Yb:YAG Innoslab femtosecond amplifier," *Optics letters* **35**, 4169–4171 (2010).
41. "Data Sheet ActiveFiberSystems Ytterbium-2000," https://www.afs-jena.de/images/Flyer_Ytterbium-300-2000.pdf.

42. A. Giesen, H. Hügel, A. Voss, K. Wittig, U. Brauch, and H. Opower, "Scalable concept for diode-pumped high-power solid-state lasers," *Appl. Phys. B* **58**, 365–372 (1994).
43. M. Müller, C. Aleshire, A. Klenke, E. Haddad, F. Légaré, A. Tünnermann, and J. Limpert, "10.4 kW coherently combined ultrafast fiber laser," *Optics letters* **45**, 3083–3086 (2020).
44. T. Dietz, M. Jenne, D. Bauer, M. Scharun, D. Sutter, and A. Killi, "Ultrafast thin-disk multipass amplifier system providing 19 kW of average output power and pulse energies in the 10 mJ range at 1 ps of pulse duration for glass-cleaving applications," *Opt. Express* **28**, 11415 (2020).
45. J.-P. Negel, A. Loescher, D. Bauer, D. Sutter, A. Killi, M. A. Ahmed, and T. Graf, "Second Generation Thin-Disk Multipass Amplifier Delivering Picosecond Pulses with 2 kW of Average Output Power," in *Lasers Congress 2016 (ASSL, LSC, LAC)* (Optical Society of America, 2016), ATu4A.5.
46. P. Russbueldt, T. Mans, G. Rotarius, J. Weitenberg, H. D. Hoffmann, and R. Poprawe, "400W Yb:YAG Innoslab fs-Amplifier," *Optics express* **17**, 12230–12245 (2009).
47. E. Papastathopoulos, F. Baumann, O. Bocksrocker, T. Gottwald, A. Killi, B. Metzger, S. S. Schad, N. Speker, T. Ryba, and S. Zaske, "High-power high-brightness disk lasers for advanced applications," *Proc. SPIE 11664, Solid State Lasers XXX: Technology and Devices*, 116640M (5 March 2021).
48. S. Nagel, B. Metzger, T. Gottwald, V. Kuhn, A. Killi, and S.-S. Schad, "Thin Disk Laser Operating in Fundamental Mode up to a Power of 4kW," 1.
49. C. Y. Teisset, C. Wandt, M. Schultze, S. Klingebiel, M. Häfner, S. Prinz, S. Stark, C. Grebing, J.-P. Negel, H. Höck, M. Scharun, T. Dietz, D. Bauer, A. Budnicki, C. Stolzenburg, D. Sutter, A. Killi, and T. Metzger, "Multi-kW Thin-Disk Amplifiers," in *High-Brightness Sources and Light-driven Interactions* (Optical Society of America, 2018), HT1A.6.
50. C. Wandt, C. Herkommer, R. Jung, S. Klingebiel, P. Krötz, M. Rampp, C. Y. Teisset, K. Michel, and T. Metzger, "Ultrafast Thin-Disk based CPA System with >.1kW Output Power and <.500 fs Pulse Duration," in *The 22nd International Conference on Ultrafast Phenomena 2020* (Optical Society of America, 2020), W2A.2.
51. T. Nubbemeyer, M. Kaumanns, M. Ueffing, M. Gorjan, A. Alismail, H. Fattahi, J. Brons, O. Pronin, H. G. Barros, Z. Major, T. Metzger, D. Sutter, and F. Krausz, "1 kW, 200 mJ picosecond thin-disk laser system," *Opt. Lett.* **42**, 1381–1384 (2017).
52. C. Wandt, S. Klingebiel, M. Schultze, S. Prinz, C. Y. Teisset, S. Stark, C. Grebing, M. Häfner, R. Bessing, T. Herzig, A. Budnicki, D. Sutter, K. Michel, T. Nubbemeyer, F. Krausz, and T. Metzger, "1 kW Ultrafast Thin-Disk Amplifier System," in *Conference on Lasers and Electro-Optics* (Optical Society of America, 2017), STh1L.1.

53. M. Schulz, H. Hoepfner, M. Temme, R. Riedel, B. Faatz, M. J. Prandolini, M. Drescher, and F. Tavella, "kilowatt burst average power from 2-stage cascaded Yb:YAG thin-disk multipass amplifier," in *Frontiers in Optics 2013* (Optical Society of America, 2013), FTu4A.2.
54. J. M. Smith, S. Banerjee, P. D. Mason, K. Ertel, T. J. Butcher, P. J. Phillips, M. D. Vido, O. Chekhlov, M. Divoky, J. Pilar, W. Shaikh, C. Hooker, A. Lucianetti, C. H. Gomez, T. Mocek, C. Edwards, and J. L. Collier, "Energy Scaling Nanosecond Pulsed Yb:YAG Cryo-cooled DPSSL Amplifier Technology to 100J-level," in *Lasers Congress 2016 (ASSL, LSC, LAC)* (Optical Society of America, 2016), ATh4A.2.
55. T. Gonçalves-Novo, D. Albach, B. Vincent, M. Arzakantsyan, and J.-C. Chanteloup, "14 J / 2 Hz Yb³⁺:YAG diode pumped solid state laser chain," *Opt. Express* **21**, 855–866 (2013).
56. C. Wandt, S. Klingebiel, S. Keppler, M. Hornung, M. Loeser, M. Siebold, C. Skrobol, A. Kessel, S. A. Trushin, Z. Major, J. Hein, M. C. Kaluza, F. Krausz, and S. Karsch, "Development of a Joule-class Yb. YAG amplifier and its implementation in a CPA system generating 1 TW pulses," *Laser & Photonics Reviews* **8**, 875–881 (2014).
57. P. Mason, M. Divoký, K. Ertel, J. Pilař, T. Butcher, M. Hanuš, S. Banerjee, J. Phillips, J. Smith, M. de Vido, A. Lucianetti, C. Hernandez-Gomez, C. Edwards, T. Mocek, and J. Collier, "Kilowatt average power 100 J-level diode pumped solid state laser," *Optica* **4**, 438 (2017).
58. R. Jung, J. Tümmler, T. Nubbemeyer, and I. Will, "Two-Channel Thin-Disk Laser for High Pulse Energy," in *Advanced Solid State Lasers* (Optical Society of America, 2015), AW3A.7.
59. M. Pergament, L. E. Zapata, U. Demirbas, Y. Liu, M. Kellert, S. Reuter, J. Thesinga, Y. Hua, H. Cankaya, A.-L. Calendron, and F. X. Kärtner, "High Energy Cryogenic Yb:YAG and Yb:YLF Chirped Pulse Amplifiers," in *Laser Congress 2020 (ASSL, LAC)* (Optical Society of America, 2020), ATu4A.3.
60. Y. Wang, H. Chi, C. Baumgarten, K. Dehne, A. R. Meadows, A. Davenport, G. Murray, B. A. Reagan, C. S. Menoni, and J. J. Rocca, "1.1 J Yb:YAG picosecond laser at 1 kHz repetition rate," *Opt. Lett.* **45**, 6615–6618 (2020).
61. J. Dong, M. Bass, Y. Mao, P. Deng, and F. Gan, "Dependence of the Yb³⁺ emission cross section and lifetime on temperature and concentration in yttrium aluminum garnet," *J. Opt. Soc. Am. B* **20**, 1975 (2003).
62. C. Herkommer, P. Krötz, R. Jung, S. Klingebiel, C. Wandt, R. Bessing, P. Walch, T. Produit, K. Michel, D. Bauer, R. Kienberger, and T. Metzger, "Ultrafast thin-disk multipass amplifier with 720 mJ operating at kilohertz repetition rate for applications in atmospheric research," *Optics express* **28**, 30164–30173 (2020).

63. "The Laser Lightning Rod Project," www.llr-fet.eu.
64. T. Produit, P. Walch, C. Herkommer, A. Mostajabi, M. Moret, U. Andral, A. Sunjerga, M. Azadifar, Y.-B. André, B. Mahieu, W. Haas, B. Esmiller, G. Fournier, P. Krötz, T. Metzger, K. Michel, A. Mysyrowicz, M. Rubinstein, F. Rachidi, J. Kasparian, J.-P. Wolf, and A. Houard, "The laser lightning rod project," *Eur. Phys. J. Appl. Phys.* **93**, 10504 (2021).
65. www.unige.ch/gap/biophotonics/research/llr.
66. C. Romero, F. Rachidi, M. Paolone, and M. Rubinstein, "Statistical Distributions of Lightning Currents Associated With Upward Negative Flashes Based on the Data Collected at the Säntis (EMC) Tower in 2010 and 2011," *IEEE Trans. Power Delivery* **28**, 1804–1812 (2013).
67. P. Manoocherhnia, W. Schulz, F. Rachidi, and M. Rubinstein, Lightning Statistics in the regions of Saentis and St. Chrischona towers in Switzerland. 29th International Conference on Lightning Protection (2008).
68. G. P. Agrawal, *Nonlinear fiber optics*, 5th ed. (Elsevier Science, 2013).
69. R. W. Boyd, *Nonlinear optics*, 3. ed. (Elsevier/Academic Press, 2008).
70. W. Demtröder, *Experimentalphysik 2. Elektrizität und Optik*, 6., überarb. u. akt. Aufl. 2013 (Springer, 2013).
71. P. W. Milonni and J. H. Eberly, *Laser physics* (Wiley, 2010).
72. A. Yariv, *Quantum electronics*, Third edition (John Wiley & Sons, 1989).
73. M. Eichhorn, "Quasi-three-level solid-state lasers in the near and mid infrared based on trivalent rare earth ions," *Appl. Phys. B* **93**, 269–316 (2008).
74. J. He, X. Liang, J. Li, H. Yu, X. Xu, Z. Zhao, J. Xu, and Z. Xu, "LD pumped Yb:LuAG mode-locked laser with 7.63ps duration," *Opt. Express* **17**, 11537–11542 (2009).
75. J. Koerner, C. Vorholt, H. Liebetrau, M. Kahle, D. Kloepfel, R. Seifert, J. Hein, and M. C. Kaluza, "Measurement of temperature-dependent absorption and emission spectra of Yb:YAG, Yb:LuAG, and Yb:CaF₂ between 20 °C and 200 °C and predictions on their influence on laser performance," *J. Opt. Soc. Am. B* **29**, 2493–2502 (2012).
76. D. Kouznetsov, J.-F. Bisson, J. Dong, and K.-i. Ueda, "Surface loss limit of the power scaling of a thin-disk laser," *J. Opt. Soc. Am. B* **23**, 1074–1082 (2006).
77. J. Speiser, "Scaling of thin-disk lasers - influence of amplified spontaneous emission," *J. Opt. Soc. Am. B* **26**, 26–35 (2009).
78. J. Speiser, "Thin disk laser - Energy scaling," *Laser Physics* **19**, 274–280 (2009).
79. A. Antognini, K. Schuhmann, F. D. Amaro, F. Biraben, A. Dax, A. Giesen, T. Graf, T. W. Hansch, P. Indelicato, L. Julien, C.-Y. Kao, P. E. Knowles, F. Kottmann, E. Le Bigot, Y.-W. Liu, L. Ludhova, N. Moschuring, F. Mulhauser, T. Nebel, F. Nez, P. Rabinowitz, C. Schwob, D. Taqqu, and R. Pohl, "Thin-Disk Yb. YAG Oscillator-Amplifier Laser, ASE, and Effective Yb:YAG Lifetime," *IEEE J. Quantum Electron.* **45**, 993–1005 (2009).

-
80. D. Kouznetsov and J.-F. Bisson, "Role of undoped cap in the scaling of thin-disk lasers," *J. Opt. Soc. Am. B* **25**, 338–345 (2008).
81. Sellmeier, "Zur Erklärung der abnormen Farbenfolge im Spectrum einiger Substanzen," *Ann. Phys. Chem.* **219**, 272–282 (1871).
82. <https://refractiveindex.info>.
83. R. Kashyap, *Fiber Bragg gratings*. 2nd Edition, 2nd ed. (Academic, 2010).
84. O. Martinez, "3000 times grating compressor with positive group velocity dispersion. Application to fiber compensation in 1.3-1.6 μm region," *IEEE J. Quantum Electron.* **23**, 59–64 (1987).
85. E. B. Treacy, "Compression of picosecond light pulses," *Physics Letters* **1968** (1968).
86. S. Klingebiel, *Picosecond pump dispersion management and jitter stabilization in a petawatt-scale few-cycle OPCPA system*. Dissertation (2013).
87. S. Klingebiel, C. Wandt, M. Siebold, Z. Major, I. Ahmad, S. Trushin, R. Hörlein, T.-J. Wang, F. Krausz, and S. Karsch, "Counteracting gain narrowing using spectral amplitude shaping in a high-energy diode-pumped CPA system based on Yb-doped materials," in *Advanced Solid-State Photonics* (Optical Society of America, 2009), TuB9.
88. S. Klingebiel, I. Ahmad, C. Wandt, C. Skrobol, S. A. Trushin, Z. Major, F. Krausz, and S. Karsch, "Experimental and theoretical investigation of timing jitter inside a stretcher-compressor setup," *Opt. Express* **20**, 3443–3455 (2012).
89. B. Webb, M. J. Guardalben, C. Dorrer, S. Bucht, and J. Bromage, "Simulation of grating compressor misalignment tolerances and mitigation strategies for chirped-pulse-amplification systems of varying bandwidths and beam sizes," *Applied optics* **58**, 234–243 (2019).
90. I. Walmsley, L. Waxer, and C. Dorrer, "The role of dispersion in ultrafast optics," *Review of Scientific Instruments* **72**, 1–29 (2001).
91. Stefan Karsch, *Generation of ultraintense Laserpulses*. Lecture Notes. LMU München (2013).
92. H. Kogelnik and T. Li, "Laser beams and resonators," *Applied optics* **5**, 1550–1567 (1966).
93. J. Kerr, "XL. A new relation between electricity and light. Dielectric media birefringent," *The London, Edinburgh, and Dublin Philosophical Magazine and Journal of Science* **50**, 337–348 (2009).
94. J. Kasparian, M. Rodriguez, G. Méjean, J. Yu, E. Salmon, H. Wille, R. Bourayou, S. Frey, Y.-B. André, A. Mysyrowicz, R. Sauerbrey, J.-P. Wolf, and L. Wöste, "White-Light Filaments for Atmospheric Analysis," *Science* **301**, 61–64 (2003).
95. J. H. Marburger, "Self-Focusing: Theory," *Progress in Quantum Electronics* **4**, 35–110 (1975).

96. M. D. Feit and J. A. Fleck, "Effect of refraction on spot-size dependence of laser-induced breakdown," *Appl. Phys. Lett.* **24**, 169–172 (1974).
97. J. Kasparian, R. Sauerbrey, and S. L. Chin, "The critical laser intensity of self-guided light filaments in air," *Appl. Phys. B* **71**, 877–879 (2000).
98. E. Yablonovitch and N. Bloembergen, "Avalanche Ionization and the Limiting Diameter of Filaments Induced by Light Pulses in Transparent Media," *Phys. Rev. Lett.* **29**, 907–910 (1972).
99. J. Kasparian, R. Ackermann, Y.-B. Andre, G. Mechain, G. Mejean, B. Prade, P. Rohwetter, E. Salmon, K. Stelmaszczyk, J. Yu, A. Mysyrowicz, R. Sauerbrey, L. Woste, and J.-P. Wolf, "Progress towards lightning control using lasers," *J. Eur. Opt. Soc.-Rapid Publ.* **3** (2008).
100. S. L. Chin, *Femtosecond Laser Filamentation* (Springer Science+Business Media LLC, 2010).
101. G. Méchain, C. D'Amico, Y.-B. André, S. Tzortzakis, M. Franco, B. Prade, A. Mysyrowicz, A. Couairon, E. Salmon, and R. Sauerbrey, "Range of plasma filaments created in air by a multi-terawatt femtosecond laser," *Optics Communications* **247**, 171–180 (2005).
102. G. Fibich, S. Eisenmann, B. Ilan, Y. Erlich, M. Fraenkel, Z. Henis, A. Gaeta, and A. Zigler, "Self-focusing Distance of Very High Power Laser Pulses," *Optics express* **13**, 5897–5903 (2005).
103. S. Henin, Y. Petit, J. Kasparian, J.-P. Wolf, A. Jochmann, S. D. Kraft, S. Bock, U. Schramm, R. Sauerbrey, W. M. Nakaema, K. Stelmaszczyk, P. Rohwetter, L. Wöste, C.-L. Soulez, S. Mauger, L. Bergé, and S. Skupin, "Saturation of the filament density of ultrashort intense laser pulses in air," *Appl. Phys. B* **100**, 77–84 (2010).
104. TRUMPF Laser GmbH, "Data Sheet TruMicro Series 2000," https://www.trumpf.com/no_cache/de_DE/produkte/laser/kurz-und-ultrakurzpulslaser/trumicro-serie-2000/product_data_sheet/download/TRUMPF-technical-data-sheet-TruMicro-Serie-2000.pdf.
105. S. Klingebiel, M. Schultze, C. Y. Teisset, R. Bessing, M. Häfner, S. Prinz, M. Gorjan, D. Sutter, K. Michel, H. G. Barros, Z. Major, F. Krausz, and T. Metzger, "220mJ Ultrafast Thin-Disk Regenerative Amplifier," *Conference on Lasers and Electro-Optics* **STu40.2** (2015).
106. P. Kroetz, A. Ruehl, A.-L. Calendron, G. Chatterjee, H. Cankaya, K. Murari, F. X. Kärtner, I. Hartl, and R. J. D. Miller, "Study on laser characteristics of Ho: YLF regenerative amplifiers: Operation regimes, gain dynamics, and highly stable operation points," *Appl. Phys. B* **123**, 385 (2017).

107. P. Kroetz, A. Ruehl, K. Murari, H. Cankaya, F. X. Kärtner, I. Hartl, and R. J. D. Miller, "Numerical study of spectral shaping in high energy Ho:YLF amplifiers," *Optics express* **24**, 9905–9921 (2016).
108. P. Kroetz, A. Ruehl, G. Chatterjee, A.-L. Calendron, K. Murari, H. Cankaya, P. Li, F. X. Kärtner, I. Hartl, and R. J. D. Miller, "Overcoming bifurcation instability in high-repetition-rate Ho:YLF regenerative amplifiers," *Optics letters* **40**, 5427–5430 (2015).
109. S. Klingebiel, C. Wandt, M. Siebold, Z. Major, S. Trushun, R. Hörlein, T.-J. Wang, F. Krausz, and S. Karsch, "Counteracting gain narrowing using spectral amplitude shaping in a high-energy diode-pumped CPA system based on Yb-doped materials," *ASSP TuB9* (2009).
110. ISO, Lasers and laser-related equipment – Test methods for laser beam widths, divergence angles and beam propagation ratios **ISO11146** (11146) .
111. B. Eppich, J. Eichler, and L. Dünkel, "Die Strahlqualität von Lasern – Wie bestimmt man Beugungsmaßzahl und Strahldurchmesser in der Praxis?," *Laser Technik Journal* **1**, 63–66 (2004).
112. K. Beil, S. T. Fredrich-Thornton, F. Tellkamp, R. Peters, C. Kränkel, K. Petermann, and G. Huber, "Thermal and laser properties of Yb:LuAG for kW thin disk lasers," *Opt. Express* **18**, 20712–20722 (2010).
113. K. Beil, S. T. Fredrich-Thornton, F. Tellkamp, R. Peters, C. Kränkel, K. Petermann, and G. Huber, "Thermal and laser properties of Yb:LuAG for kW thin disk lasers," *Opt. Express* **18**, 20712–20722 (2010).
114. Y. F. Chen, T. M. Huang, C. F. Kao, C. L. Wang, and S. C. Wang, "Optimization in scaling fiber-coupled laser-diode end-pumped lasers to higher power. Influence of thermal effect," *IEEE J. Quantum Electron.* **33**, 1424–1429 (1997).
115. K. Albers, *Neue Konzepte für Nd:YVO4 Laser*. Dissertation (2012).
116. S. Keppler, C. Wandt, M. Hornung, R. Bödefeld, A. Kessler, A. Sävert, M. Hellwing, F. Schorcht, J. Hein, and M. C. Kaluza, "Multipass amplifiers of POLARIS," *Proc. SPIE 8780, High-Power, High-Energy, and High-Intensity Laser Technology; and Research Using Extreme Light: Entering New Frontiers with Petawatt-Class Lasers*, 87800I (7 May 2013).
117. J. Körner, J. Hein, and M. Kaluza, "Compact Aberration-Free Relay-Imaging Multi-Pass Layouts for High-Energy Laser Amplifiers," *Applied Sciences* **6**, 353 (2016).
118. M. Zeyen, I. Schulthess, K. S. Kirch, M. Marszalek, L. Sinkunaite, A. Antognini, J. Nuber, F. Nez, R. Pohl, and A. Knecht, "Compact 20-pass thin-disk amplifier insensitive to thermal lensing," *Proc. SPIE 10896, Solid State Lasers XXVIII: Technology and Devices*, 108960X (7 March 2019).

119. K. Schuhmann, K. Kirch, and A. Antognini, "Multi-pass resonator design for energy scaling of mode-locked thin-disk lasers," Proc. SPIE 10082, Solid State Lasers XXVI: Technology and Devices, 100820J (17 February 2017).
120. J.-P. Negel, A. Loescher, B. Dannecker, P. Oldorf, S. Reichel, R. Peters, M. Abdou Ahmed, and T. Graf, "Thin-disk multipass amplifier for fs pulses delivering 400 W of average and 2.0 GW of peak power for linear polarization as well as 235 W and 1.2 GW for radial polarization," Appl. Phys. B **123**, 1237 (2017).
121. J.-P. Negel, A. Loescher, A. Voss, D. Bauer, D. Sutter, A. Killi, M. A. Ahmed, and T. Graf, "Ultrafast thin-disk multipass laser amplifier delivering 1.4 kW (4.7 mJ, 1030 nm) average power converted to 820 W at 515 nm and 234 W at 343 nm," Optics express **23**, 21064–21077 (2015).
122. J. Tümmler, R. Jung, H. Stiel, P. V. Nickles, and W. Sandner, "High-repetition-rate chirped-pulse-amplification thin-disk laser system with joule-level pulse energy," Opt. Lett. **34**, 1378–1380 (2009).
123. M. Schulz, R. Riedel, A. Willner, S. Düsterer, M. J. Prandolini, J. Feldhaus, B. Faatz, J. Rossbach, M. Drescher, and F. Tavella, "Pulsed operation of a high average power Yb:YAG thin-disk multipass amplifier," Optics express **20**, 5038–5043 (2012).
124. T. Gottwald, V. Kuhn, S.-S. Schad, C. Stolzenburg, and A. Killi, "Recent developments in high power thin disk lasers at TRUMPF Laser," 88980P.
125. D. Bauer, TRUMPF Laser GmbH, Unterföhring (personal communication, 2018).
126. R. Paschotta, "Beam quality deterioration of lasers caused by intracavity beam distortions," Opt. Express **14**, 6069–6074 (2006).
127. W. Koechner, "Solid-State Lasers. A Graduate Text," **2003**.
128. C. Herkommer, P. Krötz, S. Klingebiel, C. Wandt, D. Bauer, K. Michel, R. Kienberger, and T. Metzger, "Towards a Joule-Class Ultrafast Thin-Disk Based Amplifier at Kilohertz Repetition Rate," in Conference on Lasers and Electro-Optics (Optical Society of America, 2019), SM4E.3.
129. Plymouth Grating Laboratory Inc. (personal communication).
130. M. Mero, J. Liu, W. Rudolph, D. Ristau, and K. Starke, "Scaling laws of femtosecond laser pulse induced breakdown in oxide films," Phys. Rev. B **71**, S373 (2005).
131. T. Metzger, A. Schwarz, C. Y. Teisset, D. Sutter, A. Killi, R. Kienberger, and F. Krausz, "High-repetition-rate picosecond pump laser based on a Yb:YAG disk amplifier for optical parametric amplification," Opt. Lett. **34**, 2123–2125 (2009).
132. J. Novák, J. T. Green, T. Metzger, T. Mazanec, B. Himmel, M. Horáček, Z. Hubka, R. Boge, R. Antipenkov, F. Batysta, J. A. Naylor, P. Bakule, and B. Rus, "Thin disk amplifier-based 40 mJ, 1 kHz, picosecond laser at 515 nm," Opt. Express **24**, 5728–5733 (2016).

133. H. Fattahi, H. G. Barros, M. Gorjan, T. Nubbemeyer, B. Alsaif, C. Y. Teisset, M. Schultze, S. Prinz, M. Haefner, M. Ueffing, A. Alismail, L. Vámos, A. Schwarz, O. Pronin, J. Brons, X. T. Geng, G. Arisholm, M. Ciappina, V. S. Yakovlev, D.-E. Kim, A. M. Azzeer, N. Karpowicz, D. Sutter, Z. Major, T. Metzger, and F. Krausz, "Third-generation femtosecond technology," *Optica* **1**, 45–63 (ts).
134. T. Produit, P. Walch, G. Schimmel, B. Mahieu, C. Herkommer, R. Jung, T. Metzger, K. Michel, Y.-B. André, A. Mysyrowicz, A. Houard, J. Kasparian, and J.-P. Wolf, "HV discharges triggered by dual- and triple-frequency laser filaments," *Optics express* **27**, 11339–11347 (2019).
135. A. Talebpour, S. Petit, and S. L. Chin, "Re-focusing during the propagation of a focused femtosecond Ti:Sapphire laser pulse in air," *Optics Communications* **171**, 285–290 (1999).
136. P. J. Wrzesinski, D. Pestov, V. V. Lozovoy, J. R. Gord, M. Dantus, and S. Roy, "Group-velocity-dispersion measurements of atmospheric and combustion-related gases using an ultrabroadband-laser source," *Opt. Express* **19**, 5163–5170 (2011).
137. P. Walch, B. Mahieu, M. Lozano, Y.-B. Andre, L. Bizet, U. Andral, V. Moreno, T. Produit, C. Herkommer, R. Bessing, T. Metzger, J. Kasparian, J.-P. Wolf, A. Mysyrowicz, and A. Houard, "Long distance laser filamentation using Yb:YAG kHz laser," *European Optical Society Annual Meeting* (2021).
138. Y. Pfaff, M. Rampp, C. Herkommer, R. Jung, C. Y. Teisset, S. Klingebiel, and T. Metzger, "Ultrafast thin-disk amplifier with over 500 mJ pulse energy at 1 kHz repetition rate," *European Optical Society Annual Meeting* (2021).
139. L. Rui, Z. Xihe, F. Gong, J. Yong, S. Deng, Y. Jin, and G. Li, "Effect for an anti-ASE cap thickness on pump spot uniformity in a thin disk laser," in *Advanced Laser Technology and Applications* (SPIE, 2018), pp. 172–176.
140. Y. Qiao, X. Zhu, G. Zhu, Y. Chen, W. Zhao, and H. Wang, "Analytical model of amplified spontaneous emission with different thickness anti-ASE caps for thin disk lasers," *Applied optics* **56**, 5131–5138 (2017).
141. D. A. Copeland, "Amplified spontaneous emission (ASE) models and approximations for thin-disk laser modeling," in *Solid State Lasers XXII: Technology and Devices* (SPIE, 2013), pp. 342–365.
142. P. Peterson, A. Gavrielides, T. C. Newell, N. Vretenar, and W. P. Latham, "ASE in thin disk lasers. Theory and experiment," *Optics express* **19**, 25672–25684 (2011).
143. M. Wang, G. Zhu, X. Zhu, Y. Chen, J. Dong, H. Wang, and Y. Qian, "Thickness optimization for an anti-ASE cap in a thin disk laser considering dioptric power and aberration-induced loss," *J. Opt. Soc. Am. B* **35**, 583 (2018).

144. M. Dillmann, Simulation of Amplified Spontaneous Emission in High Power Thin Disk Lasers. Master Thesis, Friedrich-Alexander Universität Erlangen-Nürnberg (2019).
145. J. Schulte, T. Sartorius, J. Weitenberg, A. Vernaleken, and P. Russbuedt, "Nonlinear pulse compression in a multi-pass cell," *Optics letters* **41**, 4511–4514 (2016).
146. P. Balla, A. Bin Wahid, I. Sytceвич, C. Guo, A.-L. Viotti, L. Silletti, A. Cartella, S. Alisauskas, H. Tavakol, U. Grosse-Wortmann, A. Schönberg, M. Seidel, A. Trabattoni, B. Manschwetus, T. Lang, F. Calegari, A. Couairon, A. L'Huillier, C. L. Arnold, I. Hartl, and C. M. Heyl, "Postcompression of picosecond pulses into the few-cycle regime," *Optics letters* **45**, 2572–2575 (2020).
147. M. Kaumanns, V. Pervak, D. Kormin, V. Leshchenko, A. Kessel, M. Ueffing, Y. Chen, and T. Nubbemeyer, "Multipass spectral broadening of 18 mJ pulses compressible from 1.3 ps to 41 fs," *Optics letters* **43**, 5877–5880 (2018).
148. F. Salehi, A. J. Goers, G. A. Hine, L. Feder, D. Kuk, B. Miao, D. Woodbury, K. Y. Kim, and H. M. Milchberg, "MeV electron acceleration at 1 kHz with <10 mJ laser pulses," *Optics letters* **42**, 215–218 (2017).
149. K. Fritsch, M. Poetzlberger, V. Pervak, J. Brons, and O. Pronin, "All-solid-state multipass spectral broadening to sub-20 fs," *Optics letters* **43**, 4643–4646 (2018).

10 Appendix

A.1 Characterization of the MP Pump Power

Table 10.1: Pump energy as a function of pump pulse duration and the peak pump power.

Pump Energy (J)		Pump Duration (μs)									
Peak Power (kW)	125	150	200	250	300	350	400	450	500	600	700
2,4	0,13	0,18	0,28	0,38	0,47	0,58	0,69	0,74	0,83	1,24	1,50
3,6	0,25	0,33	0,49	0,65	0,80	0,97	1,13	1,25	1,4	1,85	2,20
4,8	0,37	0,48	0,70	0,92	1,13	1,36	1,58	1,76	1,97	2,46	2,91
6	0,51	0,65	0,92	1,19	1,46	1,73	2,00	2,27	2,54	3,08	3,62
7,2	0,63	0,8	1,13	1,46	1,79	2,12	2,45	2,78	3,11	3,77	4,43
8,4	0,75	0,95	1,34	1,73	2,12	2,51	2,9	3,29	3,68	4,46	5,24
9,6	0,875	1,1	1,55	2	2,45	2,9	3,35	3,8	4,25	5,15	6,05
10,8	0,99	1,24	1,75	2,26	2,77	3,28	3,79	4,30	4,81	5,83	6,85
12	1,19	1,46	2	2,53	3,1	3,6	4,12	4,63	5,13	6,14	7,15

A.2 Data Sheet TRUMPF TruMicro2000

	TruMicro 2020	TruMicro 2030
LASERPARAMETER		
MITTLERE AUSGANGSLEISTUNG	10 W	20 W
STRAHLQUALITÄT (M ²)	< 1.3	< 1.3 optional < 1,2
WELLENLÄNGE	1030 nm	1030 nm
PULSDAUER	20 ps < 900 fs < 400 fs	20 ps optional 900 fs 400 fs oder variabel einstellbar von < 400 fs - 20 ps
MAX. PULSENERGIE	10 µJ optional 20 µJ und 50 µJ	20 µJ optional 50 µJ oder 100 µJ
MAX. REPETITIONSRATE	1000 kHz optional 2000 kHz, 200 kHz bei 50 µJ Pulsenergie (10 W)	1000 kHz optional 2000 kHz, 400 kHz bei 50 µJ Pulsenergie (20 W) oder einstellbar von 200 kHz (100 µJ Pulsenergie) bis 2 MHz (10 µJ Pulsenergie)
BAUFORM		
ABMESSUNGEN LASERKOPF (B X H X T)	570 mm x 360 mm x 180 mm	570 mm x 360 mm x 180 mm
ABMESSUNGEN VERSORGUNGSGERÄT (B X H X T)	510 mm x 485 mm x 180 mm	510 mm x 485 mm x 180 mm

Danksagung

Die Entstehung dieser Arbeit wurde durch die Unterstützung und Beiträge von vielen Menschen ermöglicht, bei denen ich mich an dieser Stelle herzlich bedanken möchte.

Mein Dank gilt zunächst meinen beiden Betreuern Prof. Reinhard Kienberger und Tom Metzger, die mich auf dem Weg meiner Promotion begleitet haben. Ich bin euch sehr dankbar, dass ihr verlässlich an meiner Seite standet und damit den Rahmen für die Durchführung meiner Promotion geschaffen und ermöglicht habt. Den durchweg unkomplizierten und direkten Umgang mit euch habe ich sehr geschätzt.

Ebenso möchte ich meinen sehr geschätzten TLM Kollegen danken, auf deren unglaublichen Erfahrungsschatz bei der Laserentwicklung ich stets zurückgreifen konnte. Insbesondere Peter Krötz möchte ich Danke sagen, dass du mir vor allem am Anfang unter die Arme gegriffen hast und immer für Diskussionen von Messungen und Fachsimpelien offen warst. Auch dir, Robert Bessing, gilt ein besonderer Dank, dafür, dass du beim Endspurt mit mir Vollgas gegeben hast und ich bei den Installationen voll auf dich zählen konnte. Ohne dich hätte ich's nicht geschafft!

Danke auch an alle LLR-Projektpartner, die zum Gelingen des Projektes sehr große Beiträge geleistet und eine erfolgreiche Kollaboration ermöglicht haben. Danke für eure Offenheit, Expertise und Motivation das Projekt trotz der Pandemie zum Erfolg zu führen.

Auch den Schramberger Kollegen gilt mein Dank, für tausende Tipps, Tricks und Kniffe, die Remote-Unterstützung und den Austausch über aktuelle Entwicklungen. Insbesondere bei Dominik Bauer und Tobias Hangst möchte ich mich an dieser Stelle nochmal herzlich bedanken.

Meinen Eltern und Geschwistern möchte ich danke sagen, dass sie mich auf meinem Lebensweg stets begleitet haben und mich auf verschiedenen Wegen immer gefördert haben. Danke für eure Hilfe und Großzügigkeit.

Den größten Dank möchte ich zuletzt meiner Frau Anna aussprechen. Du hast mich bei so vielen Emotionen begleitet, mir Mut gemacht, mich motiviert, mich glücklich gemacht. Ich bin dir unendlich dankbar für deine Liebe, deine Geduld, dein Verständnis und deine Unterstützung in Zeiten wo viele Opfer nötig waren. Ohne dich hätte ich es nicht geschafft. Danke, dass Du und Jonah bei mir seid!